CHARACTERIZATION OF ION PROPERTIES IN A LINEAR PULSED PLASMA-MATERIAL INTERACTION TEST STAND

BY

MICHAEL PETER CHRISTENSON

THESIS

Submitted in partial fulfillment of the requirements
for the degree of Master of Science in Nuclear, Plasma, and Radiological Engineering
in the Graduate College of the
University of Illinois at Urbana-Champaign, 2015

Urbana, Illinois

Master's Committee:

Professor David N. Ruzic, Adviser
Assistant Professor Davide Curreli

ABSTRACT

In the edge and divertor regions of the magnetically confined plasma, tokamaks experience off-normal events in which high intensities of heat flux incident on wall component surfaces result in intolerable levels of damage. Proposed solid divertors will not be able to withstand these fluxes, especially in larger toroidal machines such as ITER and DEMO. In addition to this detrimental effect on solid wall materials, demonstrations have shown that the erosion of these materials can cause impurity generation and transport within the bulk plasma, leading to high radiative losses. To avoid these and other major issues, liquid metal divertor and wall schemes have been proposed and studies have been done to understand their effect on bulk tokamak plasmas.

To simulate extreme events in the tokamak boundary and provide a test stand for liquid-metal plasma-facing components, a pulsed plasma source utilizing a theta pinch in conjunction with a coaxial plasma accelerator has been developed[1-3]. The ThermoElectric-driven Liquid-metal plasma-facing Structures (TELS) device will provide fusion-relevant plasma flux incident on structures with flowing liquid metal surfaces. In order to accurately quantify the ability of TELS to provide a simulated disruption or edge localized mode (ELM) plasma, a suite of diagnostics was used to measure a variety of plasma parameters. The objective of this thesis was to develop an electrostatic analyzer to measure the ion information in TELS and use the results to understand particle energy distribution and loss as a function of distance from the plasma source.

It has been previously observed that TELS plasmas can bombard a target with an electron density of 3×10^{21} m^{-3}, an electron temperature of 20 to 30 eV, and a peak energy flux of 0.08 MJ/m^2 over the pulse length of 100 to 200 μs[2]. To validate that the experimentally observed heat flux delivered to a target corresponds to the isotropic magnetohydrodynamic (MHD) predictions based on electron and ion temperatures, it became necessary to evaluate the ion temperature and subsequent energy distribution. In addition to these theoretical comparisons, the ion temperature and transport of ions down the length of the chamber is important in order to fully characterize a system that preferentially heats and accelerates ions as a function of the energy coupling in the theta pinch.

Two major conditions were imposed to observe how ions behave as a function of the effect of the compression with the theta pinch. First, the analyzer system comprised of an analyzer open to the plasma and an analyzer closed to the plasma was inserted into the target chamber, at a distance of 16 inches (40.6 cm) downstream of the theta pinch. The closed analyzer was used as an experimental control, so that the effects of electromagnetic and circuit noise were eliminated from the open analyzer signal. The ion current showed two prominent features that followed in suit with the way the PiP discharges, and the time-averaged temperatures were taken with respect to the duration of these features during the pulse. Without guiding magnetic fields used to prevent ion diffusive losses, the measured ion signal showed an ion temperature of 22.83 ± 7.43 eV for the first peak and 17.59 ± 11.53 eV for the second peak. This measurement was used as a basis against which to compare ion temperatures subject to different pulse conditions. Secondly, the analyzer system measured the ion information from the use of only the coaxial plasma accelerator as a comparison by which the theta pinch can be proven effective or not. Without the use of guiding fields, the measured signal showed an ion temperature of 10.40 ± 6.62 eV for the first peak and 7.70 ± 3.57 eV for the second peak. The effects of these results from a plasma transport and a plasma-material interaction basis will be discussed.

To my wife and family

ACKNOWLEDGEMENTS

The completion of this thesis would have not been possible were it not for the support of a great number of people. I will attempt to acknowledge all individuals who contributed to this work, but the list is by no means comprehensive.

I would most importantly like to acknowledge and appreciate my wife, Lindsay F. Christenson, the love of my life, who has supported me through all of the ups and downs of my undergraduate and graduate career. She is the foundation on which I can face the world, and the person who can brighten even the gloomiest of my days. I love her forever.

My parents, Peter G. and Cynthia A. Christenson, are the reason why I have progressed so far in my educational development. Throughout my life, they continuously challenged me to be all that I could be, while still maintaining the sincere attitude that I was just as intelligent and as determined as any other person. Without their guidance, I would have never made it this far.

I am also greatly indebted to my advisor, Professor David N. Ruzic, who has given me this wonderful opportunity. He is an amazing teacher and a wonderful advisor. It is from him that I have learned how to become an independent thinker and researcher.

I would also like to thank every individual at the Center for Plasma-Material Interactions who has helped me out at one time or another. I would especially like to thank Casey Bryniarski, Zehuan Song, Mikhail Finko, Brandon Lee, Steven Stemmley, Jeremy Mettler, Xia Sang, and Dan Martin who have helped me so much over the last couple of years with advice and experimentation. I would like to thank Professor Davide Curreli, who has been an inspiration to me during my computational studies of plasmas, as well as by far and away one of the most brilliant people I have ever met. I would also very much like to thank the postdoctoral assistants who have been in the lab, namely Dr. Kishor Kalathiparambil. I would finally like to thank the most influential member in my graduate career, previously of the Center for Plasma-Material Interactions, Soonwook Jung. I have learned so much from you and will never be able to repay my debt.

TABLE OF CONTENTS

CHAPTER 1: INTRODUCTION

1.1 Fusion Energy

As the world approaches a position in which non-renewable resources become less viable as an energy source, it will become necessary to explore alternative avenues for energy generation to rid the world of its fossil fuels dependence. Current efforts have been focusing on sources including solar, wind, biological, fission, and fusion energy systems. Among these energy source types, fusion has been considered as one of the most attractive alternative sources due to its abundance of fuel, lack of byproducts, and potential for high efficiency. With the current world inventory of deuterium, a critical reactant in the fusion reaction, it is expected that fusion could meet the world's energy needs for millions of years as long as tritium breeding becomes a commercially attainable process[4].

While fusion remains the most attractive alternative resource, researchers have yet to achieve a stable fusion reaction that can generate more energy than it consumes. Reasons behind this shortcoming are numerous, but focus primarily on issues of plasma confinement, plasma transport, plasma heating, and plasma-wall interactions. In order for any type of fusion reactor to accomplish a net energy output, the Lawson criterion must be satisfied. The achievement of this condition allows the reactor to reach a condition known as "ignition", in which the reactor can sustain a fusion chain reaction, with the α particles carrying enough energy to continue the reaction. The approximate value of the triple product used to evaluate the Lawson criterion for a deuterium-tritium reaction is[5]

$$n_e T \tau_E \geq 10^{21} keV\ s/m^3 \tag{1.1}$$

where n_e is the electron density, T is the average temperature of the plasma, and τ_E is the confinement time of the plasma. Different methods for fusion take advantage of different parameters in the above equation, with the two major fusion concepts being inertial confinement and magnetic confinement. Inertial confinement at the National Ignition Facility aims to achieve ignition at a plasma pressure of 10^{11} atm in 1 x 10^{-9} s[6]. Alternatively, magnetic confinement at the International Thermonuclear Experimental Reactor (ITER) aims to accomplish the ignition

condition at a plasma pressure of 7 atm, confined for a duration of nearly 1 s with a proposed operation time of 3600 s[7,8]. The topic of this thesis relates to magnetic confinement and proposed methods to reach ignition and reduce detrimental effects of the plasma-material interactions.

Prior to the early 1980s, magnetically confined toroidal fusion devices operated in the L-type regime, which resulted in plasmas that lacked the required temperature and density to achieve even the condition of breakeven, where the power gained from the fusion reaction is equivalent to the input power. At the time, it was thought that increasing auxiliary heating to the plasma would result in hotter plasmas that could be confined for the same if not longer durations when compared to experiments without extra auxiliary heating. These attempts resulted in discouraging observations, namely that even with increased auxiliary heating the confinement time of the plasma suffered[9].

Then, in 1982, a very important breakthrough occurred. The ASDEX device, located in Germany, was able to achieve a new type of discharge using divertor and limiter schemes in the edge of the plasma[10]. This new H-type mode resulted in plasmas with higher densities and temperatures, typically by a factor of 2, and longer confinement times, and was a result of larger density and temperature gradients being developed at the plasma boundary generating a feature known as the pedestal. It was later proved on ASDEX and other machines that because of the inhibition of particle transport across the pedestal, the confinement is thereby strongly influenced by the height and gradient of the density and temperature pedestal[11-14]. While the discovery of the H mode operation in toroidal fusion devices helped to radically alter the landscape of fusion research, it too suffered from new forms of instabilities and confinement loss, which have been active areas of research since the ASDEX discovery.

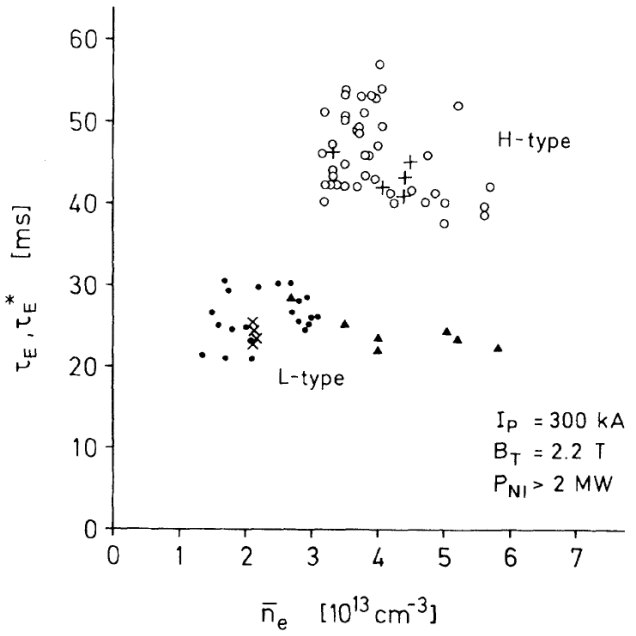

Figure 1.1: Global energy confinement time vs. average line density for toroidal limiter (triangles) and divertor discharges (other symbols) as seen in Ref. [10].

1.2 Roadblocks to Fusion Energy: Edge Localized Modes and Disruptions

The advent of the H mode type discharge in magnetic fusion devices has advanced the field far beyond what was achievable prior to the discovery on ASDEX, but the new confinement did not come without its own issues. Edge localized modes (ELMs) and disruptions became the new problems as more machines were able to achieve H mode operation. Both of these events were a product of the excitation and growth of new modes and either pressure-driven or current-driven instabilities, and both are characterized by plasma ejection. Also, both off-normal events occur over very short timescales, typically less than a few milliseconds, which prevent radiative and convective cooling of wall materials as a power mitigation strategy.

The most important question surrounding the new type of off-normal events is how wall materials will handle the power loading from the plasma ejections, and what can be done to mitigate a large portion of this heat flux. In a number of machines it was observed that in high heating regimes and high ELM frequency, 20 – 40% of the total stored energy in the plasma crosses the separatrix, resulting in a significant amount of energy delivered to the divertor surface[15-19]. A good example of this is found in Ref. [20], where a stored ITER plasma energy

of 1200 MJ results in an ELM energy on target of 25 to 80 MJ at a frequency of 1 to 5 Hz. This high level of repeated power flux will permanently damage the proposed wall materials, with reports indicating that such materials would only survive if ITER level ELMs could either be completely eradicated or reduced by 95%[21]. For this reason, apart from preventing losses due to introductions of high Z materials from the walls, efforts have been made to reduce ELM intensities and produce alternative, more suitable, wall materials. While disruption mitigation effects are also being explored, this work will focus primarily on the ELM-material interactions and physics.

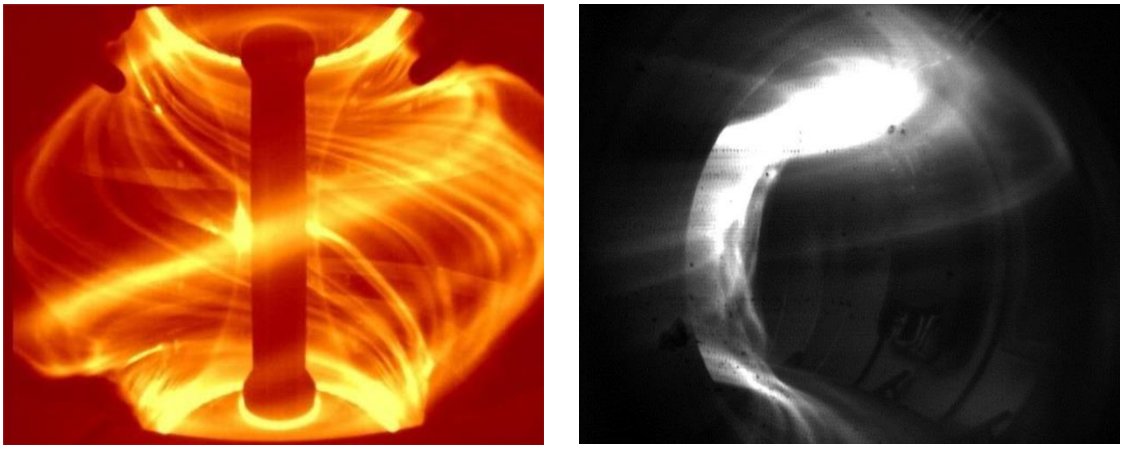

Figure 1.2: (a) A high-speed video image of the MAST plasma obtained at the start of an ELM[22]. (b) A high-speed video image of the Tore Supra plasma obtained during a disruption event[23].

1.3 Liquid Lithium as a Wall Material

To address the concerns over solid wall materials and their capabilities to handle off-normal events in large devices, especially ITER, many alternate schemes have been proposed. Among these, the most promising deal with using lithium on wall components, both in the solid and liquid form[24]. Lithium is desirable as a wall material for a number of reasons. Most importantly, it leads to much lower radiative losses when introduced into the plasma as compared with tungsten or molybdenum, which are materials considered strongly for solid tiles in larger machines. Additional benefits of lithium include the fact it getters high-Z impurities such as carbon and oxygen and has a very low wall recycling coefficient[25,26].

Lithium does not come without its own drawbacks, however. Because of its ability to getter high-Z materials quickly and to react strongly with oxygen, nitrogen, and hydrogen, the surface of the lithium can become passivated on a relatively short timescale[27,28]. This passivation layer on the surface of the lithium coating becomes a hindrance to the benefits that a fresh lithium coating provides. It is for this reason that a flowing liquid lithium surface is desired to replenish the passivated coating with a fresh surface. Work at the University of Illinois at Urbana-Champaign has aimed at achieving a stable flowing liquid lithium surface utilizing thermoelectric-driven magnetohydrodynamic (TEMHD) flow as the primary driving force[29,30]. This Lithium-Metal Infused Trenches (LiMIT) configuration is beneficial due to its ability to passively pump lithium and its resistance to surface instabilities that cause rapid lithium ejection into the plasma.

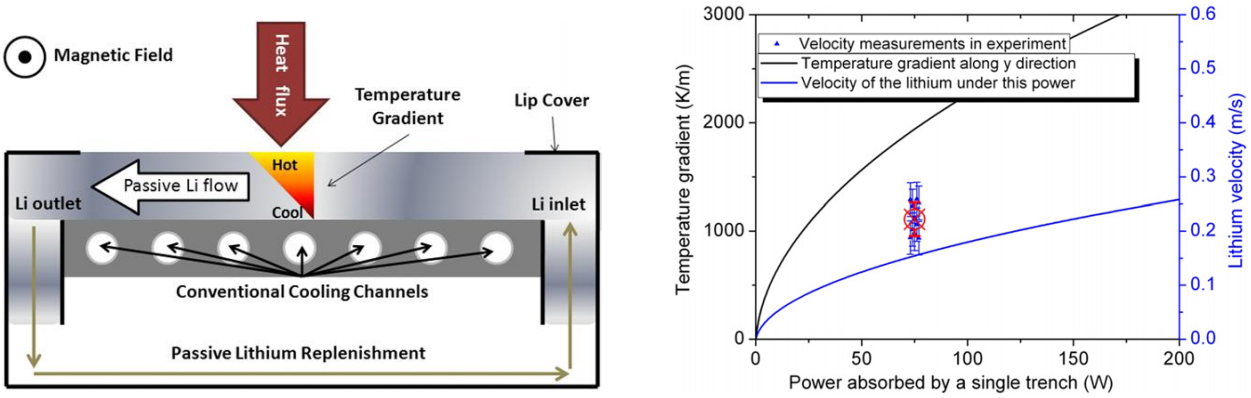

Figure 1.3: (a) Concept of removing heat using TEMHD flow. The Li regenerates due to rotational flow around the cooling channels, (b) Theoretical temperature gradient and lithium velocity profiles as a function of absorbed power. The particle tracking method data are also shown[29].

To understand the ability of the LiMIT device to be able to handle fusion-level, off-normal events at the timescales of ELM-like discharges, work has begun at the University of Illinois at Urbana-Champaign to develop a pulse simulator to deliver relevant heat fluxes to a target[1,2]. To fully understand the impact the pulsed plasma has on the LiMIT device, the plasma had to be characterized using a number of different diagnostic techniques. Previous work was accomplished to generate an understanding of the isotropic heat loads delivered onto a target under specific pulsed conditions, but the data lacked the necessary ion information to draw a significant conclusion when compared to theoretical predictions. This work, therefore, focuses

primarily on the gathering of the ion information to better understand the plasma-material interactions in the ThermoElectric-driven Liquid metal plasma facing Structures (TELS) device.

1.4 Review of Previous Experimental Work

Understanding the relevance ions play in plasma devices has been an active area of research for decades, especially in the magnetic fusion community. This is due in large part to the fact that ions subjected to fusion conditions often have distributions with mean energies, or ion temperatures, comparable to those of electrons. Hutchinson[31] succinctly summarized the various diagnostic types used to acquire ion information for a wide array of plasmas, with ion energies ranging from thermal temperatures all the way to fusion temperatures. This work will focus on those diagnostics relevant to magnetic fusion.

One of the more common earlier techniques used for the measurement of ion temperatures dealt with charge exchange recombination spectroscopy (CXRS)[32-38], where ion energy distributions were derived based on the detected counts of hot atoms that had undergone charge-exchange collisions with ions and the known energy of neutrals injected into the plasma control volume. While these techniques seemed to give the first semblance of an ion energy distribution, even within magnetic fusion conditions, they were subject to numerous sources of error. First, the neutral flux inside of the tokamak plasma had to be known to accurately determine how the incoming cold neutral flux would react with the ions. Second, this technique operated on the ideal assumption that only two potential collisions could occur: charge-exchange or ionization. Third, critical densities could easily prevent travel across the chord of interest to the detector. Finally, the distributions measured in these experiments were often line-averaged or global in nature, since local effects at any given point along the chord were often integrated out of the final analysis. This last point is very important, since ion temperatures and energy distributions in the edge and scrape-off layers of a tokamak are essential in determining the energy and power flux to a wall or divertor material.

This inability to make local measurements of the ion temperature and energy distribution gave rise to the use of a probe diagnostic, known as a retarding field energy analyzer (RFEA) or, simply, a gridded energy analyzer (GEA). The retarding field supplied by the ion discriminating

grids in these diagnostics allowed the controller to sweep out ions of energies less than the desired value. A diagram of a simplified setup for an ion energy analyzer can be seen in Fig. 1.4. The resulting current waveform measured over the voltage sweep of this grid allowed for the extraction of a distribution, which in turn could be used to find the ion temperature. The RFEA diagnostic has been used as a local indicator of ion energies in toroidal fusion devices since the 1970s and 1980s[39-43], and remains a popular choice to extract ion information to this day[44-49]. A summarizing table of the ion temperatures found in different regions of a number of toroidal devices using an RFEA can be found in Table 1.1.

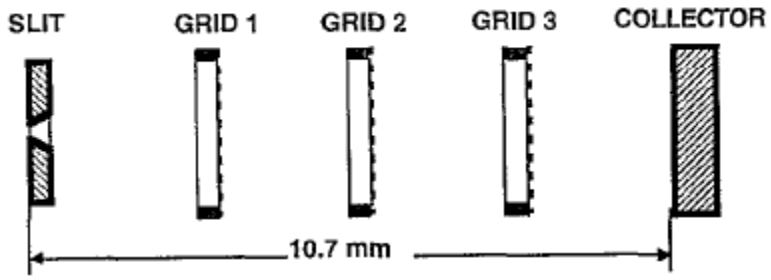

Fig. 1.4: A cartoon depiction of a retarding field energy analyzer operating in ion analysis mode[47].

Table 1.1: A summary of the mean ion energies found in various toroidal devices using RFEAs.

	Alcator C-Mod[44]	ISTTOK[45]	JET[49]	MAST[46]	
Plasma Type	SOL	Boundary	Midplane Separatrix	SOL	ELMy
T_i, eV	90.9	~ 15	~ 50	20 – 40	200 - 500

As Hutchinson[31] accurately states, even though RFEAs can measure local quantities, they are not without their own set of drawbacks. Primary among these are the geometrical limitations on this diagnostic brought about by the extreme conditions of the fusion plasma in which the probe configuration is inserted. For instance, in order to adequately compensate for issues involving plasma penetration, the opening aperture, or series of apertures in a low-transparency mesh, must be less than the sheath size. Fusion devices and the TELS device in particular have Debye lengths that are incredibly small, on the order of micrometers to tens of

micrometers, making the sheath size of four to six times the Debye length a limiting dimension. This limitation prevents plasma penetration into the main body of the analyzer, which could ignite a secondary, lower-energy plasma and generate a second peak in the distribution corresponding to this new plasma. Another geometrical limitation linked to the Debye length and sheath size pertains to the axial spacing between the grids, assuming cylindrical geometry for the analyzer body. Hutchinson[31] states that the axial spacing between the grids is limited again by the sheath size, which is too small in fusion devices to make a practical analyzer system. This limitation, however, helps to prevent two debilitating phenomena that can occur in a gridded analyzer: (1) the potential breakdown between grids at different polarities, and (2) the problematic contribution of space charge effects. Using a low transparency mesh or a very small aperture or slit at the beginning of the analyzer body, as is done in most cases, can eliminate this geometrical problem by greatly reducing the density on the downstream side of the aperture, slit, or mesh. In this case, it becomes important to take into account the mean free paths of different collision types for the injected gas to adequately determine the new spacing between the grids, which can help to alleviate the practical constraint of a highly collisional, dense plasma. While it seems that a low transparency on the first aperture, slit, or mesh can essentially eliminate all the problems facing an analyzer diagnostic, it also greatly reduces the signal to noise ratio, making the analyses of most current-voltage traces incredibly difficult. The signal to noise ratio, however, can be greatly improved by properly insulating the probe body and significantly isolating the collection signal from other lines connected to the chamber.

1.5 Thesis Objective

Current plasma properties of the TELS experiments are fairly well known, but key information about the ions is entirely lacking from the previous analysis. This information is imperative since the theta pinch can preferentially heat the ions of an already fast-moving plasma in order to generate higher temperature ions[2,31]. This is due mainly to the difference in the mass and momentum carried by the ions relative to the electrons, so most of the energy delivered by the theta pinch couples to the ions as opposed to the electrons.

To accomplish the goal of obtaining the ion information in a pulsed system such as TELS, this work investigates the theory, design criteria, and operation of an electrostatic energy analyzer, which allows a range of energies in various pulsed conditions to be measured. While other diagnostics, such as charge exchange recombination spectroscopy, are often used to obtain ion information, the predicted temperatures and timescale of the pulse approach the limits of most conventional diagnostic types. Apart from the limits placed on other diagnostics, electrostatic analyzers have been successful even under extreme conditions, such as in the edge and scrape-off layer areas of fusion plasmas[44-49]. The data gathered by the analyzer will serve as a parameter basis for liquid lithium experiments and will complete the bridge between theoretical predictions and experimentally observed data. The finalized results will also serve as the first set of ion information gathered by an electrostatic analyzer system in both the highly transient TELS device and other similar transient linear pulsed devices.

1.6 Thesis Overview

Over the course of this thesis, the work performed in order to uncover the ion information of TELS plasmas using an electrostatic analyzer will be presented. Chapter 2 will discuss a coupled numerical simulation still in development used as a basis for the physical results. Chapter 3 will introduce the theory and operation of the TELS device, as well as the electrostatic analyzer. This chapter will also help elucidate the proper criteria for developing an analyzer type diagnostic for use in highly-magnetized, highly-transient pulsed plasmas. Proper adherence to these criteria will allow for mitigation of noise generated by electromagnetic perturbations in the signal collection lines, along with noise produced by inadequate grounding issues. Chapter 4 will discuss the work performed in gathering the ion data from the electrostatic analyzer. Chapter 5 will discuss the broader implications of this information relative to the future work with the TELS device and fusion in general, and will conclude the work with a summary of the previous chapters.

CHAPTER 2: DEVELOPMENT OF ENERGY ANALYZER SIMULATION

2.1 Simulation Overview

Because of the Maxwellian regime under which TELS can be classified due to its high ionization fraction and very high collisionality, the plasma has previously been simulated using the open source Athena MHD code[2]. The Athena MHD code[50] was chosen as the primary solution method, which uses a higher order Gudonov scheme in order to solve the system of fluid equations and allow for an adaptive mesh refinement. This scheme can allow for the final result to be more exact in regards to other fluid solution methods, such as operator splitting methods and upwind methods, without sacrificing too much in the way of computational complexity. On top of this inherent advantage in relation to other fluid solvers, the Gudonov method has also shown to be significantly more accurate when the system has discontinuities, such as shocks, present due to the fact that these appear as characteristics in the solution to the Reimann problem [51].

The work done in Ref. [2] was replicated and the solutions were used as inputs into the primary focus of this report, the PIC simulation of the sheath physics at the entrance to an ion energy analyzer. This included the utilization of the same primary geometry and boundary conditions for the Athena simulation. The simulation was defined by a cylindrical geometry, with 50 cells in the radial direction, 100 cells in the axial direction, and 2 cells in the angular direction. The plasma was initialized as a dense slug in the region corresponding to the overall length of the theta pinch (~ 40 cells). The boundaries were set to: (1) flow out conditions at the axial boundaries, (2) a periodic condition at the angular boundaries, (3) a momentum and magnetic field reflecting condition at r = 0, and (4) a momentum reflecting condition at r = R[2]. These details will be illustrated in Section 2.

The coupling of MHD fluid-like solvers and local PIC kinetic solvers has been an ever-growing topic in computational plasma physics due in large part to the need to encompass the entirety of the physics happening in a plasma system. MHD fluid solvers can offer great insight

into how the plasma fluid body behaves, but these solvers cannot grasp the local effects from the kinetic description. PIC solvers can fully encompass the physical model of the plasma, not needing to rely on assumptions to simplify the model, but in doing so become computationally expensive. Efforts, like those at the University of Michigan[52], have been taken to couple these codes by using the information from each at the previous time step to update both solution types at a new time step. While this helps to capture the whole of the physical model for any given system, the use of the particle-mesh method in this report does not act as an input into the MHD code. Instead, the outputs from the Athena MHD code are used to generate a drifted Maxwellian velocity distribution from which the velocities of the ions and electrons can be initialized in the geometry near the first mesh of the electrostatic analyzer.

Similar PIC methods have been used to simulate analyzers in ion-beam[53] and space plasma[54] environments, but, to the author's knowledge, no effort has been made to observe the effect of the sheath of a gridded analyzer subject to a highly transient plasma load, such as that generated in TELS. The PIC will capture the sheath physics of the fully-ionized plasma as it bombards the initial, floating metal mesh or slit.

The intention of this chapter is to summarize the efforts taken toward developing a comprehensive model used to simulate the extraction of ion information in the TELS device using a retarding field energy analyzer (RFEA). This model will include the work done in generating the distribution using the ATHENA MHD code, as well as the work done in developing the appropriate field solver to further track particles as they traverse the analyzer geometry. Further documentation for each code, as well as the analysis codes used with experimental results, can be found in the Appendices to this report. The actual codes themselves can be found electronically through the appropriate channels in the Department of Nuclear, Plasma, and Radiological Engineering at the University of Illinois at Urbana-Champaign.

2.2 Athena MHD

2.2.1 Athena Setup

Athena MHD is generally used to solve the compressible, adiabatic, inviscid MHD equations. With the proper functionalities set, it can solve the resistive MHD equations, but is often used for the assumed ideal MHD conditions, which is the case for the transient TELS plasma[2]. These equations in the ideal form can easily be derived from momentum and energy conservation, the continuity equation, and Maxwell's equations[2, 50]:

$$\frac{\partial \rho \vec{v}}{\partial t} + \nabla \cdot \left(\rho \vec{v}\vec{v} - \vec{B}\vec{B} + \overleftrightarrow{P}^*\right) = 0 \tag{2.1}$$

$$\frac{\partial E}{\partial t} + \nabla \cdot \left[\left(E + \overleftrightarrow{P}^*\right)\vec{v} - \vec{B}\left(\vec{B} \cdot \vec{v}\right)\right] = 0 \tag{2.2}$$

$$\frac{\partial \rho}{\partial t} + \nabla \cdot (\rho \vec{v}) = 0 \tag{2.3}$$

$$\frac{\partial \vec{B}}{\partial t} - \nabla \times \left(\vec{v} \times \vec{B}\right) = 0 \tag{2.4}$$

where ρ is the mass density, $\vec{v}$ is the bulk velocity, $\vec{B}$ is the magnetic field, E is the energy density defined by:

$$E = \frac{P}{(\gamma - 1)} + \frac{1}{2}\rho v^2 + \frac{B^2}{2} \tag{2.5}$$

where γ is the adiabatic constant of the fluid, and $\overleftrightarrow{P}^*$ is the pressure tensor, which is a diagonal tensor with the following terms along the diagonal:

$$P^* = P + \frac{B^2}{2} \tag{2.6}$$

Each of the primary equations listed in Eq. (1) through Eq. (4) can be simplified to a hyperbolic, flux-conserving form:

$$\frac{\partial \vec{c}}{\partial t} + \nabla \cdot \vec{F} = 0 \tag{2.7}$$

where $\vec{c}$ contains the values of interest and $\vec{F}$ is the flux vector operating on those values. The unique part about Athena is that it solves this series of four hyperbolic equations using a higher order Godunov method in order to apply mesh refinement. The Athena Godunov method breaks

the series down into three steps: (1) generate a predictor solution by advancing all eigenvalues in a small Δt, (2) Solve the Riemann problem using an HLLD scheme[2, 50], and (3) reconstruct the state vector at all points in the domain. The predictor step can use methods such as the Corner Transport Upwind scheme, which can be simply illustrated in a one-dimensional form as:

$$c_i^{n+1} = c_i^n - \frac{\Delta t}{\Delta x}(F_{i+1/2}^n - F_{i-1/2}^n) \tag{2.8}$$

where the flux terms are found at the half spatial step, which leads to further interpolation between the i-1 and i+1 nodes. This, along with other fluid schemes, are characteristically dependent on the Courant-Friedrichs-Lewy (CFL) number associated with the ratio of the time step to the spatial step for stability, $\alpha = \nu\ \Delta t/\Delta x$, where the term ν resembles an advection-type coefficient.

As is the case in any computational or theoretical analysis, the application of the appropriate boundary conditions is important for Athena stability. The Athena MHD code comes preset with four different boundary types that can be called from the input script. These conditions include: (1) a reflecting condition of both the momentum and magnetic field, (2) a flow out conditions of both the momentum and magnetic field, (3) a user defined boundary condition, and (4) a periodic condition of both the momentum and magnetic field. Typically, Athena simulations are run in Cartesian systems due to the complexity surrounding the changing of the Jacobian in other systems, but has the capabilities of running two dimensional simulations relatively accurately in cylindrical coordinates, which was the system used for modeling the TELS plasma. The boundary conditions thus applied to the TELS geometry were: (1) flow out at the axial boundaries, (2) periodic at the angular boundary, (3) momentum and magnetic field reflection at the r = 0 boundary, and (4) momentum reflection at the r = R boundary[2]. These boundaries, along with the positions of the θ coils and the guiding field coils can be seen in Fig. 2.1.

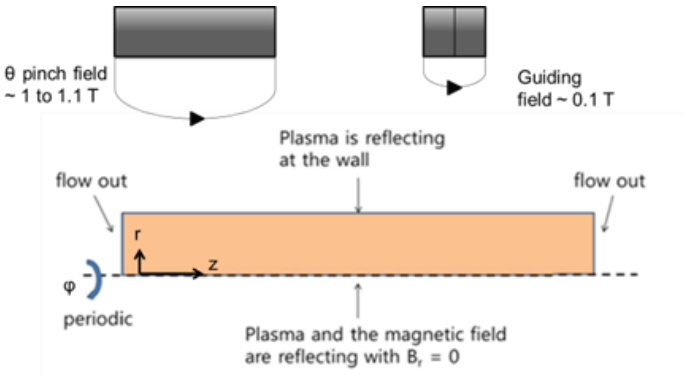

Figure 2.1: A depiction of the Athena domain along with the appropriate boundary conditions [1].

As for specifics pertaining to the simulation, the domain was discretized into 50 cells in the radial direction, 100 cells in the axial direction and 2 cells in the angular direction, since the simulation is primarily assumed axisymmetric. The physical domain with which this simulation replicates is roughly 1 m in the axial direction, 5 cm in the radial direction, and π radians in the angular direction. With these spatial steps in mind, the time step was set to be, initially, 0.1 ns in order to maintain the CFL number at 0.5[2]. This CFL number corresponds to a numerically stable simulation for the predictor step of the Godunov scheme. The simulations performed in Ref. [2] were replicated in order to extract the appropriate velocity distribution functions in each direction to initialize the particles the PIC collimator code, explained in detail in the following sections.

The plasma is initiated as a bulk fluid in the axial region that aligns with the theta pinch magnets. Initially, the plasma only fills approximately half of the domain in the radial direction. Because the Athena MHD code operates in cgs units, all properties used as initial values for the plasma were modified from those measured experimentally. The plasma was initialized with a mass density of 1.1×10^{-8} g cm^{-3}, a kinetic pressure of 30 kBa ~ 3 kPa, and an initial velocity in the axial direction of 4×10^{6} cm s^{-1} [2]. The compressing magnetic field from the theta pinch is initially locally concentrated near the wall and progresses toward the condition where the field is at its maximum field penetration depth and is then reflected[2].

2.2.2 Athena Results

Athena results were obtained using two different platforms. A series of Athena simulations were run on the University of Illinois Campus Cluster, while one full simulation was run on a separate personal computer (PC). The reason for this was that even though the simulation is numerically stable, there are issues regarding magnetic flux conservation at the r = R boundary leading to an unnecessary amount of mesh refinement. These issues were previously stated in Ref. [2]. The simulation on the PC ran for a total time of 6.67 μs before hitting the total cycle limit, while those ran on the cluster did not reach this level of completion even after using a large number of processors and having a wall clock time of greater than 10 hours. The results of the Athena simulation run on the personal computer, depicted up to 2.5 μs, are depicted in Fig. 2.2.

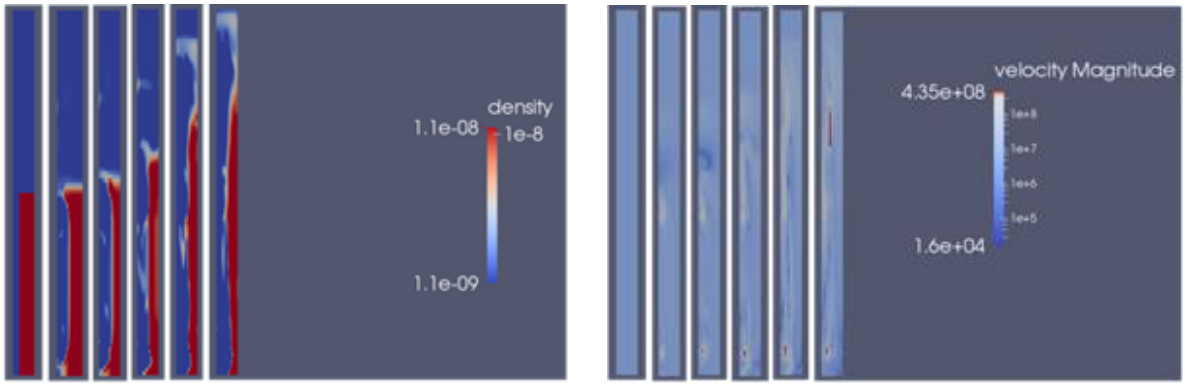

Figure 2.2: (Left) A depiction of the density profile at 0, 0.5, 1, 2, and 2.5 μs. (Right) A depiction of the velocity profile at 0, 0.5, 1, 2, and 2.5 μs.

From a single point in the target region at 2.44 μs, data was extracted to generate a set of drifted Maxwellian velocity distributions. This time was chosen out of the full time domain of the Athena MHD simulation because all the measured plasma parameters were close to those measured experimentally. This point in the domain was important because it was representative of the position of the center of the analyzer, physically. The reason data was extracted from this specific simulation time was that the densities, temepratures, and velocities were all more consistent with experimental results gathered from Ref. [2]. Ideally, the PIC would use time-varying inputs, or production runs would be made for different inputs corresponding to different

times in the Athena time domain. This will be one of the topics for future work. The outputs from the Athena simulation as a function of time can be seen in Fig. 2.3 and Fig. 2.4.

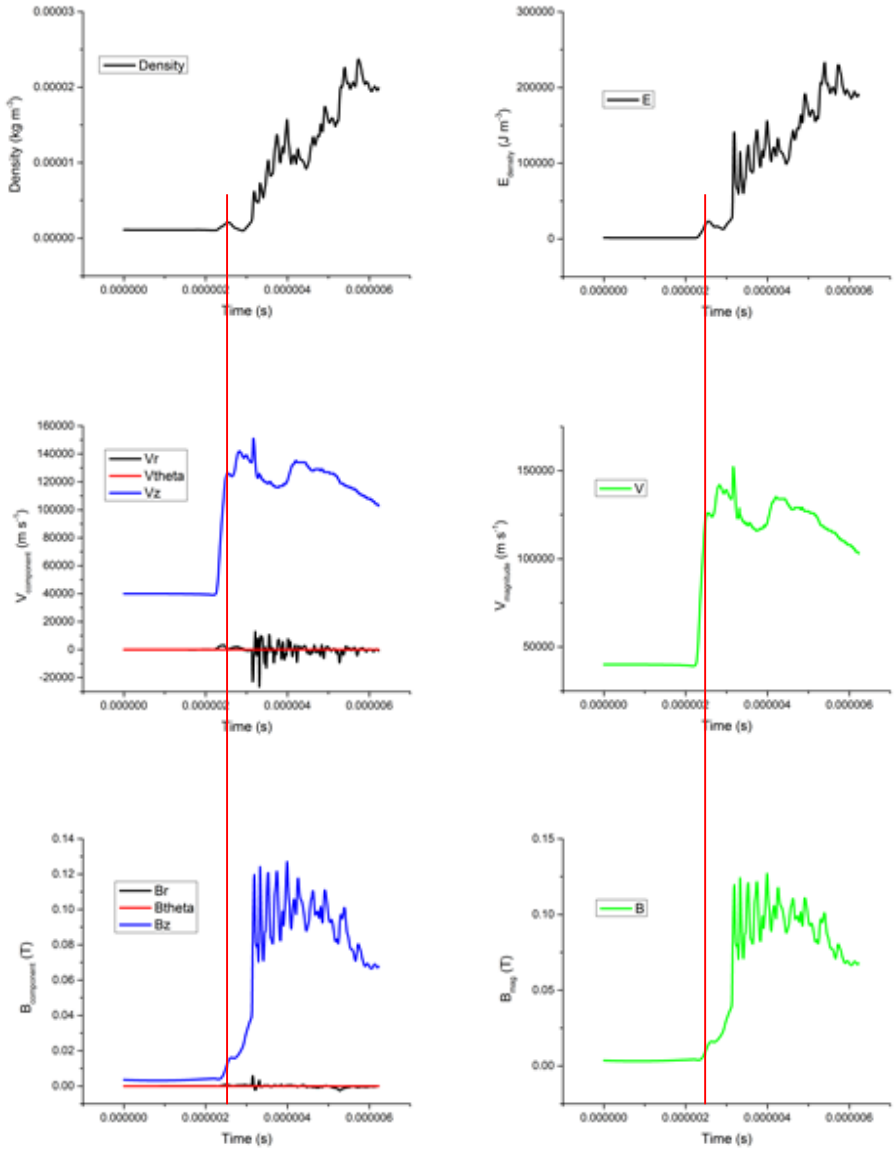

Figure 2.3: (Top left) Athena mass density output vs. time. (Top right) Athena energy density output vs. time. (Middle left) Athena velocity component output vs. time. (Middle right) Athena velocity magnitude output vs. time. (Bottom left) Athena magnetic field component output vs. time. (Bottom right) Athena magnetic field magnitude output vs. time. The red lines indicate the point in time from which data was extracted to generate the initial velocity distribution for the kinetic particle mesh code. All quantities increase at a single point in the target region over time based on the translation of the plasma and the time in which it arrives at this single target point.

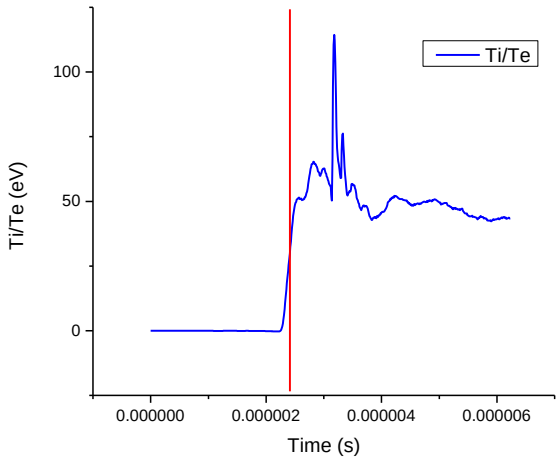

Figure 2.4: The electron and ion temperature values in thermal equilibrium as a function of time. The red line indicates the point in time from which data was extracted.

Velocity distributions were then sampled from in the initialization phase of the PIC and the appropriate masses and charges for each particle, considering singly electrons and singly charged hydrogen ions, were applied. The Maxwellian velocity distribution rotated from cylindrical coordinates to Cartesian coordinates, where the x-direction drift velocity used the z-direction drift velocity output from the Athena simulation, can be seen in Fig. 2.5. These profiles are representative for how the velocities were sampled for each charged particle type.

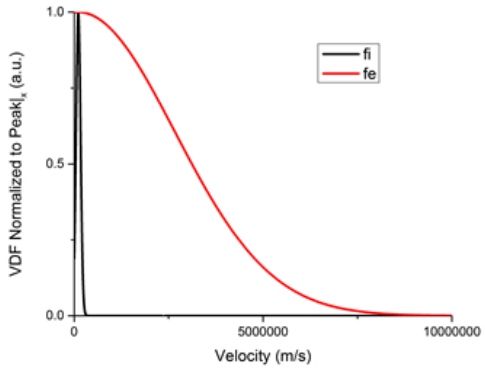

Figure 2.5: The velocity distribution functions normalized to the peak value as sampled from to initialize particle velocity in the x-direction.

From the Athena results, T_e and T_i were found to be approximately 37.16 eV, $v_{x,drift}$ was found to be 1.09 x 10^5 m s^{-1}, $v_{y,drift}$ was found to be 3130 m s^{-1}, and $v_{z,drift}$ was found to be -0.0115 m s^{-1}. The x, y and z components were rotated from the cylindrical frame to the Cartesian frame, where the velocity in z in the cylindrical frame corresponds to the velocity in x for the Cartesian frame. The temperatures were calculated by first finding the energy density at the target point at the appropriate time. This energy density value corresponds to the summation of the kinetic, pressure, and magnetic pressure components. Subtracting out the component of magnetic pressure and dividing through by the number density calculated from the mass density assuming a hydrogen plasma, the temperature of the plasma fluid was obtained. With this total temperature and applying the concept of thermal equilibrium, half of this temperature was applied to the electrons and half to the ions.

One of the key aspects of this computational work is the coupling of the MHD outputs to the PIC as inputs. As described in the previous paragraph, the data at a specific time in the MHD domain was extracted and used as an input for the PIC injected particles. A full coupling would utilize the Athena outputs as functions of time, so that they would act as dynamic inputs into the PIC code. While this would complete the simulation coupling in a way that has not been accomplished before, this coupling is not without its issues. Primarily, the fact that the two simulations operate on drastically different time steps, even though the time domains are similar, leads to the need to interpolate Athena output values for every time step in the PIC. The outputs cannot be simply fit to a trend either, as can easily be seen from Fig. 2.3 and Fig. 2.4. A more accurate way of observing the effects on the collimating grid would be to take the Athena outputs at various times through its simulation domain, extract the necessary data for those times, and use those data as distribution function inputs into the PIC. This would require numerous PIC production runs, however, and may become quite computationally expensive.

2.3 Kinetic Particle Mesh Under Development

2.3.1 Particle Mesh Setup Under Development

The PIC code developed in an attempt to simulate the kinetic effects of the transient TELS plasma incident on the primary collimating grid of the RFEA was a 2 ½ dimensional

simulation, where the fields were found on a two-dimensional square mesh and extended infinitely in the z-direction and the particles were moved in all three dimensions. This setup was able to allow capture of the magnetic field effects on charged particle trajectories.

The fields at the nodes were solved using Poisson's equation and the relationship between the electric field and the potential:

$$\nabla^2\varphi = \frac{-\rho}{\varepsilon_0} \tag{2.9}$$

$$\vec{E} = -\nabla\varphi \tag{2.10}$$

where φ is the potential, ρ is the charge density, and ε_0 is the vacuum permittivity. The two dimensions in the Cartesian coordinate frame, the Laplacian of the potential is given by:

$$\nabla^2 = \frac{\partial^2}{\partial x^2} + \frac{\partial^2}{\partial y^2} \tag{2.11}$$

This Laplacian can be discretized using the following Taylor expansions for the second derivatives:

$$\frac{\partial^2\varphi}{\partial x^2} = (\varphi_{i+1,j} - 2\varphi_{i,j} + \varphi_{i-1,j})/\Delta x^2 \tag{2.12}$$

$$\frac{\partial^2\varphi}{\partial y^2} = (\varphi_{i,j+1} - 2\varphi_{i,j} + \varphi_{i,j+1})/\Delta y^2 \tag{2.13}$$

where $\Delta x^2 = \Delta y^2 = h^2$. These discretized forms were then put into a matrix that corresponds to an $A \cdot x = b$ formulation in the form:

$$\bar{\bar{A}} \cdot \bar{\varphi} = \frac{-\rho}{\varepsilon_0} \tag{2.14}$$

where the $\bar{\bar{A}}$ matrix corresponds to the discretized Laplace operator having the typical form with -4 along the diagonal, and 1's along the first superdiagonal, the first subdiagonal, the n^{th} superdiagonal, and the n^{th} subdiagonal. The rows corresponding to the boundaries were further modified with different stencils.

Once the potential field was found, Eq. (2.10) was discretized and solved to find the electric field at the nodes. The components of the field were solved for by using a central

difference scheme within the computational domain, a forward difference scheme at the boundaries corresponding to zero in both the x- and y-directions, and a backward difference scheme at the boundaries corresponding to the final length in both directions.

The setup of the particle mover portion of the code dealt with advancing the positions and velocities in time using the charged particle equations of motion:

$$\frac{d\vec{v}}{dt} = \frac{q}{m}\,\vec{E} + \frac{q}{m}(\vec{v} \times \vec{B}) \tag{2.15}$$

$$\frac{d\vec{x}}{dt} = \vec{v} \tag{2.16}$$

where $\vec{x}$ is the general position vector of the particle, $\vec{v}$ is the velocity vector for the particle type in question, q is the charge of the particle type, m is the mass of the particle type, $\vec{E}$ is the electric field felt by an individual particle, and $\vec{B}$ is the magnetic field felt by a particle. The particle positions were advanced in time using a central difference scheme, while the particle velocities were advanced in time using a forward difference scheme. As will be touched on again in the following section, this particle mover may be a cause for error in the simulation based on the differences in the order of the particle mover. This subroutine is still under development in an attempt to employ a more robust leapfrog method to get rid of any numerical instabilities caused by the discrepancy in order of the particle mover. In three dimensions and with a uniform magnetic field assumed to only be applied in the x-direction, this led to the set of equations corresponding to:

$$x_{n+1} = x_n + dt\left(v_{x,n} + \frac{dt}{2}\left\{\frac{q}{m}\,E_{x,n}\right\}\right) \tag{2.17}$$

$$y_{n+1} = y_n + dt\left(v_{y,n} + \frac{dt}{2}\left\{\frac{q}{m}\left[E_{y,n} + B_{x,n} \cdot v_{z.n}\right]\right\}\right) \tag{2.18}$$

$$z_{n+1} = z_n + dt\left(v_{z,n} + \frac{dt}{2}\left\{\frac{q}{m}\left[-B_{x,n} \cdot v_{y,n}\right]\right\}\right) \tag{2.19}$$

$$v_{x,n+1} = v_{x,n} + dt\left(\frac{q}{m}\,E_{x,n}\right) \tag{2.20}$$

$$v_{y,n+1} = v_{y,n} + dt\left(\frac{q}{m}\left[E_{y,n} + B_{x,n} \cdot v_{z.n}\right]\right) \tag{2.21}$$

$$v_{z,n+1} = v_{z,n} + dt(\frac{q}{m}\,[-B_{x,n} \cdot v_{y.n}]) \tag{2.22}$$

Connecting the field solver to the particle mover required the use of a weighting scheme in order to first weight the contribution of each particle to the surrounding nodes for the charge density, and then to weight the solved electric field components at the nodes back to the particles in order to apply the above equations of motion. This was done using a linear Cloud-in-cell (CIC) weighting scheme, where the co-volume surrounding the node was found to be:

$$V = \frac{h^2}{3} \tag{2.23}$$

To finalize the setup of the PIC model, the appropriate spatial step and time step had to be applied. The time step had to be small enough to appropriately capture the electron movement, being smaller than the electron cyclotron frequency for the simulated density and temperature. Therefore, the time step was set at 1 ps for a total time domain of 1 μs for the mesh simulations. Since the spatial domain was limited for a separate simulation with a slit collimator, the time step was further limited to 100 fs for a total time domain of 1 μs. The spatial step is limited by the electron Debye length:

$$\lambda_{De} = (\varepsilon_0 k_b T_e \,/\, q_e^2 n_e)^{1/2} \tag{2.24}$$

where k_b is the Boltzmann constant, T_e is the electron temperature, q_e is the electron charge, and n_e is the electron density. The spatial size can be modified by a number of factors including the particle-to-computation (p2c) ratio which defines the contribution of a virtual particle vs. a physical particle, the number of particles initiated in the domain, and the rate of particle generation in the source term.

The PIC code required careful consideration for the boundary conditions. The real RFEA is a cylindrical body, so to retain in part some of the qualities the upper and lower boundaries in the y domain were set as periodic, both in the particle position and in the discretization of the field solver. This modified the $\bar{\bar{A}}$ matrix rows corresponding to these nodes to have the Taylor expanded form of:

$$\frac{\partial^2 \varphi}{\partial y^2}|_{j=0} = (\varphi_{i,1} - 2\varphi_{i,0} + \varphi_{i,N_g-1})/h^2 \tag{2.25}$$

where N_g is the number of spatial grid points and this expansion is taken at the nodes corresponding to the bottom boundary of the domain using a ghost cell for periodicity. Alternately, at the nodes corresponding to the top boundary, the expansion becomes:

$$\frac{\partial^2 \varphi}{\partial y^2}|_{j=N_g-1} = (\varphi_{i,0} - 2\varphi_{i,N_g-1} + \varphi_{i,N_g-2})/h^2 \tag{2.26}$$

This periodicity, however, is not true periodicity in that the top and bottom boundary fields are not equivalent. Instead, there lies a ghost cell in between the two from which contributions are applied to each of the boundaries. This is a problem when considering how the particle boundaries behave, where particles are truly periodic at these boundaries and are not allowed to exist in this ghost region. As was the case with the particle mover subroutine, this portion of the simulation is still under development and needs to be rectified in future work to eliminate large numerical instabilities. More will be explained as to the effect of this issue in the following section, and future work will modify the $\bar{\bar{A}}$ matrix seem in Fig. 2.6.

The boundaries in the x domain were set as Dirichlet conditions with the left most boundary corresponding to a zero potential and the right most boundary held at a potential corresponding to the potential applied to the electron repelling grid of the RFEA. This was usually set to be either -54 V or -100 V. The modification to the matrix solution was simple, with the rows corresponding to the appropriate boundaries being changed to all zeros, except for 1's along the diagonal components. A visualization of the $\bar{\bar{A}}$ matrix can be seen in Fig. 2.6.

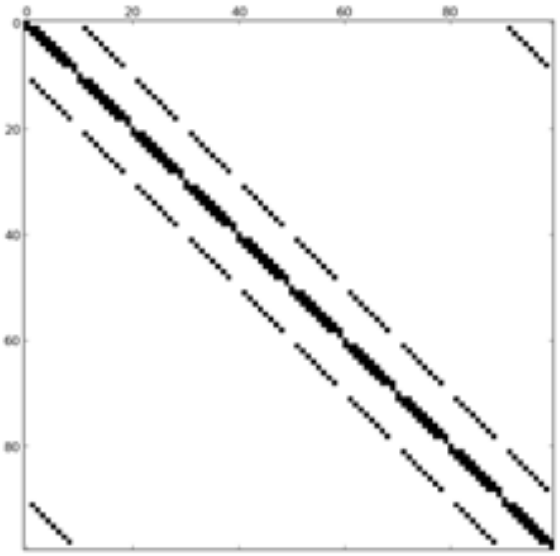

Figure 2.6: A visualization of the Laplacian matrix used to solve for the fields. This image represents an N_g of 10, where the Laplacian is on a 100 x 100 cell setup.

To complete the picture of the initialization setup, both electrons and singly charged H^+ species were initialized with a random position in the y domain and a random position uniformly spaced over the furthest left 100 microns in the x domain. The velocities of these particles were initialized after having found the appropriate drifted Maxwellian velocity distribution functions in each coordinate and transforming those to Cartesian coordinates:

$$f = n(\frac{m}{2\pi kT})^{\delta/2}\exp[\frac{-m(v-v_d)^2}{kT}] \tag{2.27}$$

where n is the density of the particle type, m is the mass of the particle type, δ is the number of dimensions used, v_d is the drift velocity found for a given component from the Athena simulation, and T is the temperature corresponding to the particle type. Electrons and ions in this case were assumed to be in thermal equilibrium at a temperature of 37.16 eV, with the plasma considered to fully ionized. The bulk drift velocities of the Maxwellian drifted distributions in each direction are described in the previous section. The values used to initialize these velocities were extracted from a point corresponding to the physical target region of TELS at 2.44 μs into the Athena simulation.

The Athena MHD simulation takes into account the bulk contributions to and from the plasma and the transportation of the plasma from the theta pinch region to the target region. The kinetic effects of the sheath, however, require the use of a separate technique since bulk fluid codes do not capture kinetic effects well. This is the reason that Athena outputs were used as inputs into the PIC, where the sheath is established in a transient fashion and the field solvers controlling the local field and potential values solve for the sheath potential drop from the incoming plasma through the collimating grid. Here, the bulk plasma potential would be inherent in the way the bombarding plasma is initialized, particles are recycled, and interactions with the physical grid barriers are controlled, and a defined plasma potential input is not necessary. This will be more evident once future work has been completed to eliminate sources of error within the simulation domain, and will be discussed more in the following section.

The final, and most characteristic, portion of the PIC domain setup pertained to the way the collimator geometry was defined. The collimator thickness was set equivalent to the size of 1 spatial step and particles that interacted with the mesh were immediately killed. Two different "kill" conditions were defined that have realistic meaning. First, the mesh acted solely as a physical barrier with no charge accumulation, as would be the case for a grounded collimator. Second, the mesh was allowed to build up charge as particles bombarded the surface, thus modifying the electric field around the mesh. Particles crossing the right boundary were recycled and reinitialized as a source. In all cases, particles crossing the right boundary were tallied in order to know how the different collimator types affected the number and type of particles traversing through the rest of the analyzer. A full depiction of the boundary and setup to the PIC can be found in Fig. 2.7.

The collimator geometry was later modified in an effort to mimic the later iterations of the experimental setup, whereby the collimating mesh was later changed to a slit on the order of Debye length in TELS. This had the effect of significantly modifying the "kill" condition for the particles at the collimator boundary. In this simulation, the right boundary was held at -100 Vdc in order to make sure that a significant portion of the higher energy electrons were screened from crossing the right boundary and affecting the statistics of the simulation output. The modified PIC domain can be seen in Fig. 2.8.

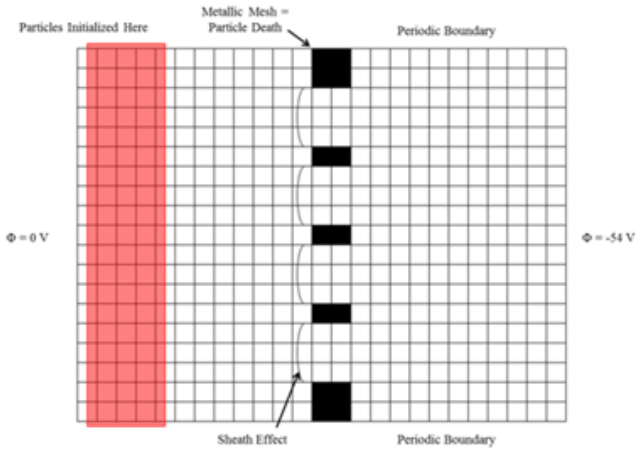

Figure 2.7: An image depicting the electric field domain in two dimensions. A constant magnetic field of 0.01 T was applied in the x-direction to every particle.

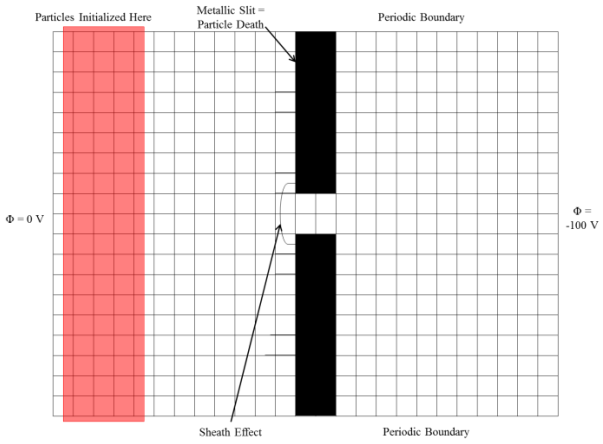

Figure 2.8: An image depicting the electric field domain in two dimensions for a collimating slit. A constant magnetic field of 0.01 T was applied in the x-direction to every particle.

The implementation of the PIC code required finding the initial particle positions and velocities, setting up the appropriate electric field pertaining to each particle using the CIC weighting scheme, advancing each particle in time using the equations of motion, and repeating the cycle. While the equations of motion were easily solved for using the previously defined schemes, the potentials were solved using a subroutine to solve a linear system with a general matrix using real double precision arithmetic, or DGESV. This is the built-in Python solver used on problems like the one illustrated in Eq. (2.14), and uses LU decomposition with partial pivoting and row interchanges to factor the $\bar{\bar{A}}$ matrix[55].

2.3.2 Preliminary Particle Mesh Results Under Development

The results presented in this section are from a prototype particle mesh simulation and must be considered very critically as they are the consequences of a work in progress. Further development of the simulation must be done in order for the results presented here to bear any physical meaning or have any correlation to experimental conditions. The errors associated with this prototype simulation were briefly mentioned in the previous section, and will be highlighted throughout this section. Efforts, however, were taken to use the results generated from this work-in-progress model in the next portion of the computational work, but the results listed in this section by no means are conclusive. Care must be taken to avoid correlating these results to any physical effect, since the sheath is not established properly in this prototype simulation. These issues will also be discussed in the concluding remarks to this chapter.

Two sets of conditions were initially used in order to generate the results presented in this section. Primarily, most variables did not vary between these two simulation runs, except for the potential applied to the right most boundary. A third simulation with a collimating slit and a right boundary held at -100 V is also presented here. As mentioned before, the right-most boundary corresponds to the physical position just before charged particles come into contact with the electron repelling grid. For all simulations presented here, the particle to computational ratio was set to a value of 100, meaning that each virtual particle contributed one hundred times the force to the overall electric field mesh solution than would be felt or contributed by an actual physical particle. Each of the mesh simulations was also held to a spatial grid size corresponding to a 4 millimeter domain being sampled by 41 grid steps in both dimensions, meaning that a single grid measured 97.5 x 97.5 square micrometers. The slit simulation, however, was reduced in size to a 400 micrometer domain using 41 grid steps, making a single grid 10 x 10 square micrometers. Since kinetic particle mesh codes are limited in spatial size by the electron Debye length, this corresponded to a density in the mesh simulations of 2.16×10^{17} m^{-3} and a density in the slit simulation of 2.00×10^{19} m^{-3}. These spatial scalers were chosen in order to reduce on computational intensity and in the hopes that the results would scale to the actual physical environment. While the reduction on computational intensity was apparent in from the results presented, the use of only 40 Debye lengths as a total domain size may be one of the root causes of error in prototype simulation. Within 40 Debye lengths, the presheath cannot be established

properly, meaning the criteria for particles entering the sheath are not met, apart from the fact the sheath is not at all established properly, as will be shown in Fig. 2.9, 2.10, and 2.11. Apart from these two constants between the computational experiments, the other parameter that was held constant was mesh size, with the thickness of the mesh being equivalent to 1 grid size and the aperture openings in the mesh also being equivalent to 1 grid size. The thickness of the collimating slit was held to 1 grid size and the slit opening was also held to 1 grid size.

The first mesh simulation uses an electron repelling potential of -54 V, while the second mesh simulation uses an electron repelling potential of -100 V. The slit simulation uses an electron repelling potential of -100 V. This was done in order to observe the effect on incoming charged particles, mainly the effect a higher electron repelling potential played on both the sheath physics happening at the collimating mesh and on the incoming electron population. The lower electron repelling potential should accelerate ions crossing the collimating apertures to be accelerated to a larger degree. A few snapshots from the results obtained by running the mesh simulations can be seen in Fig. 2.9 and 2.10. Snapshots from the results obtained by running the slit simulation can be seen in Fig. 2.11.

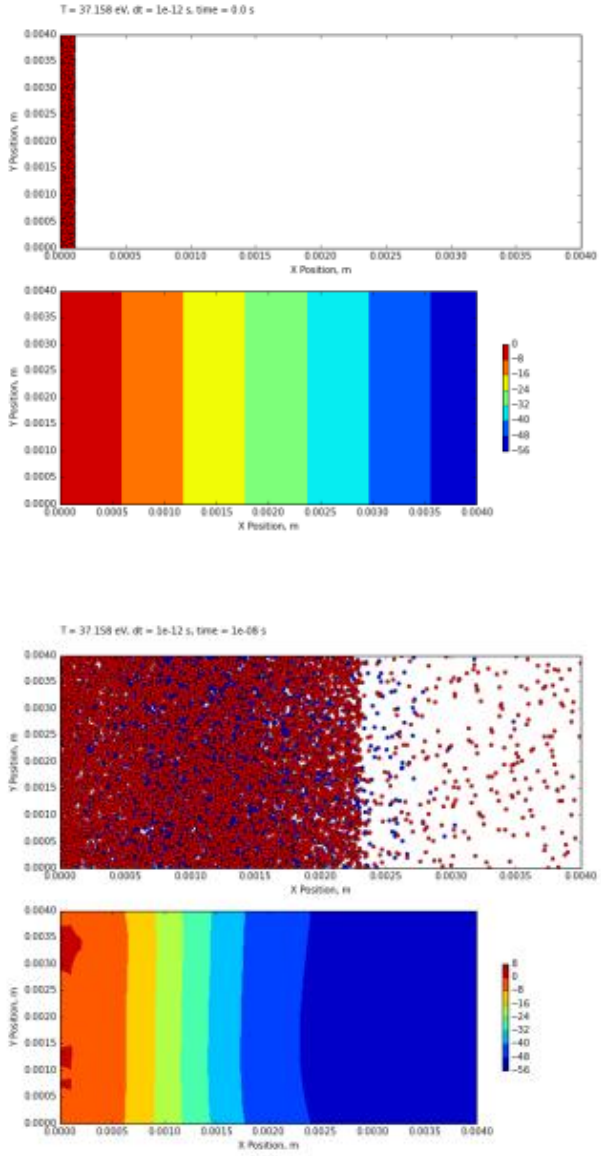

Figure 2.9: Snapshots of the simulation ran for an electron repelling potential of -54 V. The images above represent the results of the simulation at 0, 0.01, 0.05, and 0.1 μs. The red dots at the top indicate electrons, while the blue dots indicate ions. The establishment of some sort of electric barrier can be observed where after only a small portion of time (nearly 0.1 μs or less), nearly all of the electrons are being repelled. While this may seem analogous to some sort of sheath effect, in reality the sheath should be observed as menisci across the collimating apertures. Ion flux seems to remain constant over time only because of their mass relative to that of electrons, or possibly due to some sort of artificial diffusion.

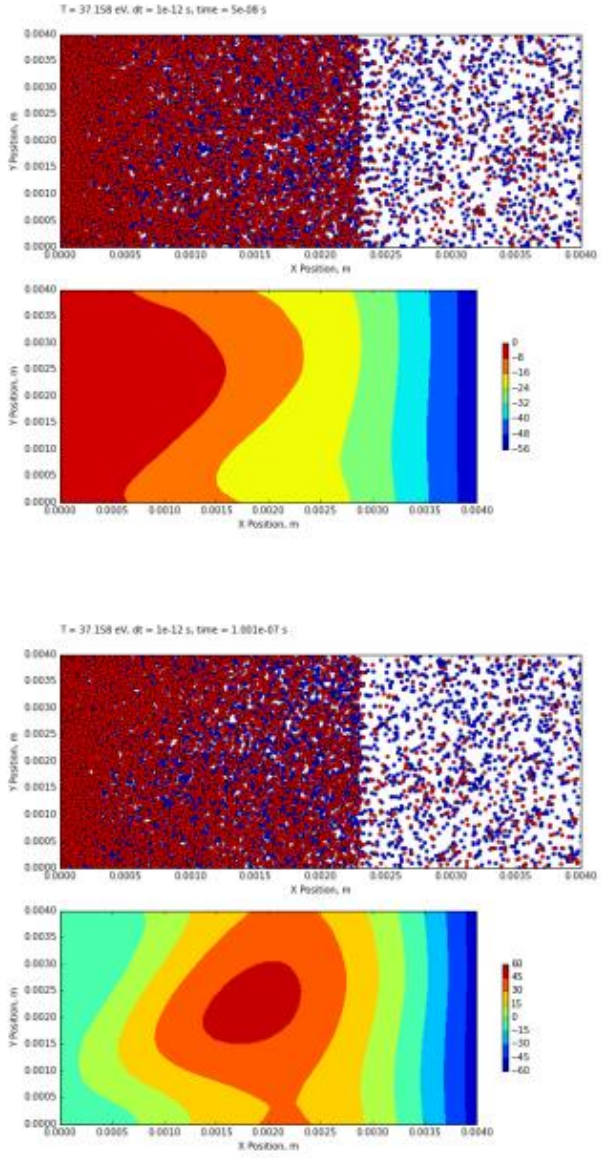

Figure 2.9 (cont.): These snapshots are a continuation of the description for the full set of figures described on the previous page.

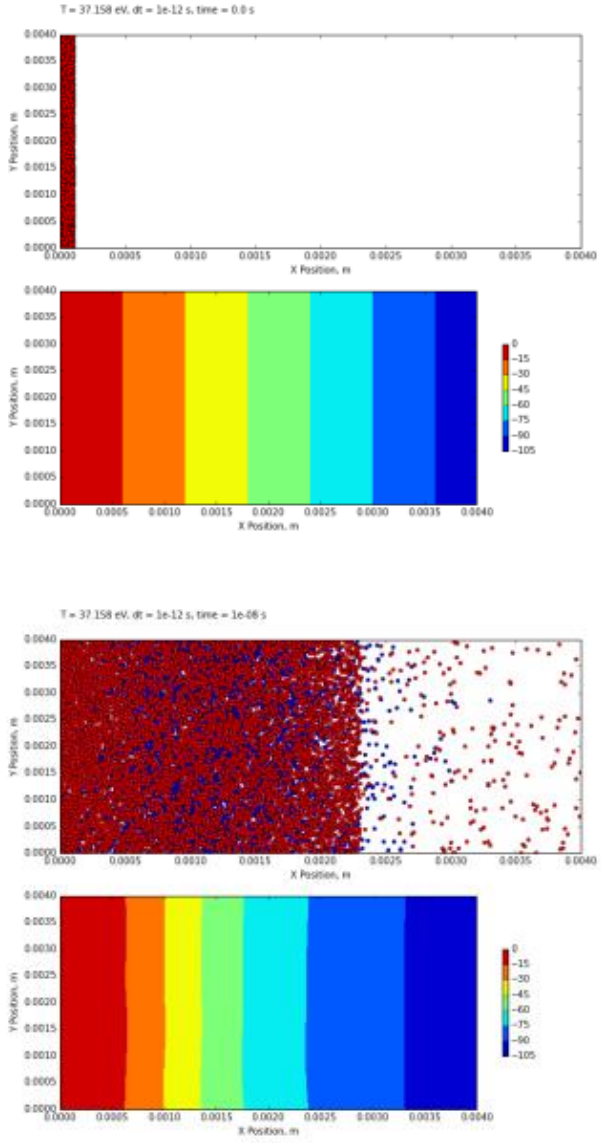

Figure 2.10: Snapshots of the simulation ran for an electron repelling potential of -100 V. The images above represent the results of the simulation at 0, 0.01, 0.025, and 0.05 μs. Similar to Fig. 2.9, the establishment of some sort of electric barrier is repelling a large number of electrons, but this cannot be directly compared to the establishment of any sort of physical sheath. In reality, what is shown is an artificial version of repelling Coulomb forces perturbed by the barrier established at the collimator. The model must be developed further in order to properly establish a sheath at the barrier boundary.

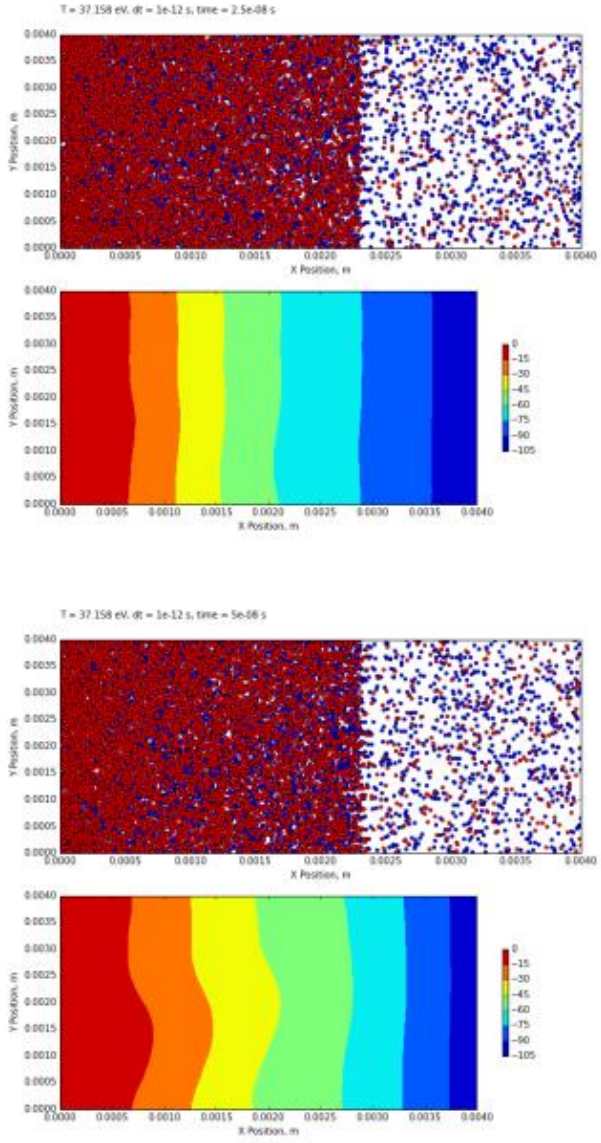

Figure 2.10 (cont.): These snapshots are a continuation of the description for the full set of figures described on the previous page.

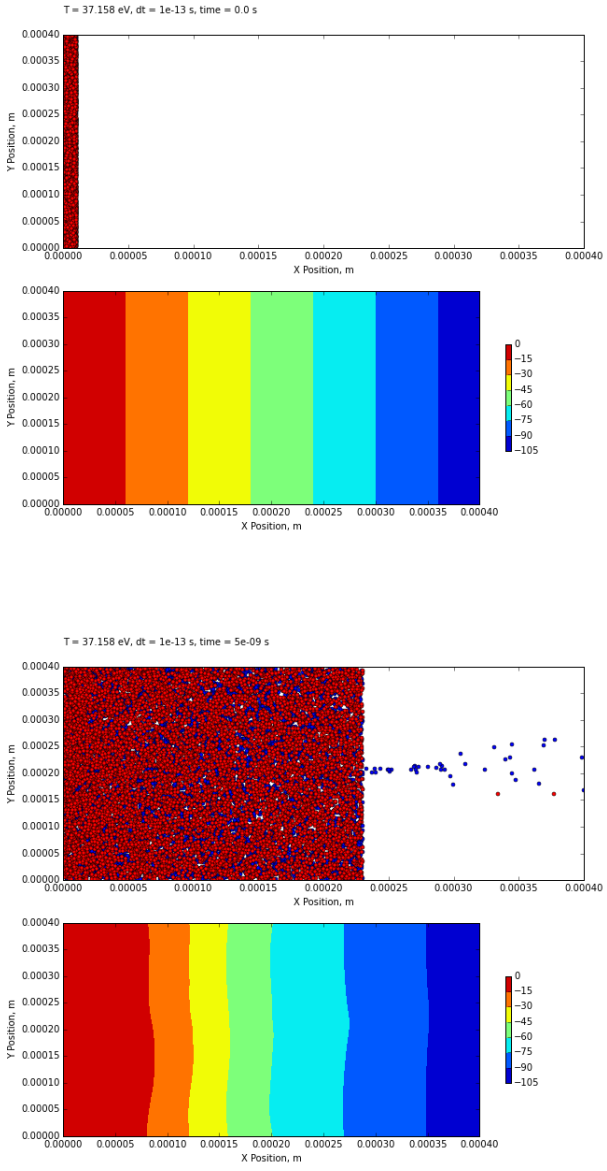

Figure 2.11: Snapshots of the collimating slit simulation ran for an electron repelling potential of -100 V. The images above represent the results of the simulation at 0, 0.005, 0.0101, and 0.025 μs. Similar to Fig. 2.9 and Fig. 2.10, the establishment of an electric barrier is noticeable here, but is by no means related to the establishment of a proper sheath potential.

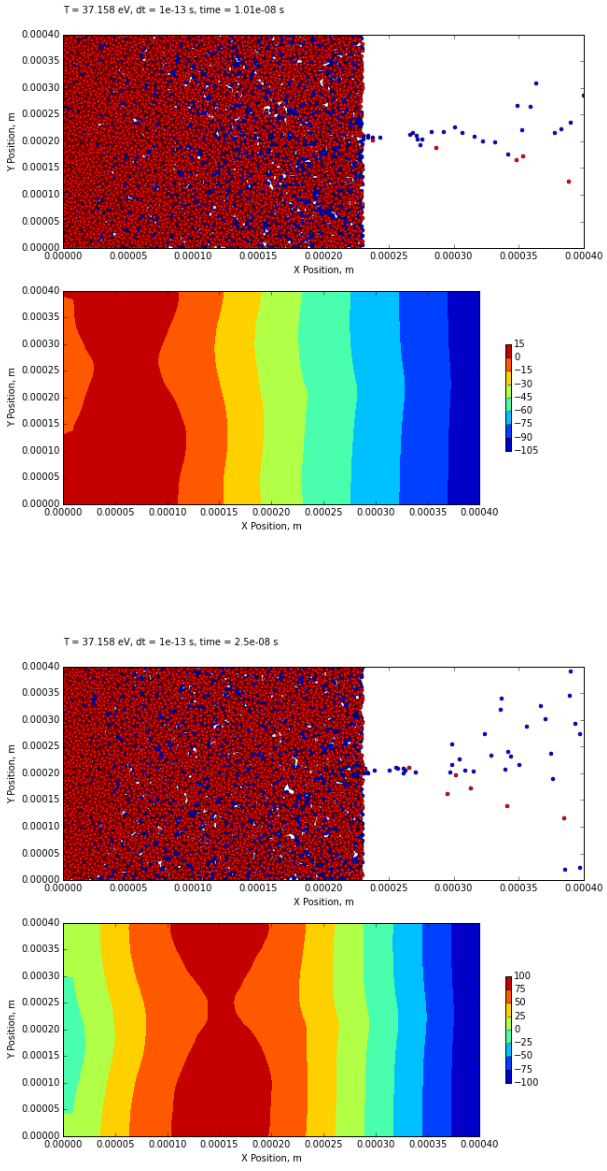

Figure 2.11 (cont.): These snapshots are a continuation of the description for the full set of figures described on the previous page.

While Fig. 2.9, 2.10, and 2.11 all show qualitatively a difference in the transmission of electrons and ions through the collimating barriers, one major issue is prevalent in the results of all three simulations. For the effective sweeping of the electrons to occur in any simulated domain, a sheath potential must be established across the mesh apertures or slit. This sheath takes the form in the contour plot of the potential as a meniscus like structure in front of the opening to the collimating barrier, as shown in Fig. 2.8. The potential contours shown in Fig. 2.9,

2.10, and 2.11 do not clearly indicate the formation of any well-defined sheath, which should be established within the first few tens of nanoseconds upon the arrival of the first set of electrons at the collimating barrier surface, specifically when considering hydrogen ions. The results presented in these figures should have easily accounted for the establishment of this sheath potential characteristic, evident in the potential contours, but all three sets of time-lapsed results show no apparent evidence of such a formation. As such, the electrons are not effectively screened from the simulated analyzer domain and continue to play a role in the Coulomb interactions and weighted fields past the collimating barriers, even when higher electron repelling potentials are applied. The results of the species crossing the right boundary, therefore, must be considered very critically, since this vital portion of the overall simulation scheme has a very significant problem that will be critical to future work endeavours.

Two different results can be used to gauge the effectiveness of the different potentials applied to the electron repelling grid. First, the total number of each particle crossing the right hand most boundary can give a clue if the simulation is providing accurate results in two different ways. If a higher flux of electrons as compared to ions crosses the right hand boundary, then there is a significant problem with how the collimator barrier is established. Errors in the setup of either the weighting scheme or the particle tracer can be the cause for a larger electron vs. ion flux. On top of this, problems with the differences in periodicity between particles and the fields play a chief role in developing numerical instability, which propagates through the domain over time. The comparisons of fluxes over time for both charged species for the cases where the electron repelling grid is held at -54 V and at -100 V can be seen in Fig. 2.12. To compare the effectiveness of a slit relative to a collimating mesh, the flux of the slit simulation is also illustrated in Fig. 2.12.

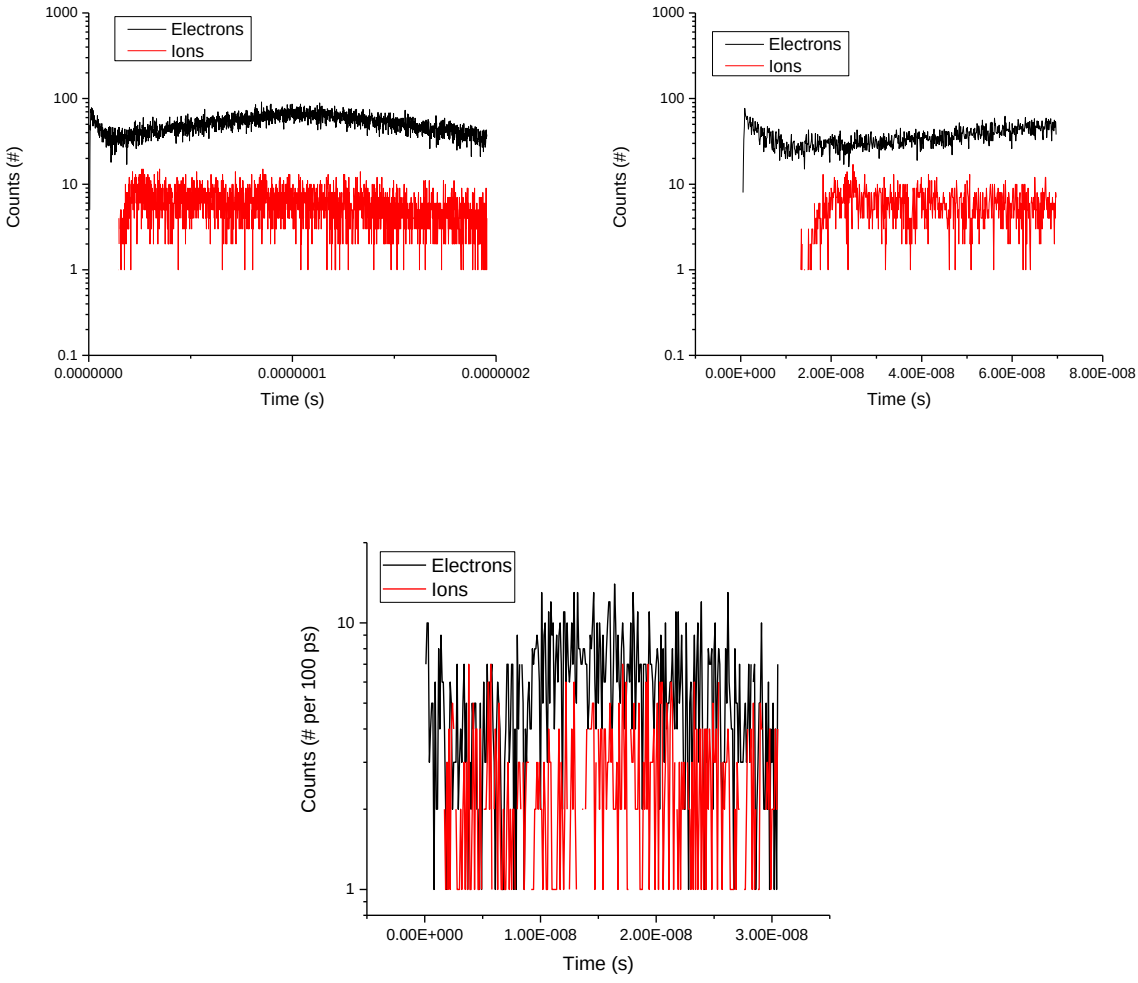

Figure 2.12: (Left) A comparison of electron and ion flux for the case of an electron repelling potential of -54 V. (Right) A comparison of electron and ion flux for the case of an electron repelling potential of -100 V. (Bottom) A comparison of the electron and ion flux for the case of a collimating slit and an electron repelling potential of -100 V. These flux values represent counts of particles crossing the right boundary with a line area of 4 mm per 100 ps. The slit analyzer flux values represent the counts of particles crossing the right boundary with a line area of 0.4 mm per 100 ps.

Fig. 2.12 shows that in all cases there is no well-defined sheath structure formed at the interface between the collimator and the incoming plasma. If the sheath were truly established, then it would be illustrated such that electron flux is high at the very beginning during the transience, but then decreases to almost zero after the sheath had been established as a steady-state potential barrier. The aforementioned error is also apparent from Fig. 2.9, Fig. 2.10, and Fig. 2.11, where the potential accumulation seems to be in error as the simulation progresses.

The high electron flux seen in Fig. 2.12 can be caused by errors in the spatial step size, whereby the total domain size must be extended to adequately encompass both the sheath and the presheath physics. More important, however, are issues that could pertain to how particle motion progresses or that the number of simulated particles is too small for the domain of interest. Apart from these two major issues with the progression of the simulation, the periodic boundaries occurring at the top and bottom of the two-dimensional spatial domain have discrepancies that could lead to numerical instability. This is due to issues that arise with how the particle is tracked beyond these boundaries versus how the fields at the top and bottom boundary nodes are generated periodically. If the particle leaves the top boundary at any point, it returns to the simulation domain at the bottom boundary at an identical point in the x-direction with the same velocity as when it left the top domain. The particle periodicity is truly a periodic boundary, whereas the field periodicity does not follow this pattern. The way the matrix is generated, the periodic condition calls for a ghost cell that occurs between the top and bottom boundary nodes. Not having particles able to fill this ghost space, but having contributions to the boundary nodes from the ghost space would lead to significant numerical issues.

The second way that results from these simulations can be gauged is by sampling the outflowing velocity distributions of both the ions and electrons that are able to traverse the collimating grid. The distributions for the ions were then used as an input into the particle tracing simulation, which will be outlined in the following section. The ion velocity distributions for all preliminary cases can be seen in Fig. 2.13.

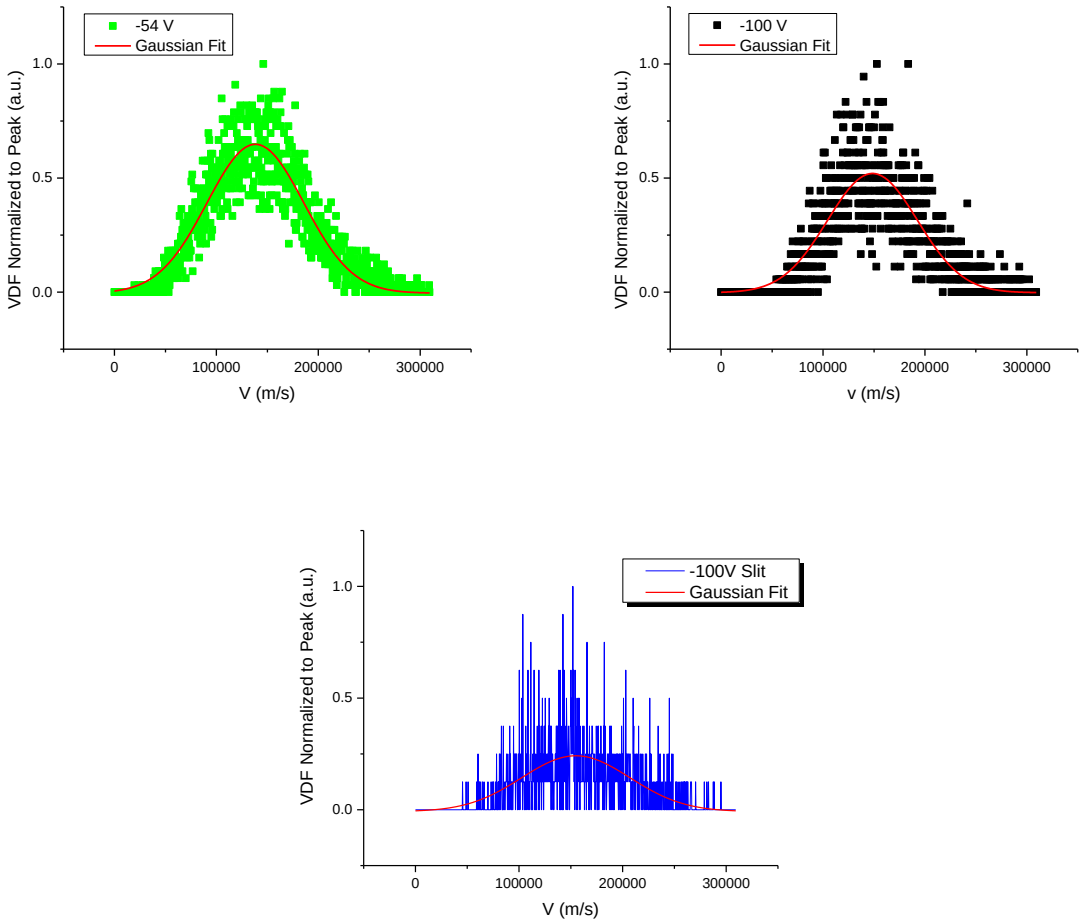

Figure 2.13: Ion velocity distributions for the cases of -54 V and -100 V for a collimating mesh and the case of -100 V for a collimating slit applied to the electron repelling grid in the direction normal to the collector. These distributions were fit to find the mean and standard deviation as an input into the COMSOL Multiphysics particle tracing simulation. The mean for -54 V electron repelling potential was nearly 1.38 x 10^5 m/s (99.4 eV), while the standard deviation was 4.75 x 10^4 m/s (11.8 eV). The mean for -100 V electron repelling potential was nearly 1.486 x 10^5 m/s (115.2 eV), while the standard deviation was 4.42 x 10^4 m/s (10.2 eV). The mean for the -100 V electron repelling potential for the collimating slit was nearly 1.55 x 10^5 m/s (125.1 eV), while the standard deviation was 5.23 x 10^4 m/s (14.3 eV).

The distributions illustrated in Fig. 2.13 are not very well resolved, especially when considering the total number of simulated particles that crossed the right-hand boundary. Statistically speaking, the binning of the velocities of each particle crossing the right-hand boundary of the domain should lead to much less noise in terms of generating an overall distribution from which the COMSOL simulation can sample. Other issues with these results are due to the problems raised in the previous paragraphs. These results are also entirely unphysical

in nature, since no sheath could be formed to adequately block or accelerate the different charged species in the system. While errors in the prototype particle-mesh simulation are clear from the unphysical results seen in Fig. 2.13, the work was used as a basis for an input in the COMSOL particle tracing module to illustrate how the whole of this computational work will eventually yield results once the particle mesh simulation has undergone significant revision.

In order to accurately summarize the results of the kinetic particle-mesh simulations, one must first take stock of flaws in the simulation. Observed in Fig. 2.9, 2.10, and 2.11, the sheath potential drop, in the form of a meniscus-like structure across the aperture of the collimating barrier, was not well established in any of the cases. This issue is a key point for further study, but current problems may have been caused by a number of underlying complications. First, the particle tracing portion of the simulation had a second-order, central difference scheme in position, but only a first-order forward difference scheme in velocity. A more accurate approach to this sub-routine would have been to use a leapfrog approach when advancing position versus velocity in time. Second, the spatial domain is not set up to adequately observe the trends that would otherwise be seen from both the presheath and the sheath. This will be modified in future iterations of the simulation. Third, there is a numerical discrepancy between the periodicity for the particles and the fields at the boundaries. The easiest approach to solving this problem would be to generate a new stencil along this boundary that does not require the use of a ghost cell outside the domain. Fourth, the number of particles sampled in this prototype simulation is too small to consider bulk movement of the plasma. Rather, individual charges are exerting forces on one another in this under-construction model. The remaining, and much less likely, problems raised in the kinetic particle-mesh simulation are due to problems in the collimating geometry, the spatial step size in the domain, and the electron repelling potential, all of which will be explored in detail in future work. For the case explained in this report, however, the unresolved distributions found in Fig. 2.13 will be used as an input into the COMSOL particle tracing simulation to illustrate how the future work will gather meaningful analyser results.

2.4 COMSOL Particle Tracing

2.4.1 Particle Tracing Setup

The final portion of the computational experiments used to simulate an ion energy analyzer in the TELS system was to trace the remaining ions as they traversed the remainder of the analyzer body. This required a Monte Carlo type approach, since particle mesh simulations are limited in spatial dimension. Past the collimating grid or slit, the Debye length is modified since a large portion of electrons are swept from the analysis, but a different particle tracing approach other than a cumbersome PIC simulation could be used for this analysis.

In light of this, the COMSOL Multiphysics[56,57] software was used to trace ions in two dimensions as they traversed the remainder of the analyzer body, modified by the potentials placed on the grids. Only ions were considered in this portion of the simulation in order to: 1) simulate more accurately the real-world condition with which the ions are subjected to interaction forces, and 2) to recover the appropriate information from the particle mesh simulation, which still requires development to properly simulate the sheath and meniscus at the collimating grid or slit. To this end, two modules out of the wide array of possible COMSOL physics modules were employed. Prior to employing the proper fields and following particles through those fields, however, the analyzer geometry and boundaries had to be established. The analyzer geometry is illustrated in Fig. 2.14.

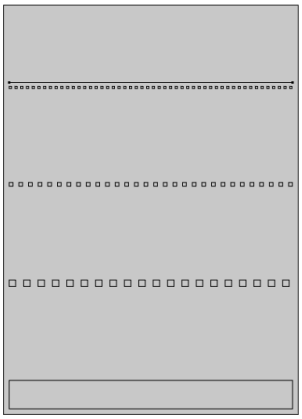

Figure 2.14: An illustration of the analyzer geometry generated in the COMSOL Multiphysics software. The collimating grid was not included in this simulation, since the physics should have been adequately handled by the particle mesh simulation and the outlet from the PIC simulation serves as the inlet into the COMSOL simulation. The plane above the top grid serves as the inlet for the particles in the particle tracing simulation.

As with the previous two simulations, the boundaries in this case are very important in establishing a relationship to the physical world. For both the field solution and the Monte Carlo type particle tracing solution, the left and right boundaries are set to periodic conditions. The top and bottom boundaries in the control volume are set to a zero potential, particle freezing condition. All mesh surfaces are set with a particle freezing condition, but the potentials are varied in accordance with the way the potentials are varied in the physical system. The fields are then solved using a variable finite element mesh based on the local geometry. The collector at the bottom is held at a zero potential and the face of the collector normal to the incoming particle flux is considered an outlet condition in the particle tracing module, where particles hitting this barrier are frozen to the surface and the statistics of these particles are noted in the output for the post-processing of the simulation. The setup of the mesh and the solutions to the electrostatic module for both cases are illustrated in Fig. 2.15. A magnetic field was not applied under the assumption that in the physical world the 430 ferritic stainless steel box would screen out the magnetic effects.

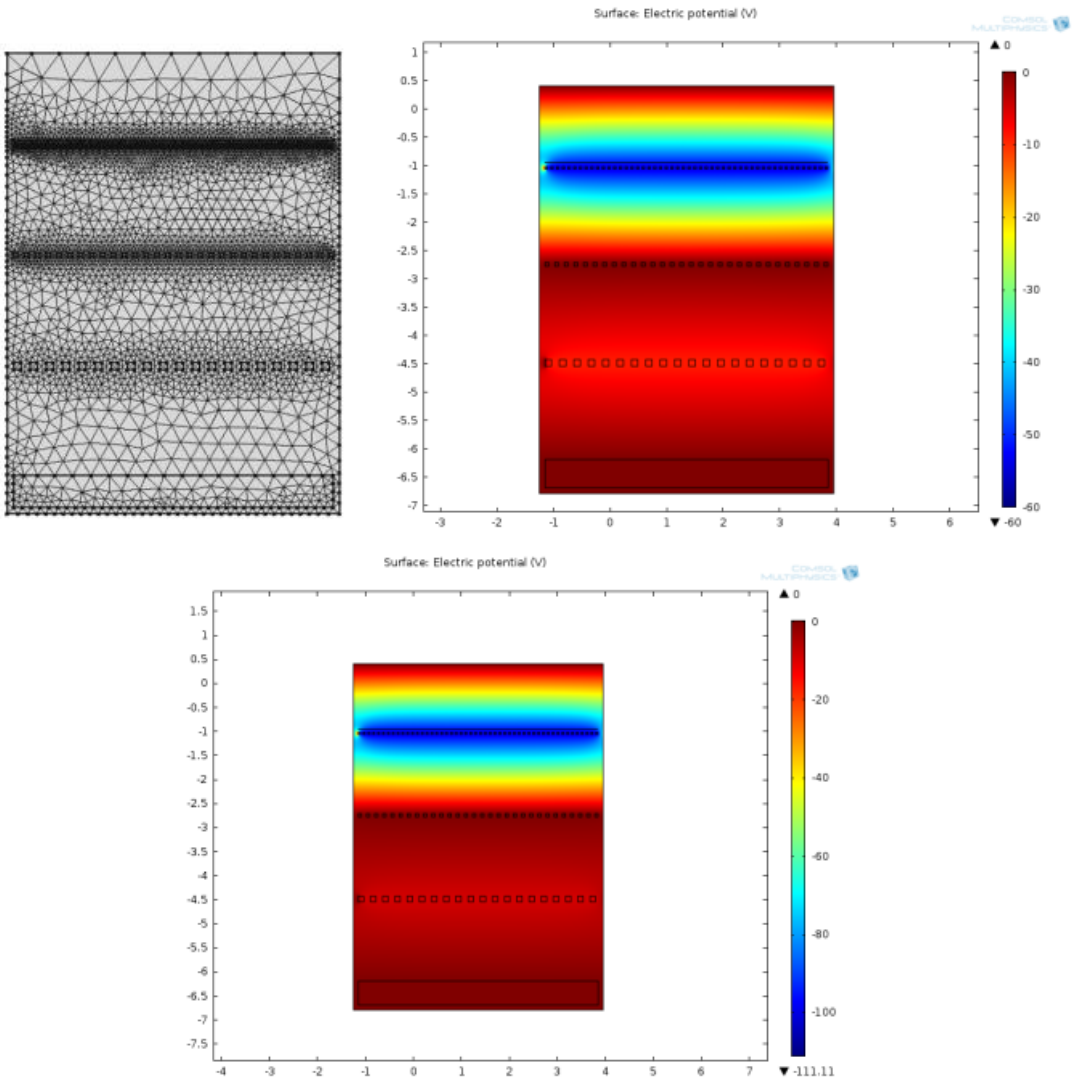

Figure 2.15: (Top Left) An image of the finite element mesh used for the field solver. (Top Right) An image of the potential field solution with an ion discriminating potential of 0 V and an electron repelling potential of -54 V. (Bottom) An image of the potential field solution with an ion discriminating potential of 0 V and an electron repelling potential of -100 V.

After the fields were solved for, the particle tracing module was initialized and particles were tracked through the established fields with a time step of 10 ns up to a total time domain 20 μs. Particle statistics, including the binning of the velocities of each particle crossing the right boundary, in the particle mesh simulation were taken in order to generate a velocity distribution function for the ions, from which the initial velocity was randomly sampled for each ion. 500 ions were initialized from an inlet boundary and all ions were released at a time of t = 0 s with random velocities associated with the velocity distribution function, defined as a normal

distribution with the values found in Fig. 2.13. As mentioned before, since the results from Section 2.3.2 are unphysical, the results from the COMSOL simulation will only prove to illustrate how the whole of the computation work will eventually provide meaningful analyzer evidence.

2.4.2 Particle Tracing Results

The COMSOL Multiphysics particle tracing module is very difficult to iterate and loop over an independent variable, so the simulation had to be iterated over the voltage applied to the second grid by calling and running the simulation multiple times using a Matlab script. For each iteration of the simulation, the number of particles interacting with the face of the collector normal to the incoming ions was counted and tallied as a virtual ion flux, which was approximated as a virtual ion current. This simulation was performed 3 times for each electron repelling potential and each collimating geometry in order to obtain statistics on the number of counts felt at the collector relative to the potential applied at the second grid. A representative solution to the particle tracing simulation can be seen in Fig. 2.16.

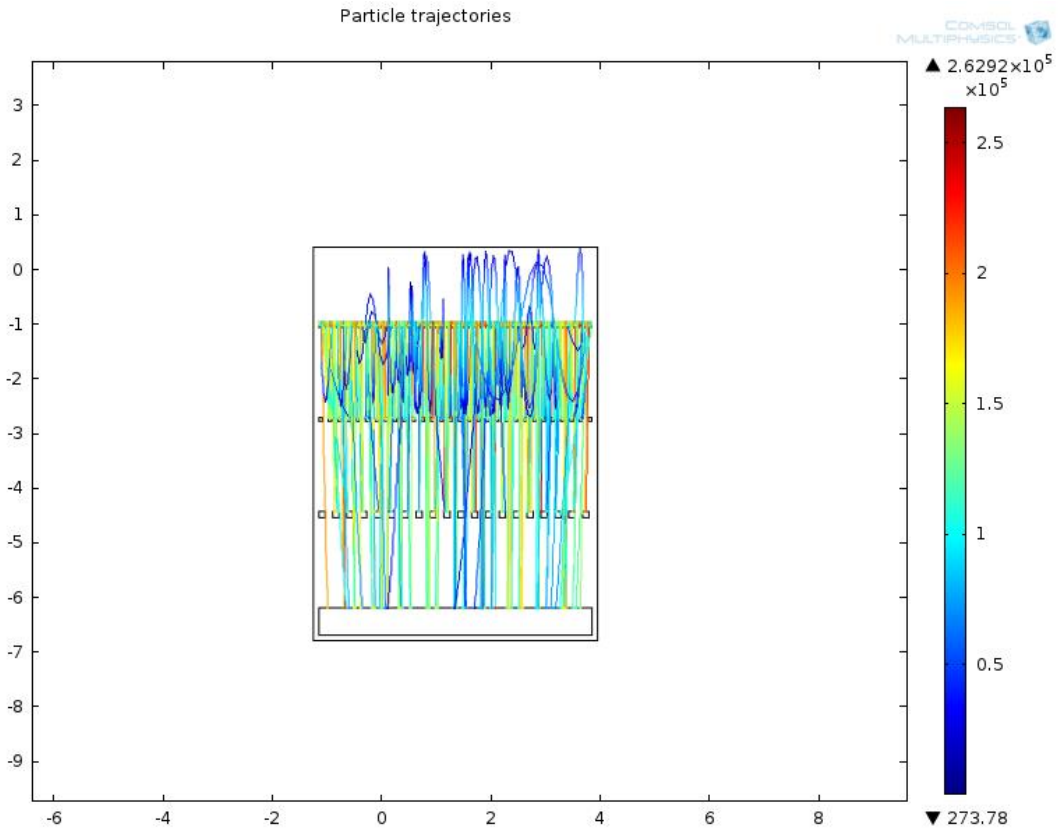

Figure 2.16: A representative solution to the particle tracing simulation where the electron repelling potential is -54 V and the ion discriminating potential is 0 V. The scale on the right indicates the magnitude of the velocities. Each line represents the track of a single particle out of the 500 that are initialized. Either particles are attracted to the electron repelling grid, are frozen when striking a surface, or are captured at the collector at the bottom.

After this simulation had been iterated over the ion discriminating potential, the counts were plotted relative to the ion discriminating potential. From these data, the counts were normalized to the maximum count value and the second-order accurate, first order derivative with respect to the ion discriminating potential was calculated. These derivative values were once again plotted relative to the ion discriminating potential and were normalized so the area under the curve was equivalent to unity. Once this procedure had been completed, the ion temperatures were found using the same procedure as will be found in Section 4.2.2. The plots of counts relative to ion discriminating voltage can be seen in Fig. 2.17. A table of the ion temperatures found for each case of electron repelling potential can be found in Table 2.1.

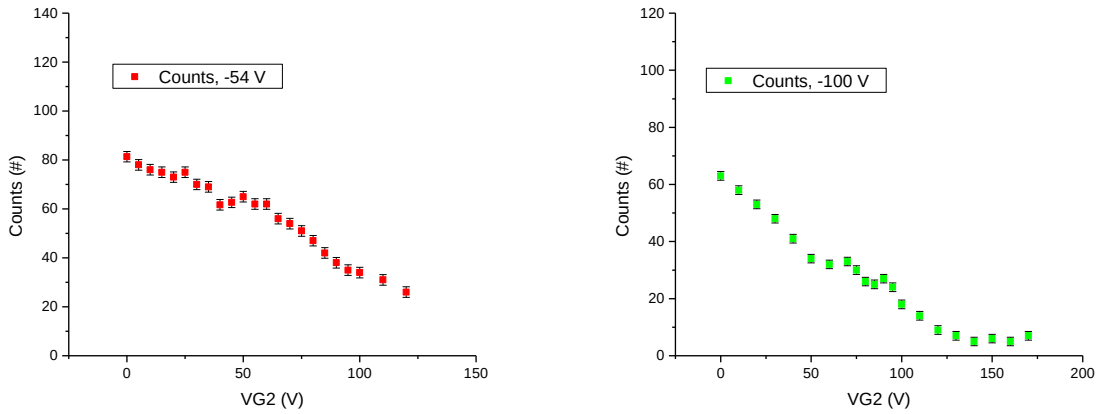

Figure 2.17: Plots of the counts relative to ion discriminating potential for an electron repelling potential of -54 V and -100 V. The x-axis VG2 represents the potential applied to the ion discriminating grid. The bottom plot is of the counts for the collimating slit simulation.

Table 2.1: Plots of the counts relative to ion discriminating potential for an electron repelling potential of -54 V and -100 V.

	Athena Output, 2.44 μs	-54 V Electron Repelling Potential	-100 V Electron Repelling Potential
Ti, eV	37.16	34.64 ± 7.01	37.10 ± 9.60

While it seems impressive that after having passed through both the collimating grid particle mesh simulation and the particle tracing simulation generated in the COMSOL Multiphysics software, the ion temperatures found by the collection of ions at the collector for both electron repelling potentials is very similar to the ion temperature from the Athena output used as the input to the particle mesh simulation, this is not the case for several reasons listed in the following paragraph. The value corresponding to the -54 V electron repelling potential is within 10% of the Athena ion temperature output value. The value corresponding to the -100 V electron repelling potential is within 1% of the Athena ion temperature output value. Both are very close to the expected value used from the output of the Athena MHD code, but the simulations done with an electron repelling potential of -100 V should be subjected to careful examination, since they should more closely mimic the experimental setup.

To conclude this chapter, while it seems that the combined hybrid simulation results provide insight into potential experimental behavior, there are still a number of complications that need to be addressed before defining the whole of this computational work as an adequate predictive model. Most of these issues deal with the kinetic particle-mesh results; however, the Athena results used both in Ref. [2] and in this report do not adequately satisfy the divergence free condition for the magnetic field and the outer radial boundary must be modified in the future to avoid this problem. The results from the kinetic particle-mesh simulations must be considered critically, since the establishment of the appropriate sheath drop is not well-defined in any of the geometries listed in Section 2.3.2. This is due to a number of underlying causes, chief among them dealing with the particle moving subroutine, the domain size, and a discrepancy found when dealing with periodicity at the boundaries. These problems allow simulated electron flux to traverse the right-hand boundary of the domain, when ideally nearly all electrons should be screened from analyzer body upon the formation of the sheath meniscus across the aperture of the collimating barrier. Beyond all these difficulties exist even more complications when considering the nature of hybrid simulations. The differences in time and spatial scales at each level are not accurately resolved to allow the whole of this computational work to be considered predictive, and must be maintained as an active area of research. As such, experimental results following similar trends to those established with the computational work in its current form must be considered coincidental.

CHAPTER 3: PROJECT OVERVIEW AND EXPERIMENTAL SETUP

3.1 Estimate of Ion Temperature and Energy Distribution

The goal of the project in determining the relevant ion information is two-fold. First, assuming a proper adherence to the assumptions and validity of a Maxwellian, albeit shifted, distribution of the ions and electrons in the TELS device, the ion temperature can be properly evaluated using appropriate probe theory. Second, the distribution as a function of time can be determined without prior assumptions, and can be used to verify the calculations of the ion temperature assuming a shifted Maxwellian distribution.

According to Hutchinson[31], the ion energy distribution can be obtained from an analyzer without prior assumption as to the shape or properties of the distribution. In a highly magnetic, collisional environment, such as is the case in TELS, as long as the collector is aligned perpendicular to the field lines to reduce the effects to a one dimensional problem, Eq. (3.1) and (3.2)[31] can be used to find the distribution relative to the voltage-current characteristic:

$$\Gamma(V_0) = \int_{-\infty}^{-\sqrt{|2eV_0/m|}} f_\infty(v_\infty) v_\infty dv_\infty \tag{3.1}$$

where Γ is the current of a single species collected per unit area as a function of the ion discriminating voltage, eV_0 is the fundamental electric charge multiplied by the ion discriminating voltage, m is the mass of the species, v_∞ is $-\sqrt{|2eV_0/m|}$, and $f_\infty(v_\infty)$ is the resulting distribution under the assumption of particle and energy conservation. The derivative of this function then gives the suitable relationship to the voltage-current characteristic:

$$\frac{d\Gamma}{dV_0} = \sqrt{\frac{2e}{m}} \frac{1}{2\sqrt{|V_0|}} f_\infty(v_\infty) v_\infty$$

$$= \frac{e}{m} f_\infty(v_\infty) \tag{3.2}$$

showing that due to the direction of flow of the charged species normal to the planar collector, the distribution is directly proportional to the first derivative of the collected current with respect to the ion discriminating voltage.

Eq. (3.1) can be modified to a more suitable form to relate the current to the voltage at each time interval during which the plasma enters the target region of interest where the analyzer sits. To do so, the species current density is modified to purely a current collection value, taking the form[44]:

$$I_C = A_{open} eZ \int_{\sqrt{|2eV_0/m|}}^{\infty} \varepsilon f_\infty(v_\infty) v_\infty dv_\infty \tag{3.3}$$

where A_{open} represents the total open area of the front collimating grid by which ions can pass through, Z is the charge on the ion species, ε is the total transmission factor seen by the ions traversing the grids to the collector, and the integrand is assumed symmetric about the boundaries. Under the assumption that the ions follow a shifted Maxwellian distribution:

$$f_\infty(v_\infty) = n\left(\frac{m}{2\pi kT}\right)^{3/2} \exp\left[-\frac{m}{2kT}(v_\infty^2 - v_s^2)\right] \tag{3.4}$$

where T is the temperature of the species in question, k is Boltzmann's constant, and v_s is the average velocity of ions in the frame of the analyzer established by the sheath potential drop, the voltage-current characteristic takes the form:

$$I_C = \begin{cases} I_0, & V_0 < V_s \\ I_0 \exp\left[-\frac{Z(V_0 - V_s)}{T_i}\right], & V_0 \geq V_s \end{cases} \tag{3.5}$$

where $I_0 = A_{open} e\varepsilon$ assuming that the transmission factor is unaffected by the incoming particle velocity, V_s is the shift potential of the mean ion velocity governed by the sheath drop, and T_i is the ion temperature. From Eq. (3.5) the ion temperature can be found as the negative inverse of the slope of the natural logarithm of the current to maximum current ratio.

The results calculated using Eq. (3.5) are only valid given that the plasma of TELS does indeed exhibit Maxwellian behavior and the flow can be described by magnetohydrodynamics (MHD). This requires that the charged species in the plasma undergo collisions on a much faster timescale than that which would allow a bulk directional, non-equilibrium flow to form. Figure 3.1 illustrates that at the operating pressure and hypothesized mean ion energy of TELS, the characteristic collision times are much less than the transit time of the ions down the length of the chamber. This transit time can also be thought of as the confinement time, which is on the order of 60 to 100 microseconds measured in previous work using optical photodiodes, while the

collision times are fractions of a microsecond to microseconds. This can and will be verified by the unadulterated calculations of the temporal evolution of the ion energy distribution function.

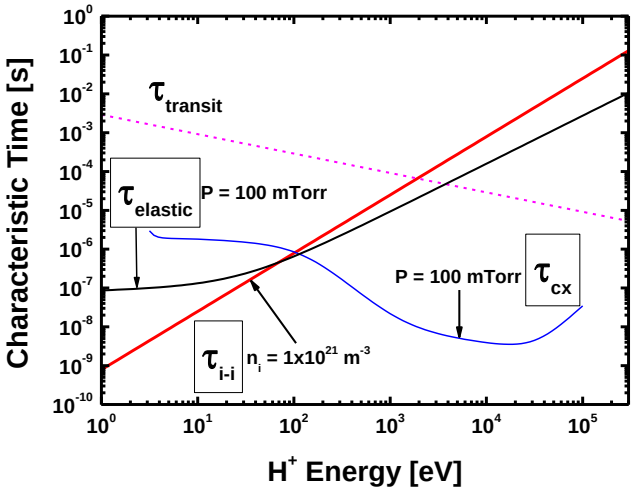

Figure 3.1: A plot depicting the characteristic collision times relative to the plasma transit time in TELS at an operating pressure of 100 mTorr and a bulk density of 1 x 10^{21} m^{-3}. TELS is hypothesized to operate at a mean ion energy ranging from 10 to 50 eV.

Another key factor in confirming the assumptions of the Maxwellian/MHD model for TELS is the ionization fraction. In previous work, this was known based on the theoretical velocity models used for a coaxial plasma accelerator relative to the experimental values[2, 58-60]. The slug model assumes the plasma moves as a single ionized body, while the snowplow model assumes that a propagating shock front carries mass and momentum axially while ionizing due to rapid heating along the front. Since the measured velocities were found to lie between the two modes and it was theoretically determined that in either case the plasma reached terminal velocity by the time it exited the plasma gun, where the propagating plasma was determined to be at or near full ionization. This lends credibility to the relative collision times previously mentioned.

A final theoretical test for the MHD assumption to be suitable comes in terms of typical plasma operating parameters and limits imposed by simple fusion plasma theory. For the MHD approximation to hold, a number of inequalities must be satisfied[61]:

$$\lambda_{De} \ll \rho_{Li} \ll L$$

$$\nu_{ei} \ll \frac{v_{Ti}}{L} \ll \omega_{ci} \ll \omega_{pe} \tag{3.6}$$

$$v_{Ti} \ll v_{Te} \ll c$$

where λ_{De} is the Debye length, ρ_{Li} is the ion Larmor radius, L is the characteristic length scale or the overall plasma radius, ν_{ei} is the electron-ion collision frequency, v_{Ti} and v_{Te} are the ion and electron thermal velocities, ω_{ci} is the ion cyclotron frequency, ω_{pe} is the electron plasma frequency, and c is the speed of light. All parameters measured assumed a pressure of 100 mTorr, an n_e of 1 x 10^{21} m^{-3}, a T_e of ~ 40 eV, and a magnetic field of 0.1 T. The characteristic length of the chamber is considered the same as the characteristic length of the plasma at a diameter of 15.24 cm. This is much greater than the ion Larmor radius at nearly 1 cm, which is in turn greater than the Debye length at nearly 5 μm. The ion thermal speed at 4.3 km/s is much smaller than the electron thermal speed 2.65 x 10^3 km/s, and both of which are much smaller than the speed of light. The frequencies also meet the same requirements, with the electron plasma frequency on the order of 2.8 x 10^{11} Hz, the ion cyclotron frequency on the order of 1.5 x 10^6 Hz, and the characteristic collision frequencies on the order of 10^4 Hz. Under this qualification, the MHD/Maxwellian approximation holds as a valid model.

3.2 TELS Device

3.2.1 TELS Capabilities and Previous Work

The Center for Plasma-Material Interactions at the University of Illinois at Urbana-Champaign currently houses a theta pinch device originally known as the Divertor Erosion and Vapor-shielding eXperiment (DEVeX), which was used to investigate the effect of lithium vapor shielding[3,62,63]. The device has since been upgraded to its current functionality for use as the TELS device[1,2], being able to now deliver 0.04 to 0.08 MJ/m^2 as compared with the previous 3 to 4 kJ/m^2 [62]. Over a pulsed plasma duration of 100 to 150 μs, the power delivered to a target ranges on the order of 0.2 to 0.8 GW/m^2. This power flux and bombardment is relevant to type 1 ELM power fluxes on a number of larger scale tokamak devices.

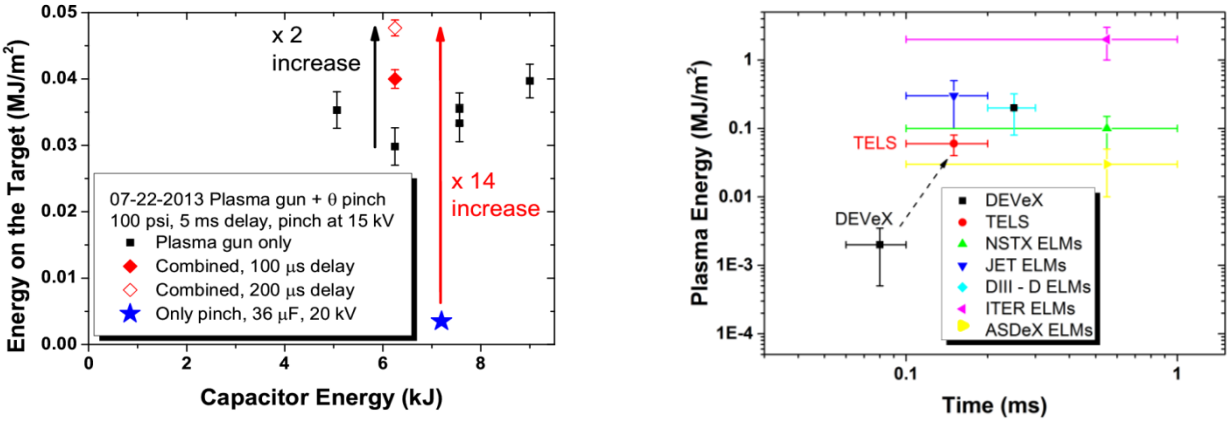

Figure 3.2: (a) A plot of the energy delivered on a target as a function of the stored energy in the 500 μF capacitor bank discharged through the coaxial plasma accelerator. The blue star represents the maximum available energy prior to the recent upgrades[62]. The black boxes represent experiments performed solely with the use of a plasma accelerator as a pre-ionization source and the red diamonds represent the energy available when utilizing the theta pinch[2]. (b) A depiction of how TELS and DEVeX energy fluxes compare to other tokamak type 1 ELMs.

The upgrades that made these new plasma energy levels possible are listed in Ref. [2]. The most important pair of improvements made to the existing device was the implementation of a puff-gas valve used in conjunction with a coaxial plasma accelerator. This pre-ionized pulse then accelerates toward a theta pinch at a high velocity, measured between 24 and 40 km/s. Another series of upgrades made to help particle transport down the length of the chamber was the application of a set of guiding magnets to prevent cross-field diffusion. The final enhancement made to the device was the use of the full 72 μF theta pinch capacitor bank in conjunction with a crowbar switch. This allows for a longer, more intense compression of the charged particles.

To understand the physics within the pinched plasma, a suite of diagnostics was used to obtain relevant plasma parameters. Previous work measured the energy flux to a target using a button-type calorimeter and the electron density and temperature using triple and double Langmuir probe diagnostics. Results from the Langmuir probe diagnostics revealed that the electron density ranges from 5×10^{20} m^{-3} to 1×10^{21} m^{-3}, while the electron temperatures ranged from 30 to 50 eV. These results are summarized in Figure 3.3.

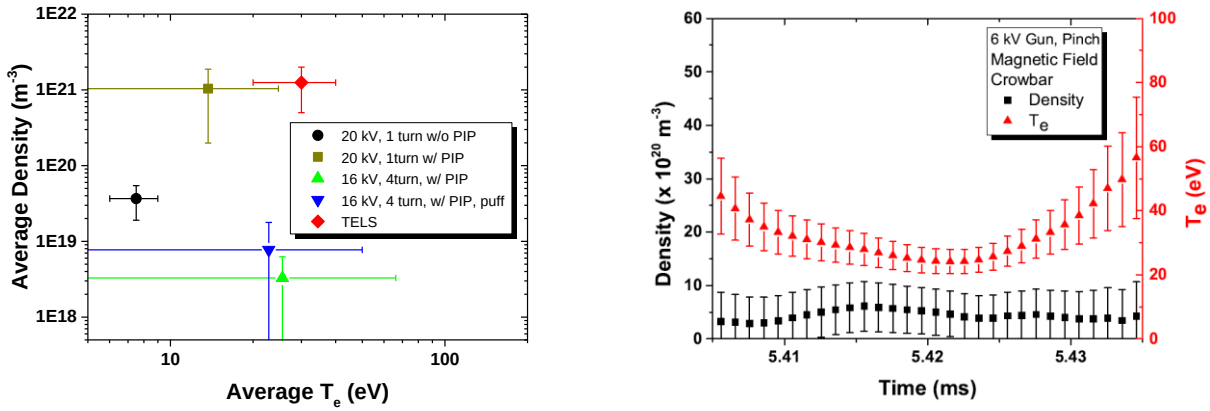

Figure 3.3: (a) A plot of the average density and temperature for a variety of configurations and upgrades to the DEVeX machine. (b) Measurements of the electron density and temperature as a function of the duration of the discharge[2].

3.2.2 TELS Setup

The current TELS setup consists of four major features that all contribute to the generation of the highly energetic, high density plasma. The primary focus of the chamber is the 1° conical set of theta coils used to magnetically confine and heat the plasma travelling axially along the chamber. The theta pinch heats the plasma in two separate manners on two separate timescales, preferentially heating the ions over the electrons due to the direct dependence on the mass of the charged particle traversing the length of the theta field[2]. The two heating methods comprise a non-adiabatic rapid implosion on the order of tens of nanoseconds to microseconds. The second heating method is through an adiabatic compression, extending from the microsecond level out to the remaining duration of the pulse[2].

The coil itself surrounds a plexiglass tube and is made of aluminum blocks segmented into four separate pieces, conically tapered to 1°. The inner diameter of the coil varies axially due to the conical shaping, but is 0.1 m on average. The depth of the coils is 0.254 m, while the axial dimension is 0.36 m. For the entirety of the analyzer experiments, the coil was segmented into 2 two-turn sections, making the inductance of the pinch 160 nH, as governed by the formula in Ref. [64]. A current is discharged through the theta coils using a 72 μF capacitor bank. The two-turn coil system requires a fast-triggering crowbar switch to reduce the overall inductance to the

coils and allow a faster current rise time[65-68]. Through the main railgap switch, a similar crowbar switch, and 15 LDF5-50 A Heliax cables running in parallel, the capacitors are discharged to a single high voltage plate which feeds into the theta coils. Each cable has a length of nearly 2 m, with an overall inductance and capacitance of 370 nH and 130 pF, respectively. For 15 cables in parallel, the total transmission inductance and capacitance are 25 nH and 2 nF[2], respectively. Both the main railgap switch and the crowbar switch are controlled by high voltage, pulsed trigger circuits capable of handling a peak current of 300 kA.

In handling the extreme loads imparted on the theta coil and supplying a steady adiabatic compression over the course of a single plasma pulse, a crowbar switch has been used in parallel with the primary railgap switch to discharge the current through the theta pinch. In the system when a lower number of turns in the coil is used, the crowbar becomes necessary to reduce the overall inductance of the switches to the transmission lines and to mitigate the issues of the slower voltage rise time in the pulse triggering circuits. The steady compression seen when operating the theta pinch with the crowbar switch allows for a higher degree of heating of the ions, since the plasma is not rapidly compressing then decompressing. This steady positive field can then couple more energy into the plasma. The importance of successful operation of the crowbar switch cannot be understated when running TELS experiments.

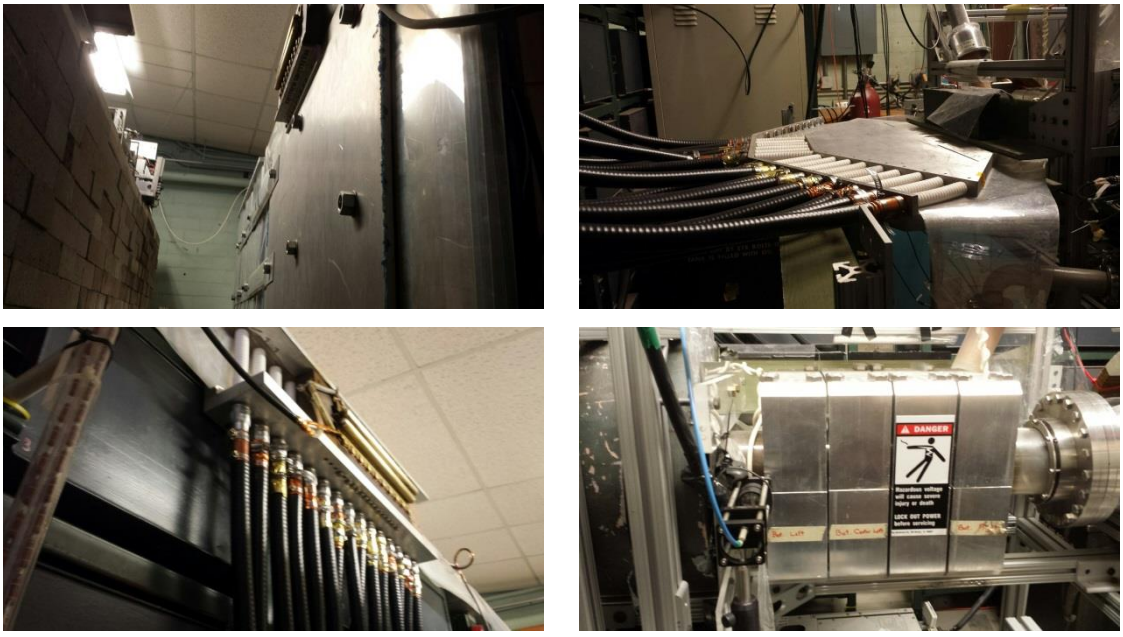

Figure 3.4: Images of the TELS theta pinch with the high voltage plate and main railgap switch (top left), the transmission lines and plate feeding the theta coils (top right), the crowbar switch and 15 transmission lines (bottom left), and the main theta coils (bottom right).

The second feature of the TELS chamber is the use of a coaxial plasma accelerator as a means of pulsed pre-ionization. The plasma accelerator used on TELS generates flow to the zeroth order through the use of a Lorentz force. The ionization from such an accelerator is much higher than other pre-ionization methods, and the plasma already has momentum by the time it reaches the theta pinch. The full theoretical explanation for the acceleration of the plasma from the coaxial plasma accelerator is given in Ref. [2], [69], and [70], where an equivalent circuit model is used in the following way:

$$(L_0 + L_1 x)\frac{d^2 I}{dt^2} + \left(R_0 + R_1 x + 2L_1 \frac{dx}{dt}\right)\frac{dI}{dt} + \cdots$$

$$+ \left(R_1 \frac{dx}{dt} + L_1 \frac{d^2 x}{dt^2} + \frac{I}{C_0}\right) = 0 \tag{3.7}$$

where the solution for the slug model , which assumes full ionization and the plasma accelerates as a bulk disk, takes the form[2, 69]:

$$\frac{d^2 x}{dt^2} = \frac{L_1}{2m} I^2 \tag{3.8}$$

and the solution for the snowplow model, which takes into account the effects of shock, viscosity and turbulence, takes the form[2, 69]:

$$\frac{d^2x}{dt^2} = \frac{\frac{1}{2}L_1 I^2 - m_1(\frac{dx}{dt})^2}{m_0 + m_1(x - x_0)} \tag{3.9}$$

where both use the following initial conditions for the full solution[2]:

$$x(t = 0) = x_0$$

$$\left.\frac{dx}{dt}\right|_{t=0} = 0 \tag{3.10}$$

$$I(t = 0) = 0$$

$$\left.\frac{dI}{dt}\right|_{t=0} = \frac{V_0}{(L_0 + L_1 x_0)}$$

According to Ref. [2], [69], and [70], in Eq. (3.7) L_0 is the total circuit inductance, L_1 is the inductive gradient of the electrode, R_0 is the total circuit resistance, R_1 is the resistive gradient of the electrode, C_0 is the capacitance in the pre-ionization capacitor bank, I is the current discharged through the electrode, and x is the mean position of the bulk plasma. Actual values corresponding to the theoretical acceleration models for the TELS plasma accelerator can be found in Ref. [2].

The accelerator uses an oxygen-free copper cathode measuring 1 inch in diameter and 12 inches in length and a stainless steel conflat 6 inch nipple with an inner diameter of approximately 6 inches as the anode. The total inductance of the capacitor setup is 0.1 μH. A 500 μF Maxwell capacitor is used as the charging source, which is fully discharged over the course of 100 to 150 μs through a T-508 L-3 Communications spark gap switch to 10 parallel RG-217 coaxial cables. The spark gap switch is operated using an in-house spark gap ignitor[2], with the distance between the electrodes adjusted to give an approximate inductance of 150 nH and can handle a discharge voltage of 5 to 6 kV at a current of 100 to 150 kA. The 10 parallel coaxial cables feed a single copper piece that connects to the external portion of a high voltage feedthrough rated for 20 kV at a peak discharge current of 150 kA. The cables are nearly a meter in length each with an inductance of 252 nH/m and a capacitance of 101 pF/m, making the total inductance of the transmission lines 25 nH and the total capacitance 1 nF.

The third feature of the TELS experiment is the puff gas valve, which in essence utilizes a pressure gradient to help drive gas and plasma flow and mitigate loss effects due to cross-field diffusion[2]. Breakdown in the plasma gun chamber requires a pressure in the range of 100 to 150 mTorr, and the pressure differential down the length of the target chamber should be established so that the target region at the time of injection has a static pressure at a base pressure of less than 5×10^{-5} Torr while the gas propagates along with the plasma. The valve used to generate this pressure differential and inject hydrogen at a supersonic gas velocity is a Parker Series 9 Pulse Valve, which injects over the duration of a 1 ms pulse.

The final feature of the TELS chamber that has helped to enhance power deposition up to Type 1 ELM levels in larger-scale tokamak devices is a set of guiding magnets used to extend the magnetic field lines from the theta pinch down to the target chamber. Theoretically, this would be useful in preventing losses from Bohm diffusion, cross-field diffusion, and the diverging fields extending from the theta pinch region. The diverging fields play a major role in enhancing radial ambipolar diffusion effects before reaching the target[2].

There are two sets of guiding magnets surrounding the target chamber. The first set that the plasma encounters as it travels toward the target region is a set of "grey" magnets. This set consists of two coils, each with 430 turns, a resistance of 0.4 Ω, and an inductance 31.8 mH. In parallel, the magnets have an overall inductance of 23.2 mH and are fed from a charge held in an 8 mF capacitor bank. The second set of coils, labeled the "copper" magnets, is composed of four copper magnets in parallel, each with 160 turns, an inductance of 8.6 mH, and a resistance of 0.5 Ω. The set is connected to a 4 mF capacitor bank. Each capacitor bank is held at a charge of 50 V, previously found to be the threshold between an inhibiting cross-field diffusion effect and too strong of a magnetic field[2], which results in a peak magnetic field of 0.03 T.

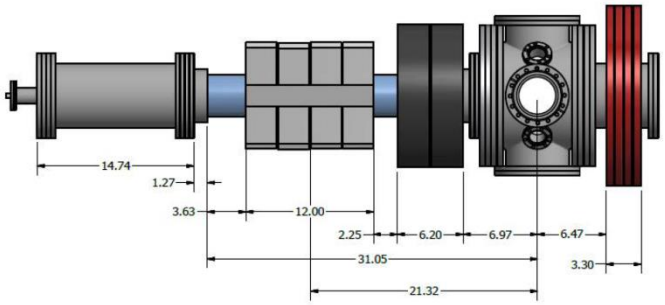

Figure 3.5: An Autodesk Inventor image of the entire TELS chamber with the appropriate axial length dimensions given in inches[2]. The coaxial gun chamber is on the left, while the target chamber sits to the right. The light gray blocks in the center are the theta pinch coils. Surrounding the target chamber are the "grey" and "copper" guiding magnets.

3.3 RFEA Setup and Operation

3.3.1 RFEA Setup

The main focus here is on the retarding field energy analyzer and the ion information extracted from TELS pulses, with the initial design being similar to that found in Ref. [46]. The analyzer was constructed carefully in order to negate the effects of plasma penetration and space charge current limitation, both of which will be discussed later. A physical depiction of the RFEA body can be seen in Fig. 3.4, which consists of a collimating stainless steel mesh, followed by three biased steel grids, and a copper plate used for current collection. The collimating mesh, used to establish a well-defined sheath potential drop, has a diameter of 19.05 mm, a thickness of 0.03 mm, and is composed of two circular pieces of 625 mesh overlaid one on top of the other to obtain an aperture size of 10 μm and a transmission factor near 10 to 15%. The three biased grids have the same diameter at 19.05 mm, but varying thicknesses and aperture sizes down the length of the analyzer. The first, electron-repelling grid has a thickness of 0.04 mm and an aperture opening size of 0.061 mm, leading to a transmission factor of 36%. The second, ion-discriminating grid has a thickness of 0.066 mm and an aperture opening size of 0.104 mm, leading a transmission factor of 38%. The final, electron-suppressing grid has a thickness of 0.114 mm and an aperture opening size of 0.14 mm, leading to a transmission factor of 30%. All transmission factors are simply taken as the ratios of open area to closed area of the mesh, with the total transmission factor to the collector plate being the product of these

individual factors is much less than 1%. The biased grids electrically connect to coaxial feed through wires using a 304 steel support structures connected to individual leads. These leads are constructed to be in line with one of the dimensions of the square mesh. The grids are isolated from each other using Macor® fabricated washers that are concentrically stamped to a depth of 1.016 mm to allow the grids to be seated within the enclosing of each washer, which has a total height of 1.651 mm and a diameter of 3.81 cm. These stamped washers, along with other Macor® fabricated flat washers, allowed the entire analyzer system to be confined to a ceramic housing structure needed to prevent extraneous current perturbations. Screw holes were drilled into each washer to allow proper alignment and the body of the analyzer was pressed using four steel 4-40 screws with appropriate nuts. From the collimating grid to the end of the final lead connecting the collector plate to a coaxial electrical feed through, the entire analyzer body measures 21.34 mm.

While the previous description of the analyzer was used on a preliminary basis, the collimating mesh using overlaid pieces of 625 stainless steel was considered to have too much error in terms of being an effective screen for electrons. The next few designs employed meshes having the correct aperture size for the Debye length limitation of DEVeX, but these meshes, originally intended for use in transmission electron microscopy, were not able to withstand the intense heat loads imparted by repetitive TELS discharges. The final design settled on a collimating slit that was purchased from Lenox Laser and used a 0.025 mm thick tungsten disk with a 5 μm x 3 mm slit cut out of the center as the collimating barrier. As a refractory metal, the tungsten would be able to handle the heat loads imparted without disintegrating and the slit is of the appropriate dimension to establish the necessary sheath potential drop. The transparency of this individual slit is much less than 1%, which would lead to an overall transparency factor for the new analyzer system to be on the order of 2×10^{-4} %.

Two analyzers were used in the final configuration, with one analyzer open to the incoming plasma flow and the other having a Teflon to block the incoming flux. Both analyzers were mounted so the collector plate was normal to the incoming particle flux, and, as will be mentioned in Section 3.3.2, the closed analyzer is used as a control against electromagnetic interference and displacement current. The importance of the control analyzer will be explained in detail in a later section, but it cannot be stressed enough how important this design was to

obtaining valuable results. The total configuration was mounted on a linear motion feedthrough using an aluminum oxide tube, with a secondary 430 ferritic stainless steel housing unit surrounding the entire arrangement to prevent electromagnetic perturbations.

Since TELS plasmas are highly transient events with pulse times on the order of 150 μs or less, generating a sweeping function for the ion discriminating grid that is not susceptible to plasma current perturbations and is nearly uninhibited by typical RC or LC time delays is not feasible. Not only that, but relevant information would require collection times and sweeping times to be on the order of 10s to 100s of nanoseconds. For these reasons, the collection of a characteristic current-voltage waveform from the RFEA collector required measurement on a shot-to-shot basis. For each experiment, the biased grids were held at constant DC voltages, with the electron-repelling and electron-suppressing grids biased using banks of 9V batteries and the ion-discriminating grid biased with a single power supply outfitted with electrolytic capacitors to handle the load imparted by the plasma. The initial electron-repelling grid was held at -105 V DC using eleven 9V batteries connected in series. This potential was chosen in accordance with the electron temperature values seen in Fig. 3.3, since this voltage will sweep out a significant number of the electrons that are not repelled by the sheath established at the collimating grid. The ion-discriminating grid was varied between 0 and 130 V DC using a KEPCO ATE 150-3.5M DC power supply, with five BHC Aerovox 330 μF capacitors connected to each other in parallel and connected to the output of the power supply. The final electron-suppressing grid, used to prevent secondary emission backflow, was held at -9.4 V DC using a single 9V battery. The initial collimating mesh was left to float, while the collector cup was held at power ground. Power provided to the ion discriminating grid was in reference to power ground. Proper grounding was a vital issue in the experiment, since pulsed devices are often plagued by ground loops or chambers that temporarily float above ground, which impedes proper diagnostic work. All potentials were delivered and maintained using RG-58 coaxial cables from a separate isolated Faraday cage control room to the BNC feed throughs. Currents for each analyzer were collected and monitored on an Agilent Infiniium oscilloscope using two Tektronix P5200 High Voltage Differential Probes measured across separate 10 kΩ resistors. The equivalent circuit layout for the analyzers can be seen alongside the physical depiction in Fig. 3.6.

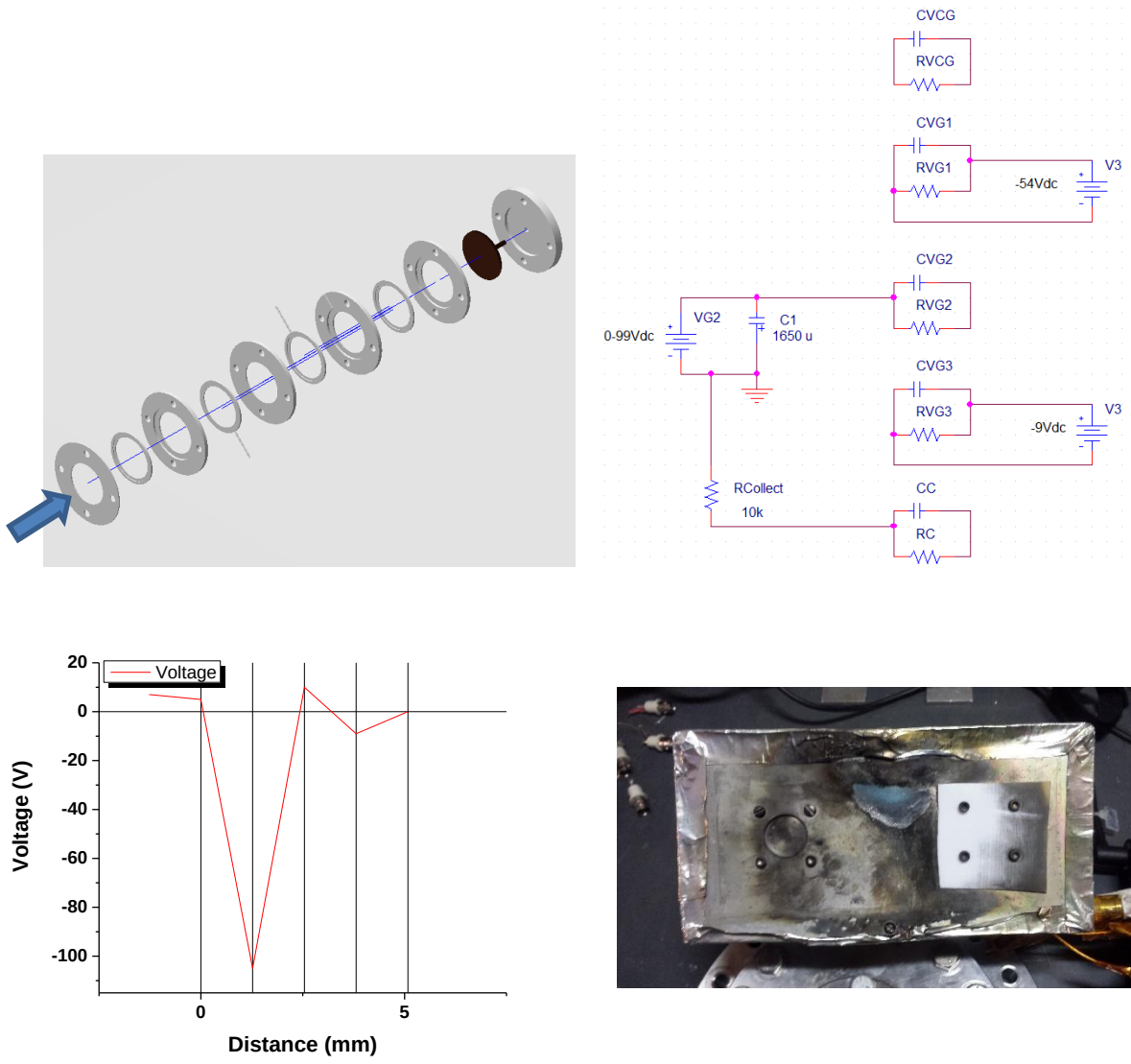

Figure 3.6: (Top left) An exploded CAD image of the analyzer body with the direction of plasma flow indicated. (Top right) An equivalent circuit diagram of the analyzer setup. The P5200 High Voltage Differential probe measures across the 10 kΩ resistor, integrates the signal, and feeds the signal into the Agilent Infiniium oscilloscope. The mesh, grids, and collector are represented schematically by their equivalent resistance and capacitance. (Bottom left) An image of the grid bias potentials. The positive bias located at the ion discriminating grid is varied on a shot-to-shot basis to get an I-V sweep. (Bottom right) A picture of the full analyzer configuration. This picture was taken after a full shot campaign had finished and the analyzer was removed from the chamber. The front plate of the 430 stainless steel box appears to have undergone some thermal deformation after having been subjected to nearly 100 TELS pulses.

3.3.2 Mitigating Electromagnetic Effects

TELS, not unlike other similar pulsed devices, requires magnetic fields in order to implode, compress, and transport the plasma from the theta pinch region to the target region.

Without the guiding fields, the fringe fields at the edge of the diverging theta pinch magnetic field in the target chamber are only as high as approximately 100 Gauss. With the guiding fields, the fields in the target region may reach up to 300 Gauss, but are limited by the previously mentioned competing processes[2]. Even with these effective field strengths, there is still the possibility to generate strong electromagnetic noise on very rapid timescales in both the transmission and collections lines to and from a single retarding field energy analyzer. It is for this reason, apart from trying to discern noise generated due to ground loop issues, that the need for a second, "control" analyzer arose.

Two effects from electromagnetic effects are the cause for noise being observed in both the collection and transmission lines. Both of these effects are due to the very small timescales on which the TELS plasma exists and imparts energy, and both can easily be summarized using Maxwell's equations. The first effect can be easily deduced from Faraday's law of induction, otherwise known as the Maxwell-Faraday equation:

$$\nabla \times \boldsymbol{E} = -\frac{\partial \boldsymbol{B}}{\partial t} \tag{3.11}$$

where **E** is the electric field and **B** is the magnetic field. In the case of TELS, the circuit closed by the connection of each grid with either ground or the negative terminal of a battery bank is subjected to a time-varying magnetic field that propagates axially down the length of the chamber. Approximating that the rate of change of the magnetic field without the guiding fields is 100 Gauss or so over the pulse duration of 150 μs, the magnitude of the curl of the electric field is approximately 66.67 V m^{-2}. The induced electromotive force on a piece of wire measuring 0.2 mm in diameter and 0.457 m in length is approximately 2 x 10^{-2} V, resulting in an overall induced current of nearly 90 mA. While this should not substantially perturb the biased grids or their respective supplies, this could potentially be a substantial contributor to the collection signal. Going through the same set of calculations, with the primary changing magnetic field provided by the guiding field with a 15 ms quarter-cycle time, the induced current is closer to 3 mA, which, while still substantial, is less problematic than with the rapidly alternating field provided by the theta pinch alone.

The second electromagnetic effect that perturbs the currents of the transmission and collection lines in the analyzer is due to the rapid timescales associated with displacement currents in Maxwell's relation that describes the curl of the magnetic field:

$$\nabla \times \boldsymbol{B} = \mu_0 (\boldsymbol{J} + \varepsilon_0 \frac{\partial \boldsymbol{E}}{\partial t}) \tag{3.12}$$

where μ_0 is the vacuum permeability, ε_0 is the vacuum permittivity, and **J** is the free current density. In steady-state and even semi-transient events, with timescales much greater than those witnessed in TELS, the displacement current governed by the time-varying electric field is often ignored due to its negligible contribution to the curl of the magnetic field, and vice versa. In the case of TELS, however, not only do the effects of a highly transient magnetic field induce currents that can perturb transmission and collection in the analyzer, but these effects must be coupled with the highly transient nature of the electric field as well. It is much more of a challenge to approximate perturbations, even to the zeroth order, of the time-varying electric field in the TELS device because the nature of the pulse itself is oscillatory, both at the fundamental and harmonic frequencies. Assuming that the full pulse discharges all of the energy held in the coaxial accelerator capacitors and the radial distance is the proper effective dimension, then the approximate electric field is 8.7×10^4 V m^{-1}, assuming of course that there was no major contribution from the theta pinch. At a time scale of 150 μs, the time-varying field calculates out to be 5.7×10^8 V m^{-1} s^{-1}, which can then translate to an induced current density of 5.1×10^{-3} A m^{-2}. Assuming the same dimensions of wire as in the previous paragraph, this would translate to a current of approximately 1.5 μA. This means that the effects of induction are much more serious than the effects of displacement current, and must be properly accounted for.

For these reasons, and for issues pertaining to proper grounding and isolation, a control analyzer was introduced to the collection configuration. This analyzer is shielded from the incoming plasma using a 430 ferritic stainless steel front plate that has no inlet. To fully take into effect the displacement current, the front shield would not be conducting, but instead a ceramic insulating piece. The effects of displacement current relative to induced current, however, have been calculated to be much less serious in terms of current collection. The effects from the electromagnetic noise and circuit noise can then be subtracted out directly from the collector signal open to the plasma. Other solution methods included using coaxial transmission and

collection cables to help reduce induced effects, but the sum total of these solution methods helped to generate meaningful ion information.

3.3.3 Space Charge Limiting Current

In 1945, Brillouin introduced the world to the exact criterion by which a space charge effect can stagnate flow in electron beams and generate a secondary potential hill that supersedes the potential distribution set by the difference in voltage between two charged plates[71]. This theory can be carried to the analyses of charged species distributions using gridded-type analyzers due in large part to the fact that the measured species ultimately form a beam within the analyzer after the oppositely charged species is swept from the analyzer control volume. Apart from this primary physical phenomenon, the grids act as planar boundaries dictating the potential difference felt by the measured species. For an optimal magnetic field, Brillouin calculated the maximum possible current in the beam when the potential between the grids is given and an optimal magnetic field configuration is accounted for[71]:

$$I_{max} = -\frac{\epsilon_0}{\alpha\beta}\left(\frac{-e}{m}\right)^{1/2}\left(\frac{2}{3}\varphi\right)^{3/2} \tag{3.13}$$

where ε_0 is the vacuum permittivity, $\alpha\beta$ is a product of two geometrical factors (planar geometry for this case, $\alpha = 4b^2$ and $\beta = \frac{1}{16}b$), the electrodes are located at ± b, e is the fundamental charge, m is the mass of the charged species, and φ is the potential between planes. This arises due to the fact that the whole beam moves with a constant drift velocity along the direction between the planes, and generates a constant space charge density, ρ:

$$\rho = 4\epsilon_0\omega_H^2\left(\frac{m}{e}\right) \tag{3.14}$$

where ω_H is a measure of the magnetic field (the cyclotron frequency, ω_c, in our case), showing that the beam can be effectively modified by the effect of the magnetic field.

Due to the high densities and fluxes incident on targets in the TELS device, one of the greatest challenges to properly determining the ion information comes in the form of the space-charge limiting current. Because the electrons are sufficiently repelled by the charge on the first

grid, an ion beam is formed and establishes a new potential arrangement, which, with a high enough energy density, has the ability to overcome the electrostatic fields generated at the grids. This negates any collected ion information, since the potential structure within the analyzer is no longer well-known. The maximum allowable current density governed by this phenomenon is given by, which is a direct modification of Eq. (3.13) after having applied the proper geometrical and magnetic field factors[72]:

$$j_{sc,crit} \approx 3.85 \times 10^{-8}[(qV_{G3} + E_{\|})^{3/2}/(z - z_m)^2][1$$

$$+0.0247T_i^{1/2}(qV_{G3} + E_{\|})^{-1/2}] \quad (3.15)$$

where $j_{sc,crit}$ is in A/cm^2, V_{G3} (the voltage applied to the electron suppressor grid) is in V, $E_{\|}$ is the average ion energy in eV ($E_{\|} \cong T_i + qV_{sheath}$), T_i is the measured ion temperature in eV, q is charge on the ion, and $z\text{-}z_m$ is the minimum distance between the potentials established between the electron suppressing grid and the collector cup. With a V_{G3} of -9 V, a $z\text{-}z_m$ of 1.016 mm, an $E_{\|}$ ranging from 87 to 103 eV, and a measured ion temperature of nearly 20 to 30 eV, the critical space charge limiting current ranges from 2.60 to 3.43 mA cm^{-2}. With peak currents collected ranging from 1.6 to 2.2 mA and assuming that the beam expands to the diameter of the collector, the maximum collected current density ranges from 410 to 570 μA cm^{-2}. The assumption of beam expansion in this case is valid, since even at a field of 200 Gauss, the ion Larmour radius is on the order of 0.5 to 1 cm. The analyzer, therefore, is not limited by the space charge effect.

CHAPTER 4: RESULTS AND DISCUSSION

4.1 Preliminary Results and Analysis

4.1.1 Measurements from a DC Magnetron Source

To experimentally benchmark the validity of the analyzers as an ion analysis tool prior to subjecting them to the transient plasma of TELS, a single analyzer was placed in a chamber where ions from a direct current (DC) magnetron sputtering source were measured. The reason for using a DC magnetron source is that it is common knowledge that this kind of source produces a cold plasma, where the mean ion energy is at a thermalized energy of 0.025 eV. The analysis using the Maxwellian probe theory to deduce the ion temperature, as in Eq. (3.5), does not hold for this kind of plasma since collisions do not equilibrate the ion and electron temperatures, but the ion energy distribution of such a plasma can still be determined using the same theory of operation as described in Ch. 3. This is because the measurement of the distribution is not based on the assumption of an already pre-defined distribution, and can easily be extracted from the current-voltage relationship as seen in Eq. (3.2). By extracting from the distribution both the most probable and mean ion energy value, the analysis can be validated if these energies lie within reason of the energy previously described.

The Sputtering High-purity Atomic Deposition Experiment, or SHADE[73 - 74], chamber in the Center for Plasma-Material Interactions at the University of Illinois at Urbana-Champaign was used as the primary tool for experimentally benchmarking the efficacy of the analyzers. This chamber employs the use of a 4-inch magnetron sputtering source that can be outfitted with a variety of magnet packs, target materials, and power supplies. SHADE is primarily used for the analysis and optimization of sputtering rates and magnet packs using the High Power Impulse Magnetron Sputtering, HiPIMS[75 - 78], system. The results found for the benchmarking of the analyzers were taken using a conventional magnet pack, with the magnetic “racetrack” being made of a single concentric polarized ring surrounding a circle at the center of opposite polarity. The power supplied to this magnetron used a direct current (DC) source provided by an Advanced Energy Pinnacle Plus DC power supply. To prevent target melting, cooling lines,

using water as the cooling medium, were run through the back of the pack. The target was a pre-fabricated titanium, Ti, target manufactured by Kurt J. Lesker. The gas used was argon, Ar, and the operating pressure was varied by concise control on the inlet gas using a mass flow controller, MFC, balanced carefully by the partial evacuation of the chamber using a Varian Model 9698518 turbomolecular pump and an Oerlikon Leybold Vacuum turbomolecular pump. A physical image and a schematic of the SHADE chamber can be seen in Figure 3.1. The analyzer was held at a constant distance of approximately 1.5 inches away from the target of the magnetron head.

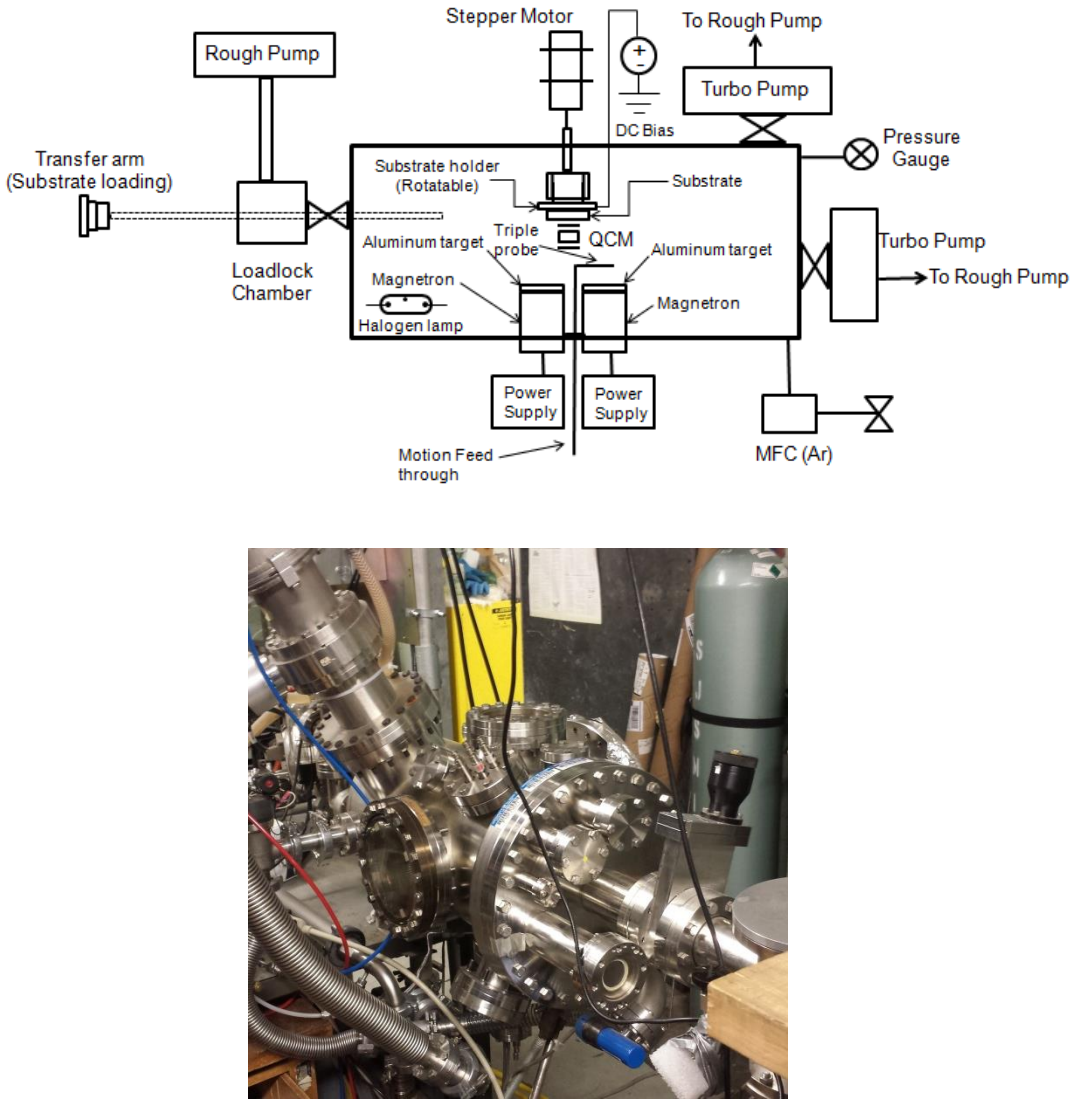

Figure 4.1: (Top) A rough schematic of the SHADE experiment[73]. The analyzer was placed where the "Triple probe" is indicated in the diagram. (Bottom) An image of the actual SHADE experiment. The magnetron heads come in from a 12" conflat flange located opposite the 8" window seen to the left.

The analyzer operation in these experiments was different to the operation method used when subjecting the system to the TELS plasma to help compensate for the physics of the cold plasma environment. The front grid was held at the floating potential of the plasma, since the plasma potential is not likely to oscillate at a high frequency as is the case in a TELS transient event. The electron suppressing grid was not used for these experiments because even with the acceleration of the ions caused by the potential drop in the sheath and the potential applied to the electron repelling grid, it was considered unlikely that a substantial number of secondary electrons would be emitted from the collector cup. This also helps to increase the overall transmission to the collector since ions are not being drawn to the negative potential applied at the suppressor grid. The electron repelling grid was held at a constant value of -18 Vdc using two 9 V batteries connected in series. The ion discriminating grid was swept between -15 Vdc and 50 Vdc using a BK Precision 4011A F MHz Function Generator amplified through a KEPCO Model BOP 500M Bipolar Operational Power Supply/Amplifier. Collected signals were read on an Agilent InfiniVision DBO-X 3034A oscilloscope, fed from the analog output of a Keithley 485 Autoranging Picoammeter which was used for the direct measurement of the ion current. Proper attenuation was accounted for since the picoammeter output was amplified by 10000:1.

Raw current and voltage waveforms were collected for a variety of operational parameters. The chamber pressures were varied between 1, 2, 5, and 10 mTorr and the powers were varied between 200, 300, and 400 W for each pressure. A set of data, taken at a power of 300 W and 2 mTorr, representative of the data taken for all powers and pressures below 5 mTorr can be seen in Figure 4.2. These data represent normal operation of the energy analyzer within the SHADE chamber subjected to a low-power, low-pressure Ar plasma.

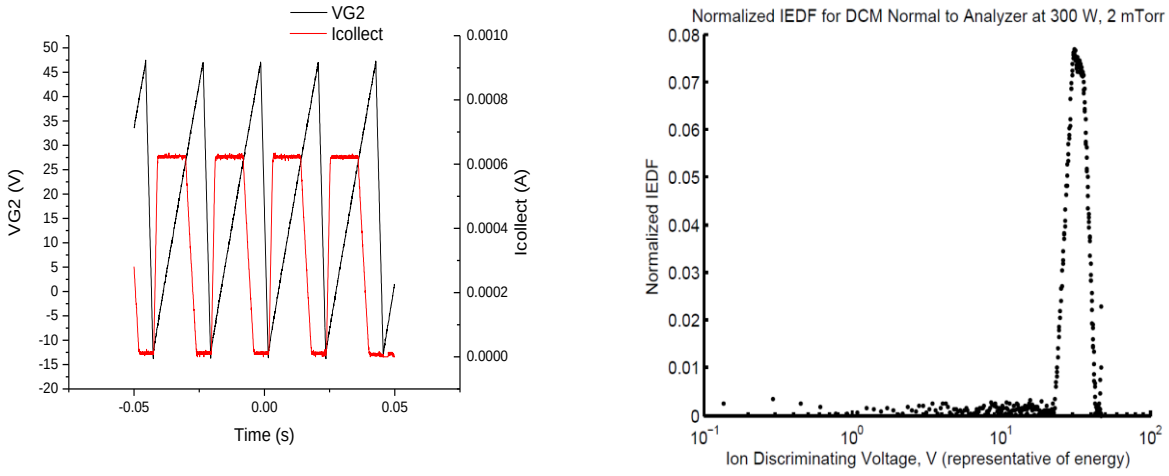

Figure 4.2: (Left) The sweeping potential on the ion discriminating grid (left y-axis) and the collected ion current (right y-axis) as a function of time. (Right) The resulting energy distribution found using Eq. (2.2) by modifying the left plot to give an I-V trace.

Obvious from the plot on the right, the distribution is shifted to where a most probable energy at the peak is given by an ion energy of approximately 27 eV. This is an entirely logical and realistic shift in the distribution due to the acceleration felt by the ions when traversing the analyzer geometry. Coming into contact with the front of the analyzer, the plasma is subjected to the sheath potential drop, which will vary based on the power applied to the magnetron, and, thus, to the plasma. At this point, a significant portion of the electrons are swept from the grid since the average energy of the electron population distribution is near 2 eV, but the ions are accelerated due to this potential difference. After screening out the majority of the distribution of electrons in the sheath potential drop, both charged species (assuming only singly charged Ar ions) are then subjected to the potential established by the electron repelling grid held at -18 V. This potential is large enough to sweep out nearly all of the remaining high energy electrons, thus establishing an ion beam which is also accelerated by the potential at this grid even though this also reduces the transmittance at the repelling grid. Due to these two different accelerations on the ions, the distribution should be shifted in energy equivalent to the sum of these two potentials, which is 27 to 28 V in this case of the analyzer within SHADE. These full values of the most probable energies for the ions can be seen in Fig. 4.3, where no subtraction of the 27 V drop has occurred, since the sheath potential drop varies with power.

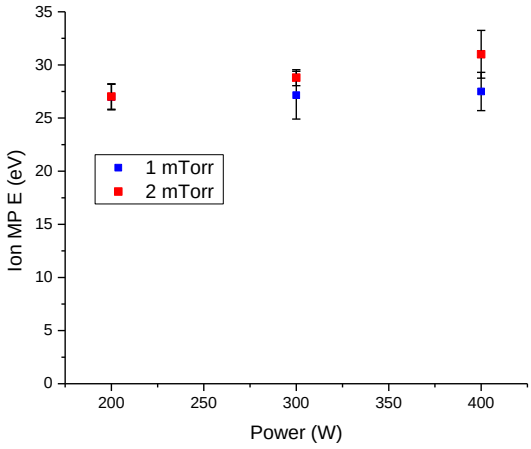

Figure 4.3: A plot illustrating the most probable ion energy as a function of both pressure and power using the SHADE DC magnetron source. Error bars are associated with the standard error propagated through from the current measurements.

The plot showing the most probable ion energies above seems to indicate that at higher pressures and powers, there is a slight increase in the most probable energy for ions. This makes sense for the trend associated with power supplied to the magnetron since higher powers indicate a higher potential drop across the sheath, due in large part to the increased electron temperature. Since the ion temperature in a low-temperature source is known, subtracting the acceleration felt by the ions from the electron repelling grid from the plot above indicates the sheath potential drop. The increase in pressure, however, should be affecting inversely affecting the electron temperature. Since the error bars associated with the measured values are within range of each other, it could be safe to assume that the error in the measurement of the most probable energy value is only different between the two pressures due to measurement and calculation error, and actually these values are closer than indicated in Fig. 4.3.

An increase in the most probable energy at higher pressures is unexpected. With the gas as Ar, the pressure of 2 mTorr may be starting to reach the limit of normal analyzer operation, where the dimensions suited to hydrogen and TELS break down in the presence of a DC plasma. From this plot, it can be concluded that the data corresponding to 200 W in both cases is most correct, and the data corresponding to an operation pressure of 1 mTorr is more correct than the data corresponding to an operating pressure of 2 mTorr.

Abnormal analyzer operation was witnessed when the pressure was set at higher values, corresponding to 5 mTorr and 10 mTorr in the case of the SHADE DC magnetron sputtering source. This can be seen in Figure 4.4, where the raw current voltage trace indicates a shift in the characteristic current decay felt at the collector cup to a much smaller potential value. This would be the case at higher pressures, anyway, since the electron temperature which governs the sheath potential drop would decrease significantly from high collisionality. This, however, does not adequately explain the fact that after having subtracted out the 18 V acceleration applied to the ions by the electron repelling grid, the sheath potential drop would then end up negative. A very plausible explanation for this is since these abnormalities are observed at higher pressures, the smaller mean free paths require smaller distances between the grids to prevent secondary discharge within the analyzer. In effect, the generation of a secondary discharge within the analyzer body most likely contributes to this shift, where the collector is sampling ions from a different plasma altogether from the plasma body being measured. Space charge is most likely not the culprit in terms of generating these abnormalities for two reasons. First, abnormal operation is a function of pressure, lending credence to the limitations brought on by the mean free path. Second, the potential barrier caused by space charge effects would actually more likely shift or skew the distribution in the opposite direction, since only higher energy ions would be able to traverse the space charge barrier. While this limits operation in a steady-state plasma to a lower pressure regime using Ar as the primary ionized medium and a metallic target, the analyzer was manufactured to be able to handle a hydrogen density up to 1×10^{22} m^{-3} by carefully limiting the distance between the first collimating grid and the ion discriminating grid to be less than the smallest effective mean free path. This prevents any ionization event from occurring within the analyzer body. A set of data, taken at a power of 400 W and 10 mTorr, representative of the data taken for all powers and pressures above 5 mTorr, can be seen in Figure 4.4. These data represent abnormal operation of the energy analyzer within the SHADE chamber subjected to a low-power, low-pressure Ar plasma.

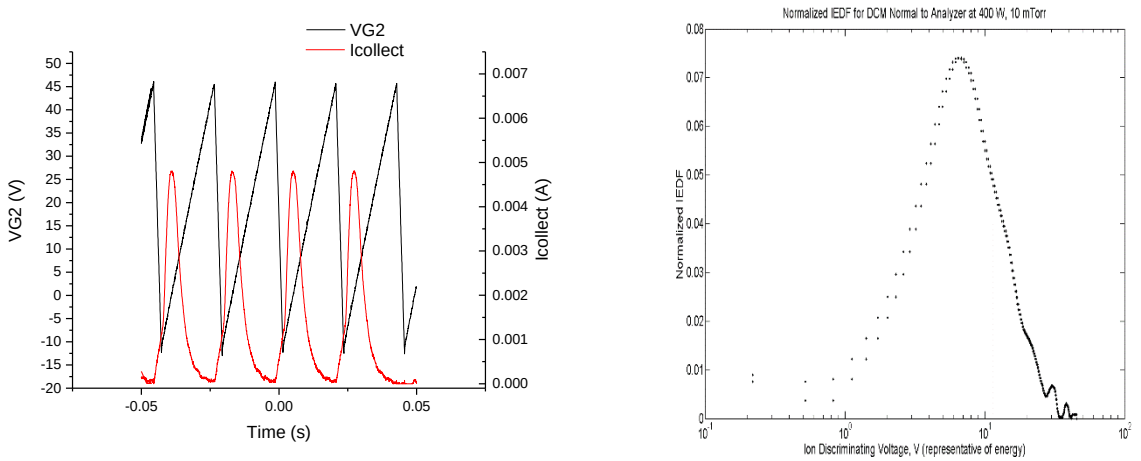

Figure 4.4: (Left) The sweeping potential on the ion discriminating grid (left y-axis) and the collected ion current (right y-axis) as a function of time. (Right) The resulting energy distribution found using Eq. (2.2) by modifying the left plot to give an I-V trace. These data were taken for abnormal operation.

4.2 TELS Results

4.2.1 Time-resolved Distribution Functions

The most important results taken in these experiments to find the ion information in TELS were those that pertained to the ion energy distribution functions. These distributions tell a great deal about the highly transient TELS plasma, as well as the interactions the plasma has with target materials, such as lithium. The distributions also indicate the level to which TELS is able to adequately simulate an ELM strike. Distributions were extracted as both a function of discharge time and the potential applied to the ion discriminating grid, indicating how the ion information changes over the duration of the pulse. Initially, analyzers using floating collimating meshes were used, but these collimators were found to be insufficient and were replaced with the collimating slit described in Ch. 3. All results here were found using the collimating slit.

Two different shot conditions were sampled using the analyzer configuration. The first condition utilized the combination of the coaxial plasma accelerator and the theta pinch, with the analyzer at the position in the target chamber where the peak heat flux would strike the divertor material or LiMIT module, at approximately 0.61 m downstream of the theta pinch. This position was chosen for obvious reasons, since the behavior of the plasma at this position would determine the plasma-facing and plasma-material interaction properties. At this distance away

from the theta pinch, and without the use of the guiding field to help extend the flux surfaces, the fringing magnetic field is only 0.01 T in the axial direction with a much smaller magnetic component in the radial direction. It is for this reason that the previous assumption of the ion Larmour radius extending to the size of the collector used to determine the limitation of space charge remains valid. A plot of the currents of the PiP and the theta pinch over time, indicative of the pulse parameters for each shot, can be seen in Fig. 4.5.

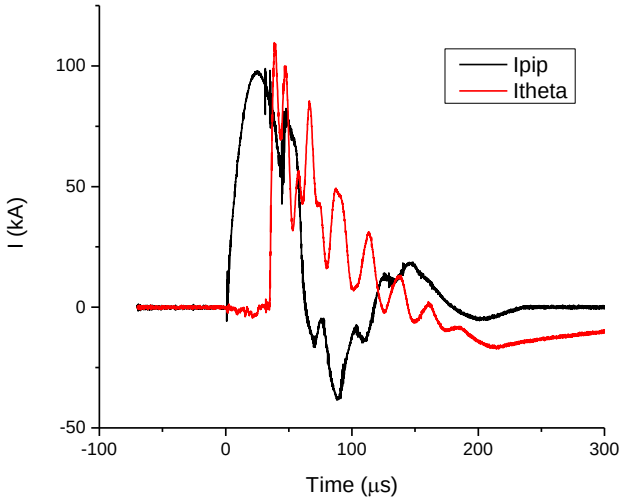

Figure 4.5: Representative plots of the current traces for the coaxial plasma thruster (PiP) and the theta pinch over discharge time in microseconds. This indicates that the initialization of the pulse is when the PiP fires.

To illustrate how one arrives at the proper distribution function with respect to time, the procedure by which the raw data must be converted requires explanation. Pivotal to the analysis is the fact that the current trace of the closed analyzer must be subtracted from the current trace of the open analyzer in order to get rid of the noise generated by electromagnetic and grounding issues. Two representative traces with respect to time can be seen in Fig. 4.6, where the black trace represents that of the open analyzer and the red trace represents that of the closed analyzer. The resultant current trace can also be seen in Fig. 4.6.

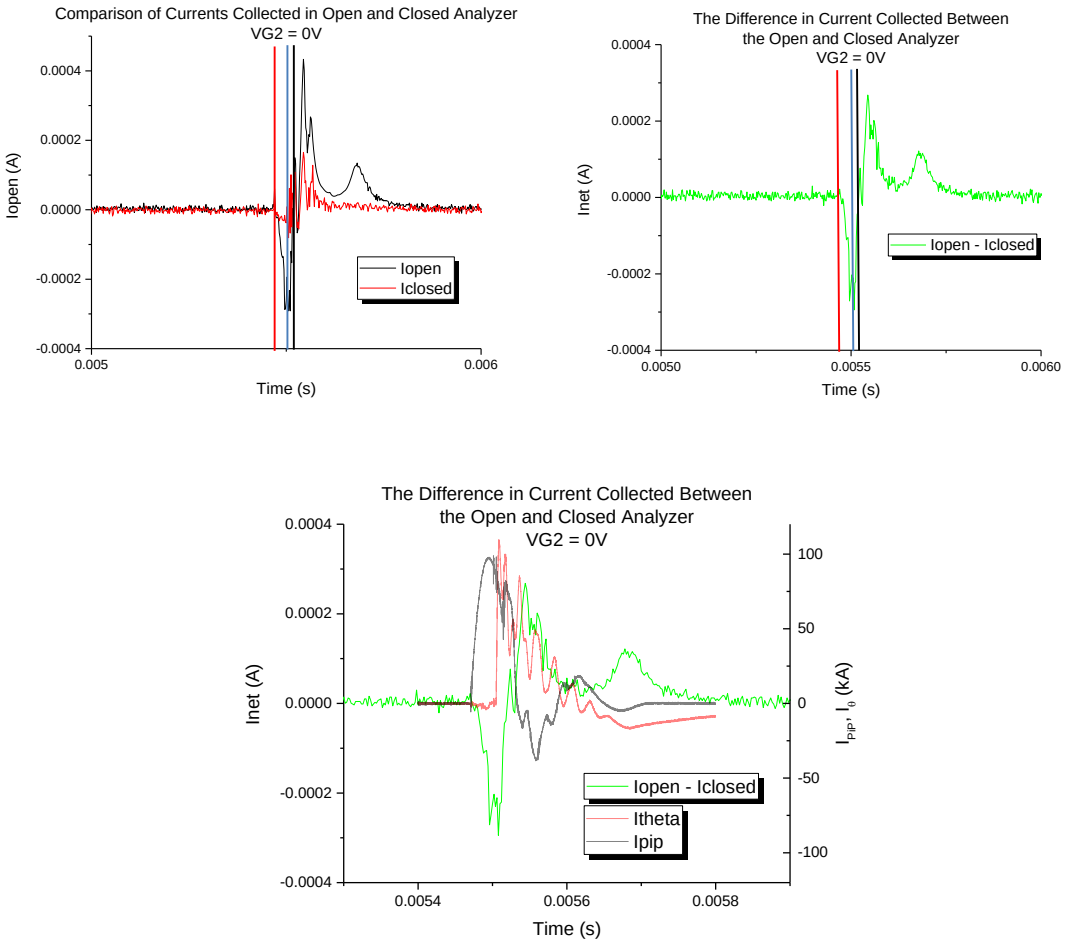

Figure 4.6: (Left) The comparison of currents collected between the open and closed analyzers at a discriminating potential of 0V. These traces are representative of the current collected for each analyzer at each discriminating potential. (Right) The resultant current waveform from the subtraction of the closed current trace from the open current trace. The red vertical lines indicate where the PiP fires and the blue vertical lines indicate where the theta pinch fires. (Bottom) A plot indicated the current trends of the PiP and θ pinch relative to the trends in the net collected current. From the velocity data in Ref. [2] it is known that the plasma does not arrive at the target until the time indicated by the black vertical lines, meaning that the negative signal seen before these indicated times are most likely due to high energy electrons arriving in the target chamber before the bulk plasma.

The final current for each value of the ion discriminating grid, similar to the image to the right in Fig. 4.6, were then compared to one another. As mentioned in the section describing the analyzer measurements in a DC chamber, the shifted potential corresponding to a similar shift in the distribution function takes the acceleration to the ions applied by the electron repelling grid into account. In all experimental cases, the electron repelling grid was held at -105 Vdc, meaning that at minimum the ions are accelerated to an energy corresponding to nearly 100 eV after

having traversed the collimating mesh. The remaining shift in the energy distribution is provided by the difference between the sheath drop felt at the collimator and the potential at which the collector is held. This is easily illustrated when comparing the currents over time and observing how the magnitude of the current decreases with increasing discriminating potential. A plot of the currents over time can be seen in Fig. 4.7, where the initial negative part of the pulse explained in Fig. 4.6 is left out. In all cases, this negative current observed due to the transit time of the high energy electrons is no longer observed nearly 60 microseconds after the PiP initially discharges.

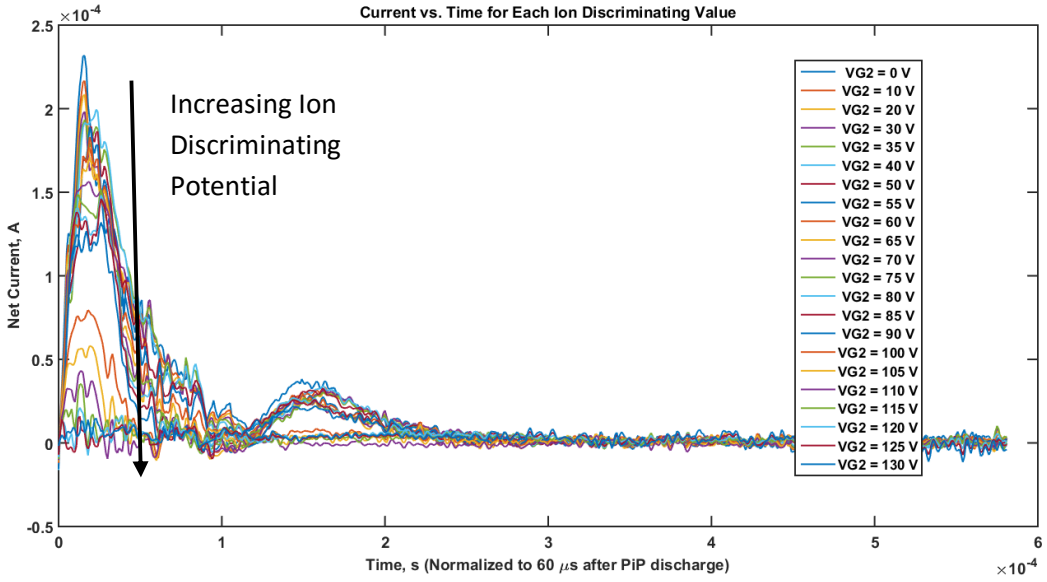

Figure 4.7: A comparison of the currents collected at different discriminating potentials for the time domain in which the plasma has reached the target chamber and is interacting with the analyzer. It is interesting to observe how the analyzer measured currents capture the individual discharges noted by the rings in the current profile of the PiP in Fig. 4.5.

These data in Fig. 4.7 illustrate that the resultant currents collected by the analyzer follow the typical trends expected for probe-type analyses. A concern might stem from the fact that Ref. [2] hypothesized that the plasma duration in the target region only lasts around 150 microseconds, whereas the second peak in Fig. 4.7 shows that there is a secondary ion current collected between 150 and 200 microseconds. This current is not an artifact and can easily be explained in reference to Fig. 4.5, along with the knowledge of the TELS discharge parameters. Knowing the velocity of the plasma for Ref. [2], it can be safely assumed that at the very earliest

the first plasma structure arrives in the target region 50 microseconds after the PiP initially discharges, with the mean time of flight being closer to 60 microseconds. This, however, is the time of flight in reference to the first of two primary plasma structures of interest (denoted in Fig. 4.5 by the rings in the PiP current profile) propagating down the length of the chamber. It is with reference to this initial plasma discharge that the theta pinch fires (set to fire 30 microseconds after the rise of the PiP current reaches a threshold of 60 kA). This pinch sufficiently compresses the primary plasma structure propagating through the theta region, but acts as somewhat of a barrier to the secondary portion of the discharge, which is already propagating behind the primary plasma. The coupling of the lower velocity of the secondary discharge along with the magnetic drag felt by this discharge as it propagates through the theta pinch region easily lends credibility to this second portion of the discharge at 150 μs being the second pulse from the PiP, and, thus, the ion currents collected at these times.

While the data depicted in Fig. 4.7 is indicative of how the collected current waveforms over time decrease with increasing discriminating potential, this figure does not readily portray the curves used to relate the collected current to probe theory. The data in Fig. 4.8 are the currents collected at snapshots in time near the two peaks seen in Fig. 4.7, plotted as functions of the ion discriminating potential. These data show that the currents in relation to the discriminating potential follow the expected probe traces.

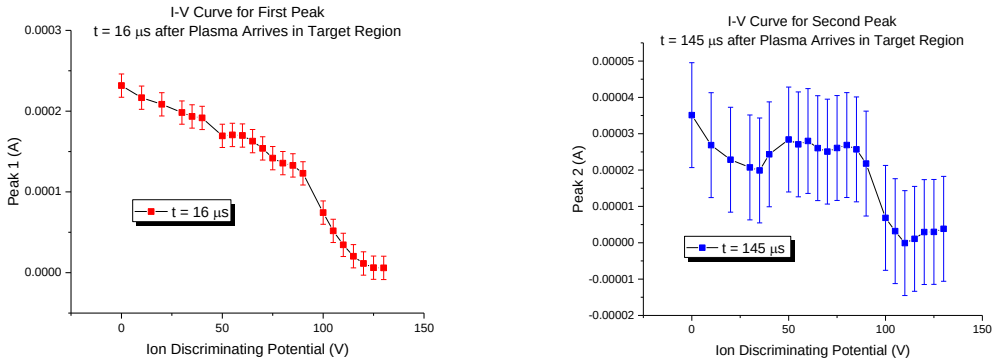

Figure 4.8: (Left) Current as a function of increasing ion discriminating potential for the primary plasma peak that reaches the target chamber the quickest. (Right) Current as a function of increasing ion discriminating potential for the secondary plasma peak that reaches the target chamber the more slowly. The error here is represented by the maximum of the population standard deviation calculated from taking a number of shots at each discriminating potential.

From Fig. 4.8, it is interesting to find that the I-V characteristics are very similar to those found computationally in Fig. 2.17. There are some slight discrepancies from the theoretical predictions, however, that are worth mentioning. First, it seems as if the experimental shifted potential is slightly less than the predicted value (by only approximately 5%). While within reasonable error from the computational values, this may have been caused by line losses when applying the electron repelling potential to the appropriate grid. Second, the decay in these plots are sharper than those predicted in Fig. 2.17, which leads to a smaller ion temperature than that predicted in Ch. 2. This will be made more evident in the next section when the ion temperatures are extracted directly from the energy distributions shown below.

While distributions can be extracted from the plots seen in Fig. 4.8, these data are not fully encompassing of the ion information found during the course of the plasma pulse. As described in Eq. (3.2), the derivative of the current with respect to the discriminating voltage, directly proportional to the distribution, can be used to extract ion temperature values over the TELS pulse time. The temporal evolution of this derivative, directly proportional to the distribution, for the case where the PiP and the theta pinch are in use is plotted in Fig. 4.9. These values are normalized to the peak in order to more easily observe the evolution of the distribution and the growth or decay of key features of the distributions over time. The actual normalized distributions are plotted over time in Fig. 4.10 for comparison.

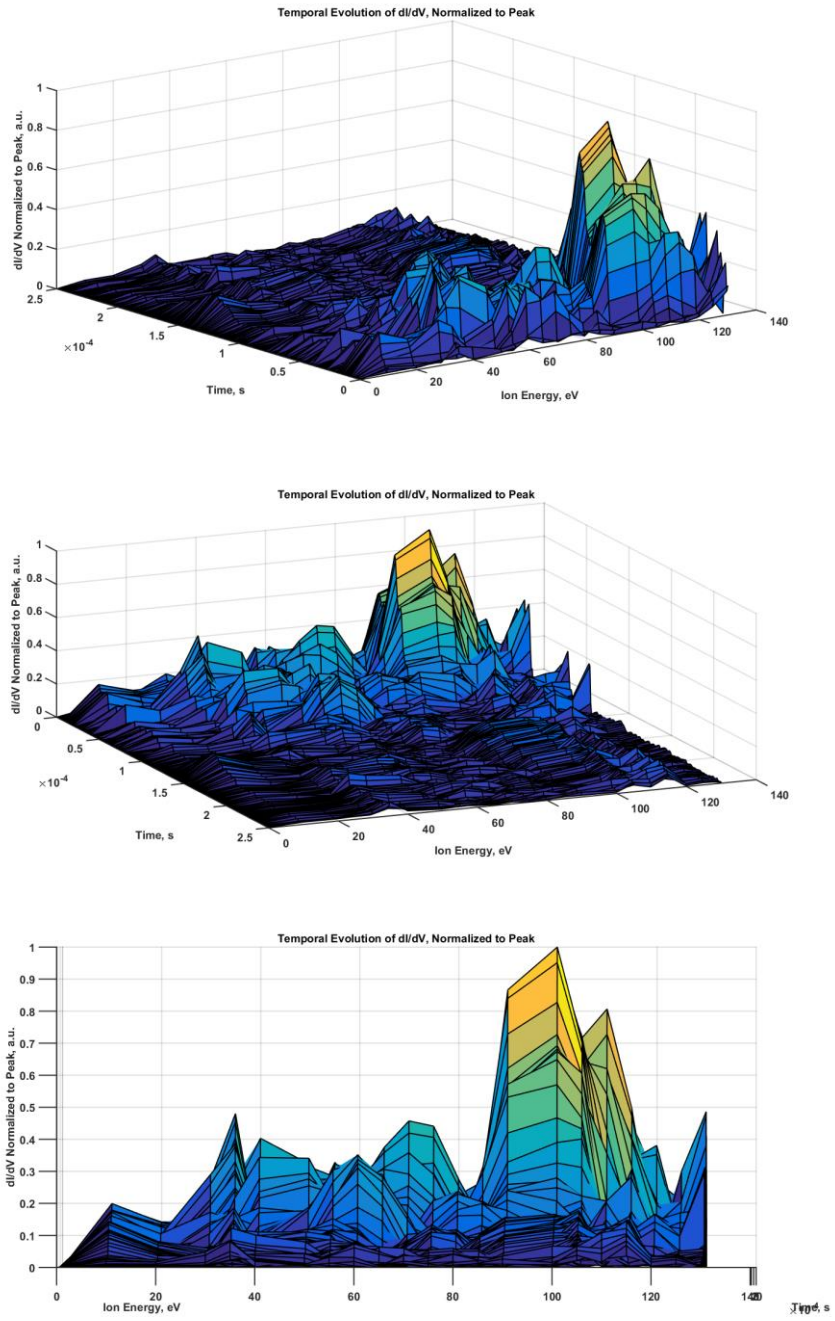

Figure 4.9: Different views of the ion energy distribution function with respect to time of the TELS plasma in the target chamber corresponding to the condition of using both the PiP and the theta pinch. All times are normalized to 60 μs after the PiP discharges.

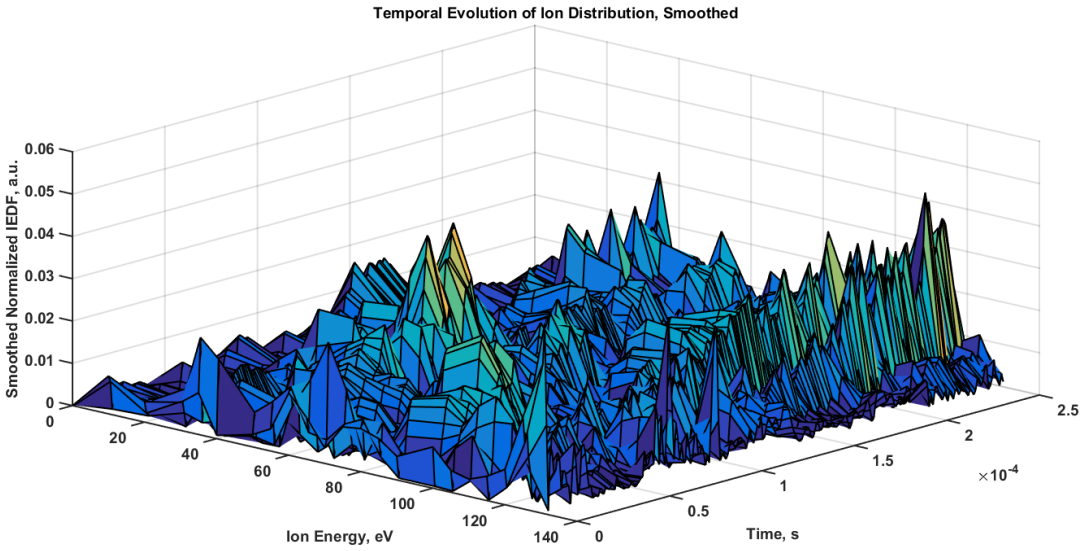

Figure 4.10: The temporal evolution of the normalized ion energy distribution function. This plot was made as a comparison with regards to the plots in Fig. 4.9. The key features are washed out by the noise since the areas under the curves at each time are normalized to unity, making features originally caused by noise seem much more prominent than they actually are. These trends use a 3-point running average over discriminating voltage in an attempt to smooth out the less desirable features, but undesirable features are still observed.

While the above plots are very illustrative in the way they show the evolution of the ion energy distribution, they can only be considered qualitatively. Real information on the way the energy evolves can be observed when taking the normalized distributions at a few key times over the pulse and plotting them relative to each other. This gives a better indication of the distribution evolution and at what times one can expect ions of a given energy value. A plot for the case of the PiP with the θ pinch can be seen in Fig. 4.11, where the two distributions illustrated are indicative of the two primary features in the plasma discharge.

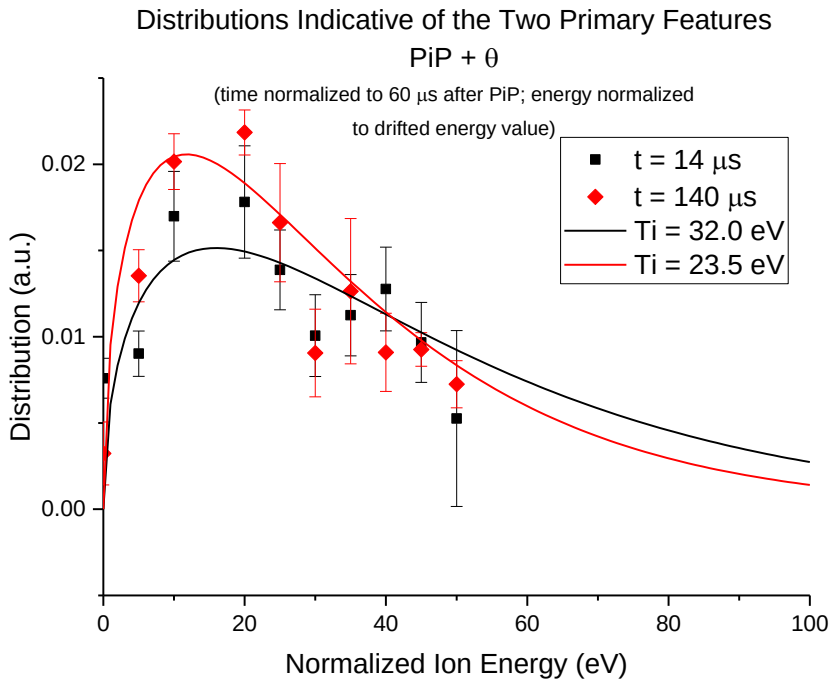

Figure 4.11: A plot of the normalized distributions taken at two different times representing the key features of the discharge. The time is normalized to 60 μs after the PiP discharges, while the energies on the x-axis are normalized to the drifted energy value, illustrated in Fig. 4.9. These data are also plotted against their fitted distributions, with the T_i at 14 μs found to be 32.0 ±12.7 eV, and the T_i at 140 μs found to be 23.5 ± 9.1 eV. The error bars are associated with accumulated error in the form of the standard deviation.

This analysis is incomplete, since the basis of this work is to prove that the ion information is significantly different for cases with and without the use of the theta pinch. This proof must come by analyzing the ion currents collected at the same position in the target chamber for discharges using only the PiP, discharging at the same current and stored potential as the pre-ionization pulses used in the theta experiments. Theoretically, the ion temperature should be much lower for the PiP shots than for the experiments using the theta pinch and crowbar, since these additions preferentially heat the ions due to their much larger Larmour radii. This means that the distribution should be more peaked in the regions of interest. In all cases, the electron repelling potential for the PiP shots was held at only -59 V using 6 9V batteries in parallel. This is due to the primary fact that the measured electron temperatures found in Ref. [2] indicate a smaller electron temperature for PiP shots, as compared with theta pinch experiments. The derivative of the current with respect to the ion discriminating potential, normalized to the peak value, are found in Fig. 4.12.

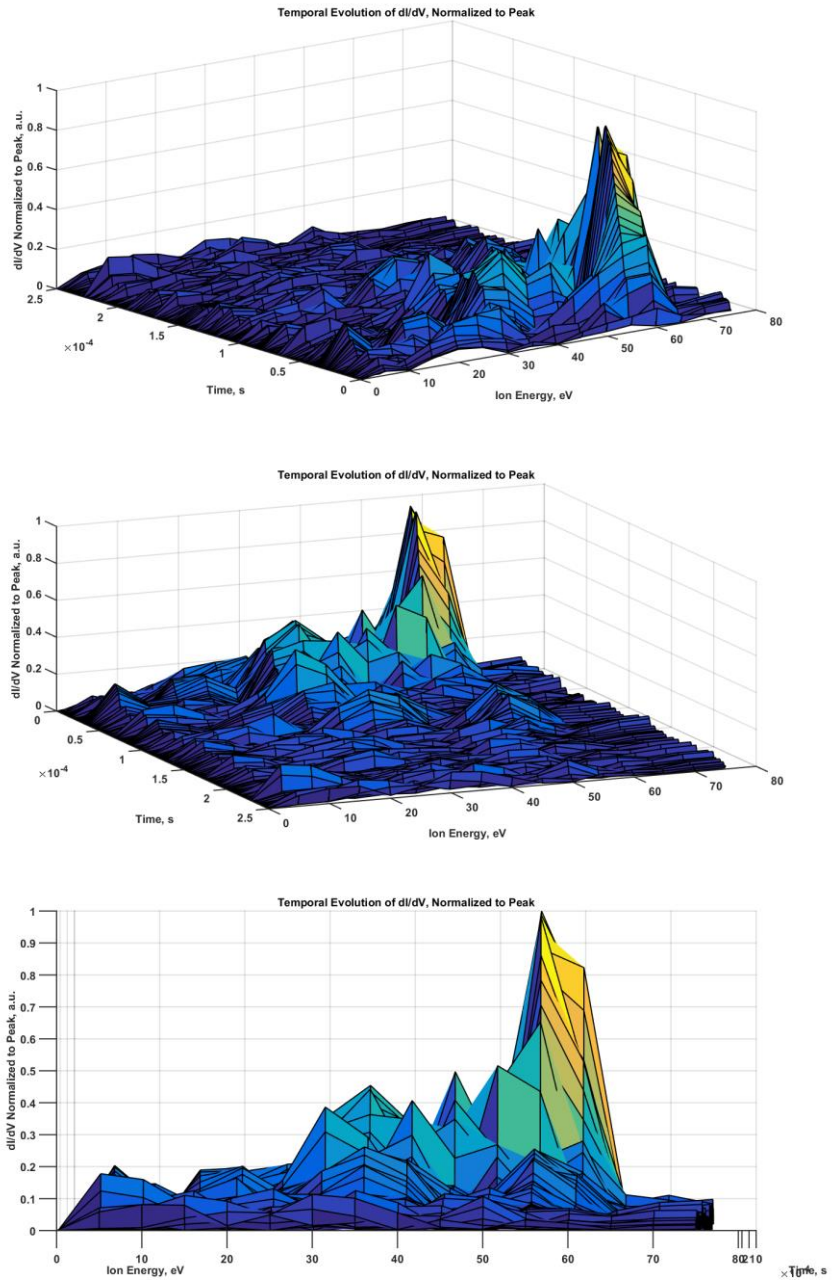

Figure 4.12: Different views of the ion energy distribution function with respect to time of the TELS plasma in the target chamber corresponding to the condition of using both the PiP and the theta pinch. All times are normalized to 60 μs after the PiP discharges.

Similar to the analysis done in the case with the use of the PiP and the theta pinch, a plot of the distributions for each discharge case at key points in time were plotted against one another to observe the impact the theta pinch has on ion compression and transport. These plots were normalized in time to observe the key features as they interact with the analyzer. This means that the case with the PiP and theta pinch was normalized to 60 μs after the PiP discharge and the case with just the PiP was normalized to 70 μs after the PiP discharge. Both distributions were normalized to their respective drifted energy values, which can be seen in Fig. 4.9 and Fig. 4.12. The plots can be found in Fig. 4.13.

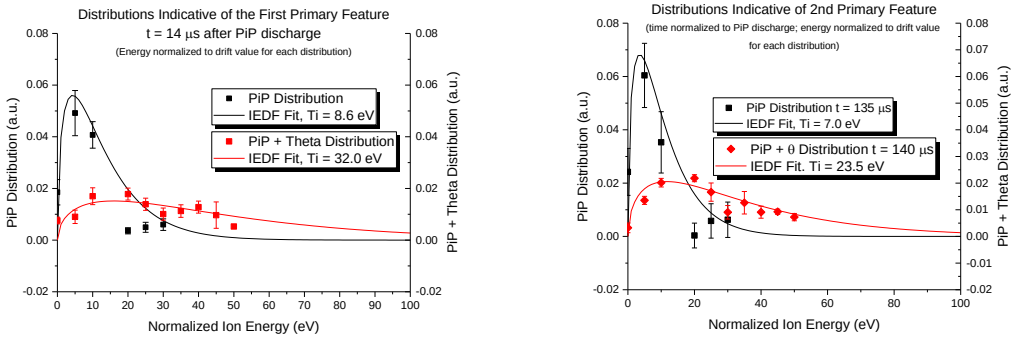

Figure 4.13: A plot of the normalized distributions taken at two different times representing the key features of the discharge. The time is normalized to 60 μs after the PiP discharges for the case of the PiP + θ pinch, and to 70 μs after the PiP discharges for the case of the PiP. For the first primary feature, the fit T_i value for the PiP + θ pinch was found to be 32.0 ±12.7 eV, while the fit T_i for the PiP only was found to be 8.6 ± 2.7 eV. For the second primary feature, the fit T_i value for the PiP + θ pinch was found to be 23.5 ± 9.1 eV, while the fit T_i for the PiP only was found to be 7.0 ± 2.2 eV.

4.2.2 Temporal Evolution of Ion Temperature

While the ion energy distributions are the most important information that can be collected from an analysis such as this, the ion temperatures are typically how the energy spectrum is quantified in relationship to other plasma parameters. Because TELS is a pulsed device and the entirety of the pulse affects the relationship between the plasma and the materials being bombarded, a significant amount of knowledge can be gained by extracting the ion temperatures from the time-resolved distributions plotted in the previous subsection. The ion temperatures can be found by fitting each of these distributions at a given instance in time to the equation:

$$f_E(E) = 2\left(\frac{1}{T_i}\right)^{3/2}\sqrt{\frac{E-E_d}{\pi}}\exp\left(\frac{-(E-E_d)}{T_i}\right) \quad (4.1)$$

where E is the energy in eV, E_d is the drifted energy in eV, and T_i is the ion temperature in eV. As such, the ion temperature can easily be understood in terms of the width of a peaked Maxwellian energy distribution. From this equation, Eq. (3.5) can be derived in terms of probe theory. Using Eq. (4.1) to fit to each distribution as a function of time is adequate for these situations since the plasma acts in accordance with Maxwellian theory, while the bulk carries a drifting velocity component. An image depicting how each distribution at a given time was fit to Eq. (4.1) can be seen in Fig. 4.14.

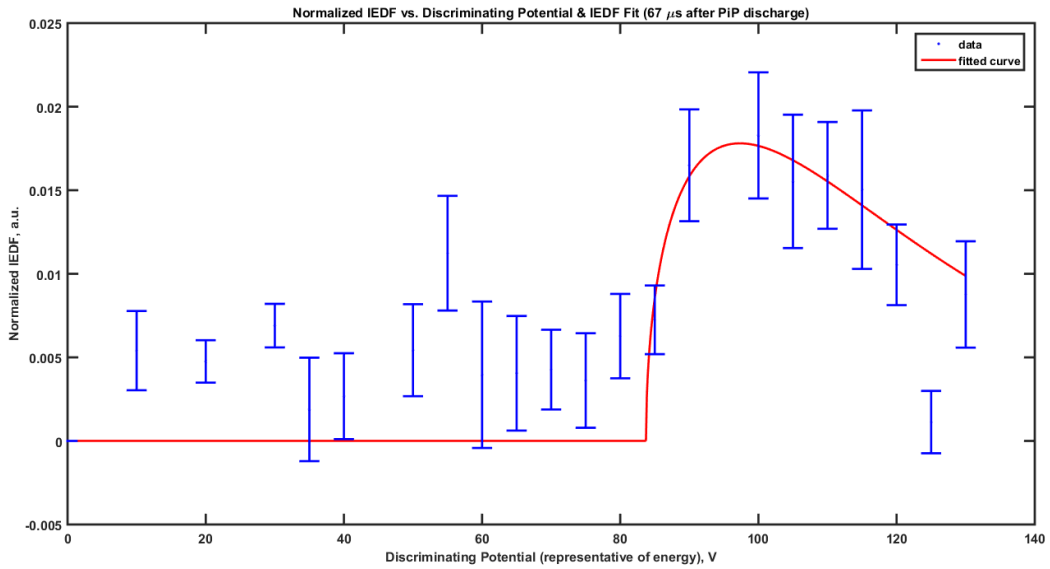

Figure 4.14: Representative plot of how the distributions at given points in time were fit to the drifted Maxwellian Energy distribution, illustrated in Eq. (4.1). This plot was extracted from 67 μs after the initial PiP dicharge. The ion temperature found from this trend fit was nearly 27.18 ± 9.41 eV. The error bars here are associated with the accumulated error in the form of the standard deviation.

Doing similar trend fits at multiple instances in time allowed for the development of a plot to illustrate how the ion temperature of the pulse evolved over time. The temporal evolution of the ion temperature can be seen in Fig. 4.15. This evolution is for the case where the combination of the PiP and theta pinch are used.

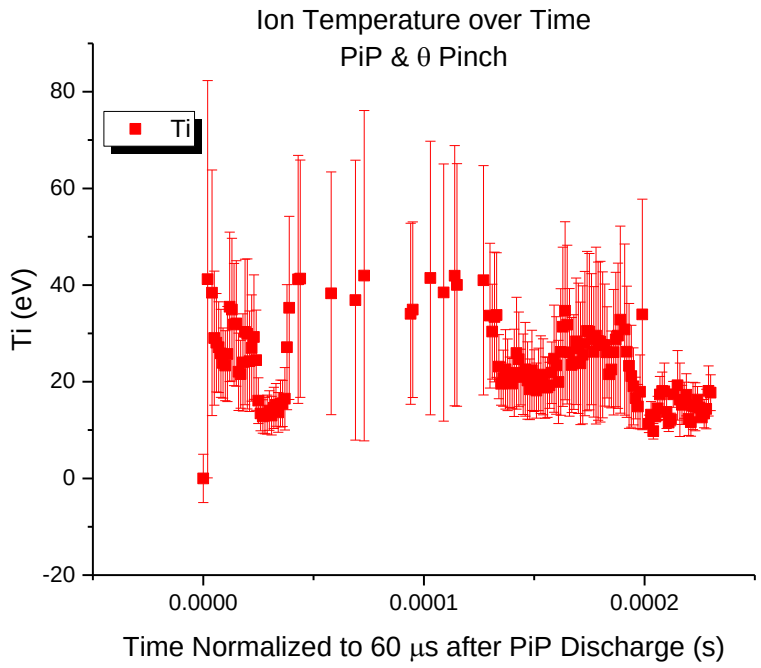

Figure 4.15: The temporal evolution of the ion temperature for the discharge case including the PiP and theta pinch. Peak temperatures for the first peak range between 30 and 40 eV, while the peak temperatures for the second peak range between 20 and 30 eV. Error bars indicate 95% confidence intervals in the fitting routine. A number of the values not seen correspond to errors in the fit routine employed in Fig. 4.14. This was due to the prevalence of undesirable features found after normalizing the distribution, seen in Fig. 4.10.

These data represent a very meaningful result, in that the ion temperature over the entirety of the duration where the plasma interacts with the analyzer are very similar in magnitude to theoretically predicted values. A similar analysis was done for the case where the analyzer was subjected only to the bombardment from the PiP. The expected trend for this would be that the magnitude of the ion temperatures should be substantially less than those for the case with the theta pinch. The temporal evolution of the ion temperature measured by the analyzers subjected to only PiP discharges can be seen in Fig. 4.16.

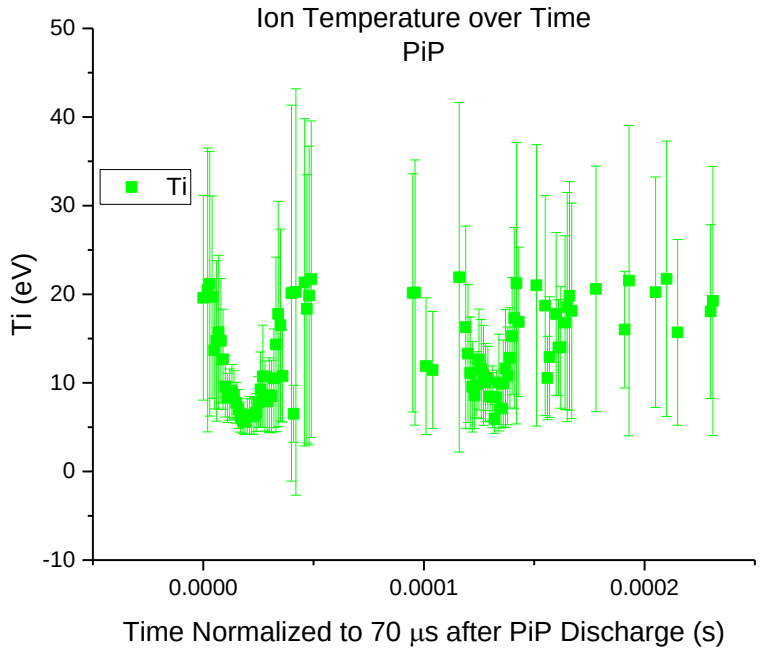

Figure 4.16: The temporal evolution of the ion temperature for the discharge case including the PiP and theta pinch. Peak temperatures for the first peak range between 10 and 20 eV, while the peak temperatures for the second peak are near 10 eV. Error bars indicate 95% confidence intervals in the fitting routine. A number of the values not observed correspond to errors in the fit routine employed in Fig. 4.14. This was due to the prevalence of undesirable features found after normalizing the distribution.

While these ion temperatures are reasonably high for any given plasma system, they are slightly low when compared to the theoretical predictions from the assumption of a Maxwellian plasma and the solution to the ideal MHD equations using the Athena MHD code in Ch. 2. The reason for this discrepancy can be explained using a justification based on radial positioning. In Fig. 3.6, it can be seen that the radial positioning of the analyzers is 1.75 inches away from plasma center. It is also clear from this image that the plasma strike on the surface of the 430 stainless steel exhibits what seems to be an axisymmetric, Gaussian-like profile. This profile is once-again illustrated in Fig. 4.17 for clarification purposes. Further investigations on the radial dependence of the ion temperature as well as the energy deposition may shed light onto the peak ion temperature felt by targets in TELS. This will be a topic for future discussion.

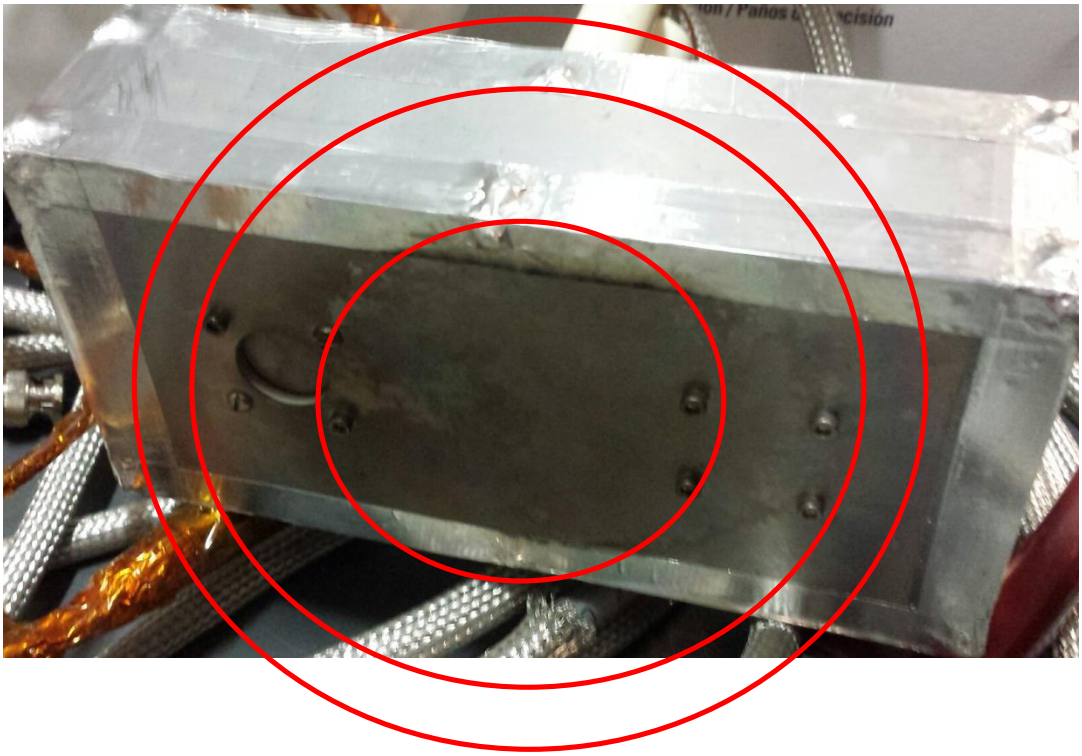

Figure 4.17: An image of an earlier iteration of the analyzer configuration as it sits in the 430 stainless steel box. The red rings indicate the concentric plasma strike patterns noticed on the surface of the box facing normal to the direction of the incoming plasma.

4.2.3 Extension to Other Plasma Parameters

The basis of the work done previously to measure the effectiveness of TELS as an ELM simulator used energy deposition values obtained through calorimetry as the primary indicator. To do this, the heat flux of the plasma delivered to the target was calculated using[2,80]:

$$\vec{Q}_\sigma = \frac{1}{2} n_\sigma m_\sigma (\vec{v}_\sigma \cdot \vec{v}_\sigma)\vec{v}_\sigma + \frac{5}{2} p_\sigma \vec{v}_\sigma + \vec{v}_\sigma \cdot \vec{\vec{\pi}}_\sigma + \vec{q}_\sigma \qquad (4.2)$$

where σ represents the species in question, m is the mass of the species, n is the number density of the species, $\vec{v}_\sigma$ is the advection velocity term for species σ, p is the plasma pressure, $\vec{\vec{\pi}}_\sigma$ is the shear stress tensor term, and $\vec{q}_\sigma$ is the heat conduction term for species σ. As described in Ref. [2], for an isotropic thermal velocity distribution, the heat source and shear stress tensor terms disappear and the equation for species σ is reduced to the form:

$$\vec{Q}_{\sigma,iso} = \frac{1}{2} n_\sigma m_\sigma (\vec{v}_\sigma \cdot \vec{v}_\sigma)\vec{v}_\sigma + \frac{5}{2} p_\sigma \vec{v}_\sigma \qquad (4.3)$$

which, when applying the kinetic approximation for the plasma pressure, reduces to the form:

$$\vec{Q}_{\sigma,iso} \sim (\frac{1}{2} n_\sigma m_\sigma v_\sigma^2 + \frac{5}{2} n_\sigma k T_\sigma)\vec{v}_\sigma \tag{4.4}$$

When assuming that the flow velocity is the same for both ions and electrons and assuming that the plasma is fully ionized, the isotropic heat flux of the plasma can be approximated as:

$$\vec{Q}_{\sigma,iso} \sim (\frac{1}{2} n_e (m_i v_0^2 + m_e v_0^2) + \frac{5}{2} n_e k (T_i + T_e))\vec{v}_0 \tag{4.5}$$

In this form, the isotropic heat flux is easily calculated from measured plasma values.

Unfortunately, the work done in Ref. [2] was incomplete in its comparison between calorimetric energy deposition values and energy deposition values found by calculating the isotropic heat flux from Eq. (4.5). This was because the ion temperatures prior to this work were not well known for the TELS device. On top of this, the work done in Ref. [2] used calorimetry dependent on the change in temperature registered by a K-type thermocouple attached to the back of a button calorimeter. Two issues arise from this type of measurement. First, the sensitivity of the thermocouple head is on the order of milliseconds, meaning that the thermocouple can only register the after effects of the plasma bombardment and not the actual heating effects over the duration of the pulse. Second, the diameter of the calorimeter is only 0.25 inches, which is much less than the plasma diameter, as observed in Fig. 4.17.

To complete this work, the instantaneous isotropic heat flux was measured for the pulse duration using a density of 10^{21} m^{-3}, an advection velocity ranging from 40 km s^{-1} to 65 km s^{-1}, and an electron temperature ranging from 30 eV to 50 eV, all of which were measured in Ref. [2]. This was done for the case of the use of the PiP and the θ pinch. For the use of the PiP only, the density was still assumed to be 10^{21} m^{-3}, but the advection velocity was modified to range between 24 km s^{-1} and 40 km s^{-1} and the electron temperature was modified to range between 10 and 30 eV. These parameters were again chosen based on information collected from Ref. [2]. Plots illustrating the instantaneous heat flux during the pulse can be seen in Fig. 4.18.

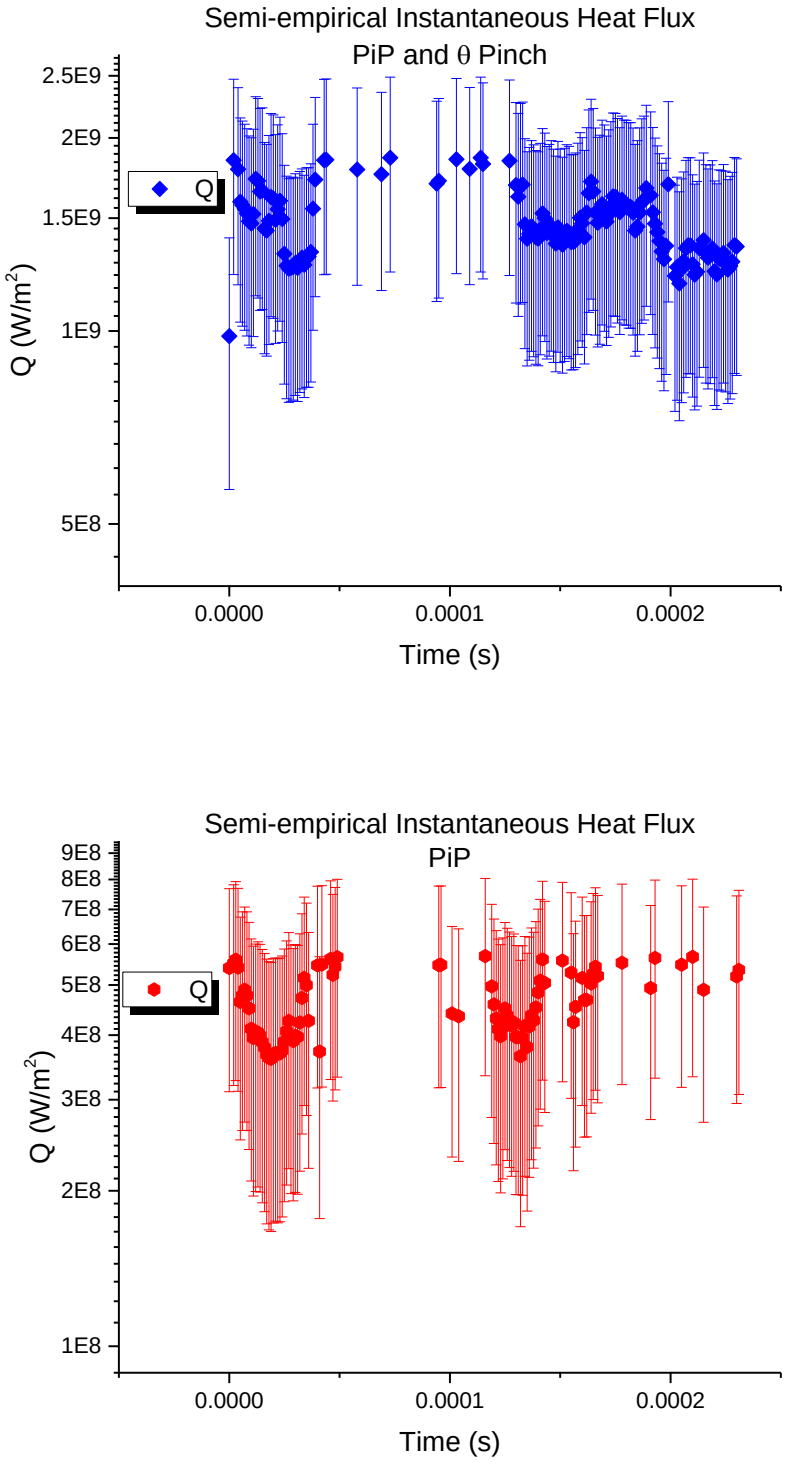

Figure 4.18: (Top) The instantaneous power deposition values on target during a TELS pulse using ion temperature values found in Fig. 4.14. (Bottom) The instantaneous power deposition values on target during a PiP pulse using ion temperature values found in Fig. 4.15. The large errors are the standard deviations associated with the accumulation of the uncertainties in T_e and v_0 from Ref. [2] and in T_i.

It is important to note from Fig. 4.18 the difference between the semi-empirical heat flux values found for the use of the PiP and θ pinch as compared with the use of the PiP only. The heat flux values are nearly a factor of 3 higher when using the theta pinch, indicating that the theta pinch is effective in compressing and heating the ions well beyond what the PiP is capable of. Now, taking the time averaged ion temperature values from each distribution, the time-averaged power deposition and subsequent energy deposition can be calculated for similar conditions as those used to generate the instantaneous power deposition trends found in Fig. 4.18. These results are summarized in Table 4.1, which can be compared directly to the values found in Ref. [2], assuming a 170 μs pulse. The values in Ref. [2] assume a 100 μs pulse only, which would in part explain the discrepancy in reported values between Ref. [2] and those reported here.

Table 4.1: A summary of the energy deposition values found by applying experimentally measured values to Eq. (4.5). These values are calculated for the cases where the PiP and θ pinch are in use and where only the PiP is in use.

	PiP + θ	PiP
Pulse-Averaged Q_{iso} GW m^{-2}	1.50 ± 0.20	0.46 ± 0.07
Pulse-Averaged E MJ m^{-2}	0.26 ± 0.03	0.08 ± 0.01

The overall peak energy deposition value measured using the button calorimeter in Ref. [2] was found to be nearly 0.08 MJ m^{-2}. This peak value is nearly 2 to 3 times less than what is predicted by applying the experimentally measured values of the time-averaged ion and electron temperatures. The reason for this discrepancy when compared with semi-empirical predictions of the isotropic heat flux is due to a few reasons. First, those values experimentally measured through calorimetry in Ref. [2] were conservative in that the energy deposited on target was considered for a pulse length of only 100 μs. This is conservative, since a number of other calculated values found in Ref. [2] can be seen to extend beyond this pulse limit to range between 150 and 200 μs. The second, and more important, reason for the discrepancy between the values reported here and the values reported in Ref. [2] is based again on time. The thermocouple measurement used to deduce the energy deposited on a button-type calorimeter has

a maximum resolution of 100 ms. This time resolution is a major issue, especially when attempting to measure instantaneous heat flux values of a pulse that lasts on the order of 100's of μs. All calorimetry measurements taken in Ref [2] take the difference between the peak value registered by the thermocouple through the use of a U6 Labjack interface and the initial value as the ΔT, but the peak value may already have been subjected to conductive, convective, and radiative cooling by the time the acquisition program has registered the "peak". It is for these reasons that further investigation of the heat flux values on target need to be considered for this device, since values in Ref. [2] are conservatively reported.

CHAPTER 5: CONCLUSIONS AND FUTURE WORK

5.1 Conclusions

As the world approaches the point where non-renewable resources become impractical as a viable energy source, alternatives must not only be researched, but must be realized. Imperative to the realization of steady-state, magnetically confined fusion energy is the mitigation and elimination of high-energy, off-normal events. The reason these events are so detrimental is that they can cause immediate plasma failure and loss of confinement, and can irreversibly damage the wall materials that are subjected to these extreme heat loads. Alternatives to solid wall materials, such as the LiMIT device from the University of Illinois in Urbana-Champaign[29,30], have been studied, but require very controlled conditions for experimentation. It is for this reason, along with the fact that an in-house ELM simulator is priceless in terms of fusion and fusion materials research, the TELS device was constructed and upgraded[2].

To be able to adequately simulate ELM events, TELS must not only be considered in terms of its heat flux and energy deposition, but also in terms of the highly transient plasma parameters. An understanding of these conditions allows for a better comprehension of how exactly the plasma interacts with the materials upon which energy is deposited. This is important when considering flowing liquid surfaces and the effects the charged particles have on TEMHD flow, from both a pressure and current standpoint. It is for these reasons that the measurement of the TELS ion information was conducted, and the results were considered with respect to the discharge duration. Careful consideration was made when designing the experimental analyzer system so as to not be vulnerable to physical limitations such as space charge and plasma penetration. These results were also loosely compared with a computational model, still under development, that took the results from a combination of the Athena MHD TELS model, a particle-mesh code to capture the kinetic effects of the collimating grid or slit, and a COMSOL Monte Carlo simulation to simulate ion travel through the analyzer. Before the experiments and computational results can be directly compared, future work must be done to update the model to

be more predictive in nature. In this vein, priority must be placed on accurately modeling the sheath by revising the kinetic particle mesh work.

The ion information was collected and the energy distributions and ion temperatures were calculated with respect to the discharge time. From measurements taken in Ref. [2], the plasma takes approximately 45 to 60 μs to travel down the length of the chamber, meaning that the data prior to approximately 55 μs after initial coaxial plasma thruster pulse is due to either electromagnetic noise or is the very high energy, low probability electron portion of the plasma distribution, of which target materials are less likely to react to when compared to the cumulative effects from the remainder of the pulse happening between 60 and 250 μs. From the distributions found at two different discharge conditions, ion temperatures were calculated with respect to time and compared to understand the effect the theta pinch has on ion energy and motion.

Under the assumption that the TELS plasma is highly Maxwellian and operates under nearly ideal MHD conditions, instantaneous ion temperatures were found from the time-resolved distribution functions by fitting the distributions to drifted Maxwellian energy distributions. These fits as a function of time were then averaged to find the time-averaged ion temperature for the pulse discharge. At the position corresponding to the optimal positioning for targets in the target chamber of the TELS device, the time-averaged ion temperature per primary feature was found to be 22.83 ± 7.43 eV for the first peak and 17.59 ± 11.53 eV for the second peak. Using only the PiP, the time-averaged ion temperature per primary feature was found to be 10.40 ± 6.62 eV for the first peak and 7.70 ± 3.57 eV for the second peak. These temperatures were found to be lower than the value found in using the computational model in Ch. 2, but only by less than a factor of 2. While this might seem to indicate that the computational model of Ch. 2 can in some way inform the experimentation, this similarity in temperature is more likely coincidental and less likely a prediction from the computational model, as explained in Ch. 2. This is caused by a number of reasons, mostly associated with the simulation parameters. A number of modifications to the simulation must be made before the experimental results and the simulation results can be directly compared.

These results were then extended to the theoretical predictions governing the isotropic heat flux felt by targets in TELS. By applying the experimentally measured values of the electron[2] and ion temperatures, the instantaneous heat fluxes were found as a function of the

discharge duration. The time-averaged values of the ion and electron temperatures were also used to find the time-averaged isotropic heat flux in order to find the semi-empirical energy deposited on a target. These values indicate that the heat flux from the full plasma profile was under sampled in Ref. [2] and the actual energy deposited on a target should be closer to 0.2 MJ m^{-2} to 0.3 MJ m^{-2}. Plot (b) in Fig. 3.2 can therefore be updated with respect to the TELS energy deposition value to the plot seen in Fig. 5.1.

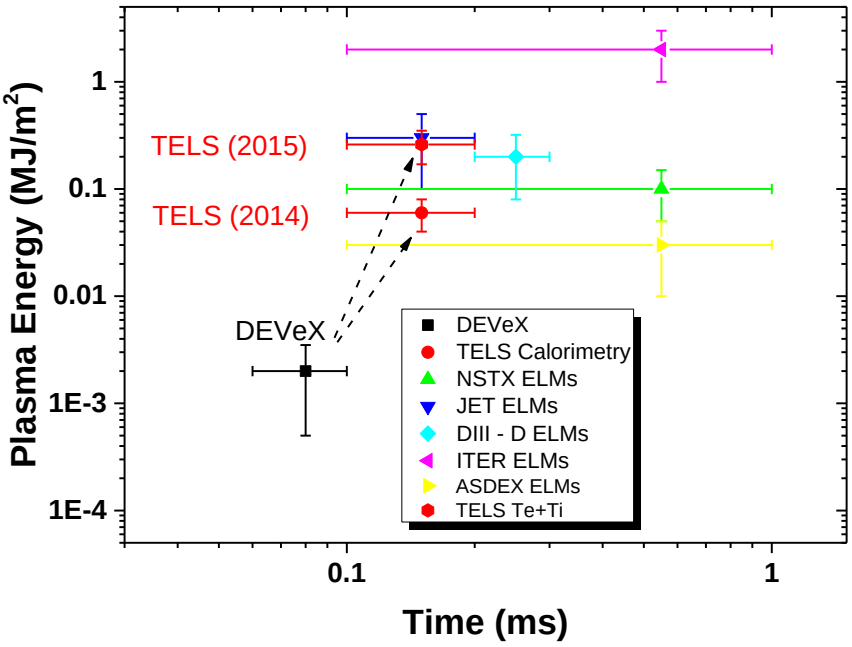

Figure 5.1: An updated form of plot (b) in Fig. 3.2. This plot illustrates the energy deposited on target from the TELS device using two different experimental methods when compared with larger machine ELM energy deposition values.

5.2 Future Work

This work presented the extraction of ion information from the TELS device, both through the use of computational tools as well as experimentally using an ion energy analyzer system. To help further validate and verify the results obtained in this report, a number of future endeavors can be carried out computationally and experimentally. These potential additions to

the results presented in this report are outlined below and are ordered in reference to the way this report was presented.

- The computational model can be expanded and further developed in a number of ways. First, the results from the Athena MHD simulation in terms of the velocity distribution functions should be extracted as a function of virtual discharge time. The computational results in this report were only a function of a single set of values extracted at 2.44 μs into the simulation time domain, but extracting this information as a function of time would be very useful to understand the approach to the kinetic particle-mesh simulation. Second, the particle-mesh simulation should be modified to apply the appropriate particle-to-computational value, grid spacing, virtual density, and electric field domain. To do so, it is necessary to reduce the domain size down in order to investigate what happens on a spatial scale much closer to the experimentally observed Debye length. Other future work is listed in Chapter 2, where the underlying subroutines and boundary conditions of the particle mesh simulation must be modified before the work can loosely be called predictive. This will be made a major future priority, since the current prototype model cannot be at all correlated with any meaningful physical result.
- The analyzer configuration should be modified in one major way. To adequately sample the peak in the ion information corresponding to the peak seen in both the heat flux and the electron temperature[2], the analyzer body should be made such that the open and closed analyzers are closer to plasma center. This second modification may require a reduction in the diameter of the probe body. The analyzer grids and their MACOR® holders should also be modified so that the distance between grids can be changed based on the plasma being sampled.
- Analysis of the current-voltage relationships used to calculate the energy distribution functions and the subsequent ion temperatures should be reiterated, both in the positions corresponding to the results of this report and in other axial positions. This will help establish a greater dependence on the distance away from the exit of the theta pinch and will give a better clue as to the magnitude of ion loss in the fringing field of the theta pinch. In this same vein, it would be necessary to run the same analysis at the optimal target position using the guiding magnet field and the capacitor charge for each set of magnets corresponding to the highest heat flux found in the transport analysis of Ref. [2].

- Construct a bucket-type calorimeter in order to verify that the heat flux measured in previous experiments is under sampled. This should be done in conjunction with the use of an analysis that provides for better time resolution. In this way, not only will the total energy deposited on a target be better understood, but the instantaneous heat flux values during the pulse duration will be measured more accurately.

The results gained from the work listed above will be able to provide a more accurate basis on which the plasma-material and ion-material interactions can be quantified. These new results, along with those obtained in this report and Ref. [2], will help to prove that TELS is a viable ELM simulator. This, in turn, will help the University of Illinois at Urbana-Champaign move forward in selecting the most appropriate plasma-facing structures as it seeks to make magnetically confined fusion a reality.

REFERENCES

[1] S. Jung, M. Christenson, et al., “Development of a high energy pulsed plasma simulator for the study of liquid lithium trenches”, Fusion Engineering and Design (2014), http://dx.doi.org/10.1016/j.fusengdes.2014.02.061.

[2] S. Jung (2014). Development of high energy pulsed plasma simulator for plasma-lithium trench experiment. (Doctoral dissertation). University of Illinois at Urbana-Champaign, 2014.

[3] S. Jung, et al., “Characterization of a theta-pinch plasma using triple probe diagnostic”, Journal of Nuclear Materials 415 (2011) S993-S995.

[4] J. Ongena and G.V. Oost, “Energy for future centuries”, Laboratorium voor Plasmafysica Laboratoire de Physique des Plasmas Koninklijke Militaire School Ecole Royale Militaire, Laboratorium voor Natuurkunde, Universiteit Gent. pp. Section III.B. and Table VI .

[5] J.D. Lawson, “Some Criteria for a Useful Thermonuclear Reactor,” Culham Laboratory Internal Report (1955) United Kingdom Atomic Energy Authority.

[6] M. Hermann, “Plasma physics: A promising advance in nuclear fusion,” Nature, vol. 506 (2014), pp. 302-303.

[7] R. Aymar, “Overview of ITER-FEAT – The future international burning plasma experiment”, Nuclear Fusion 41 (2001) 1301.

[8] S. Cowley, et al., “ITER: Burning Plasmas – Challenges”, Culham Centre for Fusion Energy. http://www.psfc.mit.edu/library1/catalog/online_pubs/iap/iap2011/cowley.pdf. Accessed: 2014-11-05.

[9]D. Swain, et al., “High-beta injection experiments on the ISX-B tokamak”, Nuclear Fusion, vol. 21, no. 11 (1981) pp. 1409.

[10] F. Wagner, et al., “Regime of improved confinement and high beta in neutral-beam-heated divertor discharges of the asdex tokamak”, Physical Review Letters, vol. 49, no. 19 (1982) pp. 1408-1412.

[11] J.R. Walk, et al., “Characterization of the Pedestal in Alcator C-Mod ELMing H-Modes and Comparison of the EPED Model”, Nuclear Fusion, vol. 52, no. 6 (2012) 063011.

[12] E.J. Doyle, et al., “ITPA Transport Physics Topical Group, ITPA confinement Database, Modelling Topical Group, ITPA Pedestal, and Edge Topical Group”, Nuclear Fusion, vol. 47, no. 6 (2007) S18.

[13] M. Greenwald, et al., “H mode confinement in alcator c-mod”, Nuclear Fusion, vol. 37, no. 6 (1997) 793.

[14] A.E. Hubbard, et al., “Measurements of the high confinement mode pedestal region on alcator c-mod”, Physics of Plasmas, vol. 5, no. 5 (1998) pp. 1744-1751.

[15] A.W. Leonard, W. Suttrop, T.H. Osborne, Journal of Nuclear Materials, 241-243 (1997) 628.

[16] W. Suttrop, K. Schonmann, J. Schweinzer, et al., in: Procedures 22nd EPS Conference on Controlled Fusion and Plasma Physics, Bournemouth, 1995, p. III-237.

[17] R. Mohanti, C. Brickley, J.P. Christiansen, et al., in: Procedures 23rd EPS Conference on Controlled Fusion and Plasma Physics, Berchtesgaden 1995, p. I-101.

[18] S.J. Fielding, K.B. Axon, M.G. Booth, et al., Journal of Nuclear Materials, 241-243 (1997) 902.

[19] Y. Kamada, K. Ushigusa, O. Naito, et al., Plasma Physics of Controlled Fusion, 36 (1994) A123.

[20] A.W. Leonard, A. Herrmann, K. Itami, J. Lingertat, A. Loarte, T.H. Osborne, W. Suttrop, the ITER Divertor Modeling and Database Expert Group, the ITER Divertor Physics Expert Group, “The impact of ELMs on the ITER divertor”, Journal of Nuclear Materials, 266-269 (1999) pp. 109-117.

[21] D.P. Boyle, R. Maingi, P.B. Snyder, J. Manickam, T.H. Osborne, R.E. Bell, B.P. LeBlanc, and the NSTX team, “The relationships between edge localized modes suppression, pedestal profiles and lithium wall coatings in NSTX”, *Plasma Physics and Controlled Fusion*, vol. 52, no. 10 (2011) p. 105011.

[22] A. Kirk, J. Harrison, Yueqiang Liu, E. Nardon, I. Chapman, P. Denner, “Observation of Lobes near the X Point in Resonant Magnetic Perturbation Experiments of MAST”, *Physical Review Letters*, vol. 108, no. 25 (2012) 255003.

[23] R. Arnoux, “Preparing for the future at Tore Supra”, iter newsline, http://www.iter.org/newsline/126/223, Accessed: 2014-11-5.

[24] G. Federici, C. Skinner, J. Brooks, J. Coad, C. Grisolia, A. Haasz, A. Hassanein, V. Philipps, C. Pitcher, J. Roth, W. Wampler, and D. Whyte, “Plasma-material interactions in current tokamaks and their implications for next step fusion reactors," *Nuclear Fusion*, vol. 41, no. 12 (2001) p. 1967.

[25] M. Baldwin, R. Doerner, S. Luckhardt, and R. Conn, “Deuterium retention in liquid lithium," *Nuclear Fusion*, vol. 42, no. 11 (2002) p. 1318.

[26] R. Majeski, S. Jardin, R. Kaita, T. Gray, P. Marfuta, J. Spaleta, J. Timberlake, L. Zakharov, G. Antar, R. Doerner, S. Luckhardt, R. Seraydarian, V. Soukhanovskii, R. Maingi, M. Finkenthal, D. Stutman, D. Rodgers, and S. Angelini, “Recent liquid lithium limiter experiments in CDX-U," *Nuclear Fusion*, vol. 45, no. 6 (2005) p. 519.

[27] J.P. Allain, D.L. Rokusek, S.S. Harilal, M. Nieto-Perez, C.H. Skinner, H.W. Kugel, B. Heim, R. Kaita, R. Majeski, “Experimental studies of lithium-based surface chemistry for fusion plasma-facing materials applications”, *Journal of Nuclear Materials*, vol. 390-391 (2009) pp. 942-946.

[28] H.W. Kugel, D. Mansfield, R. Maingi, M.G. Bell, R.E. Bell, J.P. Allain, D. Gates, S. Gerhardt, R. Kaita, J. Kallman, S. Kaye, B. LeBlanc, R. Majeski, J. Menard, D. Mueller, M. Ono, S. Paul, R. Raman, A.L. Roquemore, P.W. Ross, S. Sabbagh, H. Schneider, C.H. Skinner, V. Soukhanovskii, T. Stevenson, J. Timberlake, W.R. Wampler, J. Wilgren, L. Zakharov, the

NSTX Team, “Evaporated lithium surface coatings in NSTX”, *Journal of Nuclear Materials*, vol. 390-391 (2009) pp. 1000-1004.

[29] D.N. Ruzic, W. Xu, D. Andruczyk, M.A. Jaworski, “Lithium-metal infused trenches (LiMIT) for heat removal in fusion devices”, *Nuclear Fusion*, vol. 51 (2011) 102002.

[30] W. Xu, et al., *Journal of Nuclear Materials*, vol. 415 (2013).

[31] I. H. Hutchinson, *Principles of Plasma Diagnostics*, 2nd ed., Cambridge University Press, 2002.

[32] C.R. Parsons, S.S. Medley, *Plasma Physics*, vol. 16 (1974) pp. 267-273.

[33] V.V. Afrosimov, I.P. Gladkovskii, *Soviet Phys. Tech. Phys*., vol. 12 (1968) p. 1135.

[34] D.W. Mason, J.M.S. Schofield, Culham Laboratory Report CLM-R (1966) p. 49.

[35] C.F. Barnett, J.A. Ray, Oak Ridge National Laboratory Report ORNL-TM-34 (1971).

[36] S. Robertson, P. Korn, and C.B. Wharton, Cornell University Report LPS (1972) p. 110.

[37] V.S. Mukhovatov, M.P. Petroc, and L.D. Sinitsyna, *Fourth Conference on Plasma Physics and Controlled Nuclear Fusion*, Madison (1971) CN-28/F-8.

[38] V.V. Afrosimov, M.P. Petrov, *Soviet Phys. Tech. Phys*., vol. 12 (1968) p. 1467.

[39] H. Kimura, H. Maeda, N. Ueda, M. Seki, H. Kawamura, S. Yamamoto, M. Nagami, K. Odajima, S. Sengoku, and Y. Shimomura, *Nuclear Fusion*, vol. 18 (1978) p. 1195.

[40] H. Kimura, K. Odajima, T. Sugie, and H. Maeda, *Japanese Journal of Applied Physics*, vol. 18 (1979) p. 2275.

[41] M. El Shaer, Plasma De Bord Dans un Tokamak Mesures et Simulation Numerique Application au Chauffage Hybride du Plasma de WEGA. (Doctoral dissertation). L’Universite Scientifique et Medicale de Grenoble, 1981.

[42] G.F. Matthews, *Journal of Physics D*, vol. 17 (1984) p. 2243.

[43] G.F. Matthews, The measurement of ion temperature in tokamak edge plasmas. (Doctoral dissertation). Wolfson College, 1984.

[44] D. Brunner, B. LaBombard, R. Ochoukov, D. White, "Scanning retarding field analyzer for plasma profile measurements in the boundary of the Alcator C-Mod tokamak", *Review of Scientific Instruments,* 84 (2013) 033502.

[45] I.S. Nedzelskiy, C. Silva, H. Figueiredo, et al., "Compact retarding field energy analyzer for the tokamak ISSTOK boundary plasma", *Review of Scientific Instruments,* 77 (2006) 10E729.

[46] P. Tamain, M. Kočan, J. Gunn, et al., "Ion energy measurements in the scrape-off layer of MAST using a Retarding Field Analyzer", *Journal of Nuclear Materials,* 415 (2011) S1139-S1142.

[47] D.B. Crockett, P.E. Phillips. W.A. Craven, A.J. Wootton, A.S. Wan, T.F. Yang, "Edge parameters from an energy analyzer and particle transport on TEXT-U", *Review of Scientific Instruments,* 66 (1995) pp. 366-368.

[48] S. Raychaudhuri, S.K. Saha, S. Chowdhury, D. Banik, A.K. Hui, "Observation of high energy ion tail in the SINP tokamak plasma", *Physics of Plasmas,* 13 (2006) 122510-1-8.

[49] R.A. Pitts, S.J. Davies, I. Duran, et al., "Retarding field energy analyzer for the JET plasma boundary", *Review of Scientific Instruments,* vol. 74, no. 11 (2003).

[50] J.M. Stone, et. al., "Athena: A new code for astrophysical MHD," *The Astrophysical Journal Supplement Series,* Vol. 178, no. 1, p. 137, 2008.

[51] C. Dullemond and A. Johansen, "Hydrodynamics II: Numerical methods and applications." University Lecture, 2007.

[52] L.K.S. Daldorff, et. al., "Two-way coupling of a global Hall magnetohydrodynamics model with a local implicit particle-in-cell," *Journal of Computational Physics,* Vol. 269, pp. 236-254, 2014.

[53] St. Jankuhn, et. al., "Simulation of gridded broad-beam ion sources for ultra-precise surface processing," *Review of Scientific Instruments,* Vol. 77, 2006.

[54] N. Imtriaz, et. al., “Impact of plasma sheath on rocket-based E-region ion measurements,” *Astrophysics and Space Science*, Vol. 355, pp. 23-32, 2015.

[55] Anderson, E.; Bai, Z.; Bischof, C.; Blackford, S.; Demmel, J.; Dongarra, J.; Du Croz, J.; Greenbaum, A.; Hammarling, S.; McKenney, A.; Sorensen, D. (1999). LAPACK Users' Guide (Third ed.). Philadelphia, PA: Society for Industrial and Applied Mathematics. ISBN 0-89871-447-8.

[56] *COMSOL Multiphysics® Reference Manual*, COMSOL Version 4.3b (2013) http://hpc.mtech.edu/comsol/pdf/COMSOL_Multiphysics/COMSOL_ReferenceManual.pdf, Accessed: 2015-06-24.

[57] *Particle Tracing Module User’s Guide*, COMSOL Version 4.3b (2013) http://hpc.mtech.edu/comsol/pdf/Particle_Tracing_Module/ParticleTracingModuleUsersGuide.pdf, Accessed: 2015-06-23.

[58] J. Marshall, “Performance of a hydromagnetic plasma gun,” *Physics of Fluids*, vol. 3, no. 1, pp. 134-135, 1960.

[59] K. Schoenberg, R. Gerwin, I. Henins, R. Mayo, J. Scheuer, and G. Wurden, “Preliminary investigation of power flow and performance phenomena in a multimegawatt coaxial plasma thruster,” *Plasma Science, IEEE Transactions on*, vol. 21, pp. 625-644, Dec. 1993.

[60] G. W. Sutton and A. Sherman, Engineering Magnetohydrodynamics. New York: McGraw-Hill, 1965.

[61] J. P. Freidberg, Plasma Physics and Fusion Energy. Cambridge University Press, 2007.

[62] T.K. Gray (2009). (Doctoral dissertation). University of Illinois at Urbana-Champaign.

[63] S. Jung, D. Andruczyk, D.N. Ruzic, “Laboratory investigation of vapor shielding for lithium-coated molybdenum in DEVeX”, *Plasma Science, IEEE Transactions on*, vol. 40 (2012) pp. 730-731.

[64] F. W. Grover, Inductance Calculation: Working Formulas and Tables, p. 94. Dover, 1962.

[65] C. Grabowski, J. Degnan, T. Cavazos, D. Gale, C. Gilman, W. Sommars, T. Intrator, J. Taccetti, B. Waganaar, R. Siemon, andG. Wurden, "Development of a high-current low-inductance crowbar switch for FRX-L," *Plasma Science, IEEE Transactions on*, vol. 30, pp. 1905-1915, Oct. 2002.

[66] G. D. Cormack and A. J. Barnard, "Low inductance low pressure spark gap switch," *Review of Scientific Instruments*, vol. 33, no. 6, pp. 606-610, 1962.

[67] K. Matsugata, H. Tsuchida, H. Saitou, and K. Yatsui, "Studies and performance of decreased rail gap switch inductance by enhancing multichanneling via gas mixture," *Plasma Science, IEEE Transactions on*, vol. 25, pp. 97-99, Feb. 1997.

[68] J. Niedbalski, "High-voltage multichannel rail gap switch triggered by corona discharges," *Review of Scientific Instruments*, vol. 74, no. 7, pp. 3520-3523, 2003.

[69] K. J. Chung, K. S. Chung, and Y. S. Hwang, "Characteristics of rail gun plasma as a small-scale elm simulator," Presented at the 25th Symposium on Fusion Engineering, San Francisco, California, USA, 2013.

[70] I. R. R. Shinton, Ph. D. dissertation. Massey University, 2005.

[71] L. Brillouin, "A Theorem of Larmor and Its Importance for Electrons in Magnetic Fields," *Physical Review*, 67 (1945) pp. 260-266.

[72] A.W. Molvik, "Large acceptance angle retarding-potential analyzers," *Review of Scientific Instruments* 52, 704 (1981).

[73] P. Raman, I.A. Shchelkanov, J. McLain, and D.N. Ruzic, "High power pulsed magnetron sputtering: A method to increase deposition rate," *Journal of Vacuum Science and Technology A*, 33 (2015) 031304.

[74] H. Yu, et al., "Investigation and optimization of the magnetic field configuration in high-power impulse magnetron sputtering," *Plasma Sources Science and Technology*, 22 (2013) p. 045012.

[75] J. Alami, et al., “Plasma dynamics in a highly ionized pulsed magnetron discharge,” *Plasma Sources Science and Technology*, 14 (2005) 525.

[76] J. Alami, S. Bolz, and K. Sarakinos, “High power pulsed magnetron sputtering: Fundamentals and applications,” *Journal of Alloys and Compounds*, 583 (2009) pp. 530-534.

[77] B. Kouznetsov, et. al., “A novel pulsed magnetron sputter technique utilizing very high target power densities,” *Surface and Coatings Technology*, 122 (1999) pp. 290-293.

[78] J. Alami, et. al., “ On the deposition rate in a high power pulsed magnetron sputtering discharge,” *Applied Physics Letters*, 89 (2006) 154104.

[79] V.M. Bardakov, S.D. Ivanov, A.V. Kazantsev, and N.A. Strokin, “Peculiarities of measuring ion energy distribution in plasma with a retarding field analyzer,” *Review of Scientific Instruments*, 86 (2015) 053501.

[80] W.M. Stacey, Fusion Plasma Analysis. John Wiley & Sons, Inc., 1981.

APPENDIX

Appendix 1. Code Documentation

1.1 Simulation Codes

1.1.1 ATHENA MHD Code

The primary documentation for the entirety of the ATHENA MHD code used to simulate the compression and translation of the TELS plasma slug from the theta pinch region to the target region in Ch. 2 can be found on Princeton University's TRAC website. The download of the most current version of ATHENA, 4.2, is also available through this website and the code is licensed as an open source code through GNU licensing with strict adherence to ANSI standards.

The primary file used for simulating TELS, entitled 'cyl_newgradient3_02_2.c', sets up the majority of initial plasma and field parameters, which are used as inputs into the primary ATHENA code. For instance, the code initializes the physical geometry of the TELS device, along with the initial density and velocity of the plasma slug as it enters the θ pinch region from the coaxial plasma accelerator. More important to the simulation, the code sets up the magnetic field geometries and the resultant time-dependent fields, while also giving a determination as to the penetration strength and depth of each field into the plasma. The ghost cells at the boundaries are defined within this script and given the appropriate values and conditions to be able to set up the proper boundaries in the radial, axial, and azimuthal directions. More information regarding the initialization and usage of this script as a tool for generating DEVeX plasma conditions can be found in Ref. [2]. In most cases, ATHENA has pre-set boundary conditions that can be called and used when running the script. Sometimes, however, these conditions are not appropriate for all variables. The script uses a user-defined void function to define the outer radial boundary as a condition where the plasma momentum is reflected at the wall, but the magnetic field is left to evolve or dissipate. It is also important to note that in this script, the cylindrical geometry is defined for the domain and allocates the memory for storing the output. It is important to note that ATHENA uses cgs units to define parameters.

The script is used by the main ATHENA MHD code and called through the input file ‘athinput.test8’. It is in this input script that the majority of the ATHENA commands are used in conjunction with the geometry and domain setup defined in ‘cyl_newgradient3_02_2.c’. This script initially calls the C file as the job to run in the primary ATHENA code and defines the output format for the dump files, which are set as .vtk files and can be visualized using Paraview. The time domain information is then established, with the initial time step set to 10 ns and the total time domain length set to 10 μs. ATHENA dynamically modifies the time step as it iterates, especially once the simulation reaches a critical point where fine details of momentum flow and field penetration, as well as their interaction, become critical to model across the mesh sizes at much smaller time intervals. The code is three dimensional, but the simulation is assumed to be axisymmetric. Each spatial domain is established and the number of nodes in each direction is generated. It is also in this input file that the appropriate boundary flags are called, whether they be default ATHENA boundaries or not. For fluid dynamics and energy purposes, the specific heat ratio of hydrogen as the gas is also defined in this input file. These files can easily be called and ran using the ‘dosim.sh’ bash file or the ‘dosim.pbs’ cluster command file, while also using the open mpi module for parallelization, once ATHENA has been downloaded and the ‘cyl_newgradient3_02_2.c’ file has been copied to the source folder, which stores all the C scripts that can be called for simulation.

In an effort of clarity, the steps needed to run the ATHENA simulation that was used for this report are outlined below:

1. Download the ATHENA MHD code from the Princeton TRAC website. Follow the downloading tutorial found on the website in order to troubleshoot any issues. Download the code into a separate ATHENA directory.
2. Inside the main ATHENA directory, make a sub-directory to which the ‘athinput.test8’, ‘dosim.sh’, and ‘dosim.pbs’ can be saved. This folder will also serve as the sub-directory to which all of the outputs will be saved.
3. Inside the main ATHENA directory, there will be a ‘source’ sub-directory in which all the C scripts used as inputs into the ATHENA main code are stored. The file ‘cyl_newgradient3_02_2.c’ will be stored here.
4. The code can now be run on the local platform by initiating the ‘dosim.sh’ file.

1.1.2 Kinetic Particle-Mesh Code

Much of the kinetic particle mesh code is outlined in Ch. 2, specifically the physics employed and the numerical methods that govern the simulation progression. Individual Python scripts, however, were not spoken of in detail. This section aims to elaborate on those individual scripts on how they are ran to generate results such as those found in Ch. 2.

The first script, which is called by the other two major scripts, is 'matmaker2.py'. A number of functions are introduced in this script that generate the A matrix and the blank solution vector, denoted by the variable b. Most important of these is the function that generates the diagonal and off-diagonal components that form the basis for the numerical calculation for the Laplacian of the potential, and, subsequently, the electric field at each node. The size of the A matrix is based on the number of nodes in the simulation, which is used as an input into the function that builds the A matrix.

The next higher script, 'MSPTrack2.py', is a script used as a collection of functions that is again called by the main script. This script is different from 'matmaker2.py' in that it specifically sets up the physics as it applies to each node and the dynamics as it applies to individual particles. It is also within this script that the particle-to-computation value is defined. In the function 'EPmaker', weights through the Cloud-in-Cell method are applied from the contribution of each individual charged particle to the surrounding nodes and then these contributions are added to the appropriate position in the b vector. The appropriate modifications for the b vector with regards to boundary conditions are made after the source vector has been generated through the aforementioned weighting scheme. The potential vector is then solved for and the electric field at each node is evaluated. These values are then weighted back to the particles with a similar weighting scheme as used before, in the x-y plane. The function 'dynamics' takes the positions and velocities of the particles, along with the updated electric field values and updates the positions and velocities of each particle in each direction using force balance. This function also has a built in way of using an applied external field as part of the momentum balance, but these values need to be manually changed to generate the desired field strength for a given set of conditions to be modeled.

The parent script that utilizes the functions built in the previous two scripts, entitled 'MStest*.py', is the code that is run when executing a job in the Python IDE. It is recommended that any future use of these codes be done using the Anaconda Python IDE, since the open source download comes pre-loaded with a number of the modules needed by these scripts. There are multiple versions of this parent script, all of which are modified with respect to the spatial dimension, the time step, and the geometry of the collimator. The first few lines of the script make a sub-directory within the default 'Python Scripts' parent directory, generated after downloading the Anaconda IDE. Within the sub-directory generated at the beginning of the script, outputs in terms of the potential and particle positions are saved as .png files. Next, the number of nodes, the two-dimensional spatial domain, and the time step are all defined, along with a number of other constants and arrays used for output storage. The number of particles are then initialized and given random positions within the starting domain illustrated in Ch. 2. Electron velocities are randomly selected from the electron velocity distribution function ATHENA output and ion velocities are randomly selected from the ion velocity distribution function ATHENA output. Bin vectors then are generated for both species in order to effectively bin the velocities of each particle type upon crossing the right most boundary. The initial electric field felt by each particle is generated using the function 'EPmaker' from 'MSPTrack2.py', and the particles are then left to evolve over time using the main portion of the code, which calls the 'dynamics' function at each time step to update the particle positions and velocities and then updates the electric fields. Within this primary loop over time, boundaries are enforced through sets of conditional statements and particles with positions at or outside the boundaries are recycled to the initial domain and given new random initial velocities. The most unique portion of this code deals with the collimator boundary, which can be modified in both the x- and y-directions through the use of another series of conditional statements. Similar to the boundaries, if the particle positions lie at or within the geometry defined by the collimator, these particles are then recycled to the initial domain. During this evolution, outputs are saved to the sub-directory at every 100 or 1000 time steps, again based on a conditional statement. Once the simulation has concluded, the number of each particle type crossing the right boundary as a function of time are plotted, which is essentially an indication of the flux. This plot is also saved to the same sub-directory as the rest of the output.

It is recommended that future work with these scripts modify the boundary conditions, as well as the spatial and time scales in order to make sure that the simulation is providing accurate results that are not subject to numerical instability. As mentioned in Ch. 2, it seems that the errors associated with the particle mesh simulation arise out of numerical instability, or are subject to issues dealing with low particle fluxes on the downstream side of the collimator as compared with the upstream side. Other future endeavors should include the modifications of both the particle mover and the field generator subroutines of the kinetic particle-mesh simulation.

1.1.3 COMSOL Multiphysics Simulation

The COMSOL model, entitled 'RFEA COMSOL Model.mph', is the primary model used for the electrostatic field generation and ion tracing through the remaining portion of the analyzer. The simulation is in two dimensions, and the physics employed are simply the electrostatic and particle tracing modules. The geometry is built to a fraction of the full analyzer cross-section, but is still adequate enough to sample the electrostatic effects felt by particles at each of the three grids past the initial collimating grid. What sets this model apart from other electrostatic/particle tracing models is that the velocity distribution for each particle is randomized for the particle inlet based on the distributions found through the velocity binning process in the previous kinetic particle-mesh simulation. The grids are generated based on the dimensions of the each physical mesh described in Ch. 3 and the collector is set to the same depth as the physical collector plate. Only 3 materials are used to define the boundaries in this simulation: air (vacuum), 304 stainless steel for the grids, and copper for the collector.

For the electrostatic module, '*es*', each grid is set to a given initial potential, while the collector is set to a 0 potential. This solution is stationary, meaning that transience is not a factor here. Dirichlet conditions are set for the top and bottom of the full simulation domain and periodic conditions are set for the left and right boundary. The periodic conditions are used since the actual full dimension of the analyzer is much larger than that depicted by the model geometry. This module is called using the external Matlab code, described in Ch. 2, and the entire simulation is iterated with respect to the potential applied to G2.

The time-dependent charged particle tracing module, '*cpt*', is the portion of the model that defines the particle type and the boundaries applied at each interface. The inlet is a single line above the electron repeller grid, at which 500 hydrogen ions are initialized with a random velocity, called from the globally defined random variable, and with a position corresponding to a uniform distribution across this line inlet. All interfaces or boundaries are set as 'stick' conditions, except for the left and right boundaries, which are set to 'bounce' conditions used to imply periodicity. The electric force interactions of the particles with the surrounding medium are found using the previously described stationary '*es*' module, and particle-particle interactions are employed, assuming Coulombic interactions. The effects of elastic collision can be toggled on and off in this module, to illustrate the effect that neutrals might play on the charged particle trajectories. An outlet condition is held at the top boundary of the collector, from which particle statistics can be exported. The time-dependent study is set to a time step of 10 ns, to fully capture particle movement and the simulation runs to 20 μs. The Matlab commands corresponding to this model generate .csv outputs of the particle statistics at the surface of the collector for each new value of the ion discriminating potential.

1.2 Analysis Codes

1.2.1 Matlab IEDF

The primary language used to analyze the experimental currents collected at each ion discriminating potential is Matlab. The parent script, entitled 'TemporalIEDF.m' calls numerous functions in order to generate three main plots that illustrate various forms related to the distribution function with respect to time. The main file reading function used to collect data in a concise sequential order is entitled 'uipickfiles.m' and is available online through the Matlab Stack Exchange website. The data sets are saved into cell arrays and must be extracted from these arrays using a small series of commands, different from the ordinary method of using Matlab's default 'uigetfiles.m'. The second thing this parent script does is ask the user for input regarding two variables. These are the discriminating potential corresponding to each collection of files and a guess at the empirical shifted value for the shifted energy distribution.

The parent script then calls the function 'RFEAfileread.m', which first interpolates the current waveforms to the smallest of the time divisions used when reading data from the oscilloscope using the function 'RFEAInterp.m'. If time step were not the same for each of these data sets, then there would be large errors between current values, and the resultant distributions would not be properly resolved. This function then uses a graphic interface for the plot of the net current, closed analyzer value subtracted from the open analyzer value, to extract the point in which the PiP discharges. This is evident in the net current plot once the net current begins to dip to negative values beyond that of the noise. The time vectors and current vectors are modified with respect to this bound and set as outputs to the function.

The parent script then calls the function 'RFEAStats.m'. This function uses the outputs from 'RFEAfileread.m' and generates averaged net current values for each unique ion discriminating potential value. For instance, if multiple data sets are collected for an ion discriminating potential of 0 V, this script averages the currents and gives the standard deviation at each time step. If only one data set is collected for a given discriminating potential, the standard deviation at each time step is set to a constant of 1 μA, which is reasonable since the maximum of the population standard deviation for any unique value of discriminating potential is 14.5 μA.

From the output of 'RFEAStats.m', the parent script then calls the function 'RFEAlimit.m'. The purpose of this script is only to limit the window of calculation to only the portion of the collected net current data that corresponds to the time frame in which the bulk plasma is interacting with the analyzer. For the case with the PiP and the theta pinch, this occurs nearly 60 μs after the PiP discharges, while the case with just the PiP has this starting point closer to 70 to 75 μs after the PiP discharges. The user again uses a graphical interface to select a set of bounds. Within these bounds, the last point below a net current value of 0.0 is taken as the starting point for each time and current vector.

The outputs from this data-limiting function are then used as inputs into 'RFEAIsmooth.m'. As was the case with 'RFEAlimit.m', this function has a singular purpose to smooth the current data at each individual time step with respect to the discriminating voltage. This is accomplished by applying a 7-point moving average smoothing routine. This function

outputs the final set of net currents that will be used to generate the distribution functions in the parent 'TemporalIEDF.m' script.

Before the derivatives can be taken and normalized to give the distributions, from which the ion temperatures are evaluated using a fit routine, the currents are normalized to the peak current values at each time step, represented by the data collected at the discriminating potential of 0 V. These normalized currents are then taken and the derivative with respect to the discriminating voltage is found using a second order central difference scheme for every value of the discriminating voltage, except for the first and last values. The first value at each time step is set to a constant of 0 and the last value is found using a backward difference scheme. These derivatives are then normalized so that the area under the curve at each time is set to unity. These normalized curves are also smoothed with respect to the discriminating potential using a 3-point moving average, so that the resulting outputs can be compared. The normalized curves are output as figures (2) and (3), while figure (1) outputs the non-normalized derivative of the current with respect to the discriminating potential, divided by the maximum value of this derivative. The smoothed, normalized distribution function is what is then used in the fitting routine to extract the ion temperature at each point in time. At this point, it is important to save the workspace to be used in the following ion temperature fitting routine.

1.2.2. Matlab T_i Fitting

Each of the smoothed, normalized IEDF curves was then fit to a drifted energy distribution, defined by Eq. (4.1). Through this function fit of the data, the ion temperature and the drifted energy value were found, and 95% confidence intervals for both parameters were set as outputs. As mentioned in Ch. 4, the normalization of the curves to unity gave rise to undesirable features in the trends, which made the fitting difficult at certain points in time. Ion temperature values well above those considered reasonable for the TELS plasma type were discarded, or set to 0, in this fit where the undesirable features in the smoothed distribution prevailed. This was often the case past a time of 260 to 270 μs after the PiP discharge and in between the primary current features, typically around 90 to 110 μs.

To properly apply a Matlab fitting routine to a set of data, the ‘fittype’ must first be generated as a separate structure. This ‘fittype’ can either be a built-in Matlab construct or a user-defined curve. For the fitting of the normalized IEDF plots over time, the user-defined function ‘IEDFfit.m’ was used. The ‘fittype’ only has to be generated once and does not have to be cleared from memory before iterating through the fitting routine.

Two fitting scripts were employed, one for the case with the theta pinch and the PiP and one for the case with the PiP only. These are labeled ‘FittingTi.m’ and ‘FittingTiPiP.m’, respectively. The built-in Matlab ‘fit’ function saves the output in a separate structure in the Matlab workspace, and the temperature can be extracted for individual fits using the command ‘f.T’. The scripts save the ion temperatures (not related to the undesirable features) and the bounds associated with the 95% confidence interval of each parameter fit. This ion temperature vector can then be plotted as a function of time.